Macroscopic Modeling of Open-Cell Foams:

An Order Parameter Approach

Dissertation

zur Erlangung des Grades

Doktor der Ingenieurwissenschaften (Dr.-Ing.)

der Naturwissenschaftlich-Technischen Fakultät III

Chemie, Pharmazie, Bio- und Werkstoffwissenschaften

der Universität des Saarlandes

vorgelegt von

Dipl.-Ing. Alexander Geringer

Saarbrücken

2014

Tag des Kolloquiums: 11.02.2015

Dekan:	Prof. Dr.-Ing. Dirk Bähre
Berichterstatter:	Prof. Dr.-Ing. Stefan Diebels
	Prof. Dr.-Ing. Ralf Müller
Vorsitz:	Prof. Dr. Christian Motz
Akad. Mitarbeiter:	Dr.-Ing. Daniela Petri

Preface

The research described herein was carried out during my time as a PhD student at the Chair of Applied Mechanics at Saarland University from 2009 to 2014.

First and foremost, I would like to express my sincere appreciation to my adviser Professor Dr.-Ing. Stefan Diebels. I am very grateful for having the opportunity to work in the field of numerical modeling and all the fruitful discussions and extraordinary encouragement throughout the years.

I would also like to thank Professor Dr.-Ing. Ralf Müller for being the co-referee of this thesis and his keen interest in my research.

Furthermore, I would like to thank the former and the present colleagues from the Chair of Applied Mechanics for the pleasant working atmosphere. I would also like to give special thanks to Dr.-Ing. Joachim Schmitt for many inspiring conversations and support.

My endless gratitude goes to my family and, especially, my wife, Lena, for their continuous encouragement and trust.

Abstract

Metallic foams are an advanced material which becomes more and more attractive due to the unique combination of the mechanical properties they provide, such as high stiffness, low weight, good damping, and energy absorption properties. The microstructure defines significantly the mechanical response of the foam material on the macroscopic level.

In the present work, the order parameter approach is used to model the macroscopic behavior of open-cell foams. For this purpose an additional field linked to the foam microstructure and governed by the general equilibrium relationship is introduced.

The application of the order parameter model is examined as an alternative to micropolar continuum model regarding the size effect modeling. Furthermore, a topologically motivated order parameter damage evolution model is presented.

The comparison with the results of a field experiment proves the flexibility of the proposed damage formulation. The capability of the model regarding the prediction of the size effect is demonstrated using the standard benchmarks.

Zusammenfassung

Metallschäume sind ein Beispiel für ein modernes Material, dessen Bedeutung als Werkstoff stetig zunimmt. Dies ist auf die einzigartige Kombination mechanischer und physikalischer Eigenschaften, wie z. B. hohe Steifigkeit, leichtes Gewicht, hohe Dämpfungseigenschaft und Energieabsorption, zurückzuführen. Die makroskopischen mechanischen Materialeigenschaften der Schaumstoffe sind maßgeblich durch ihre Mikrostruktur bestimmt.

In der vorliegenden Arbeit wird das makroskopische Materialverhalten der offenporigen Schäume mithilfe eines Ordnungsparameter-Modells beschrieben. Hierfür wird auf der Basis der allgemeinen Bilanzgleichung ein zusätzliches und mit der Mikrostruktur verknüpftes Feld eingeführt.

Die Anwendung des Ordnungsparameter-Modells wird als Alternative zum mikropolaren Kontinuum unter dem Aspekt der Beschreibung von Maßstabseffekten untersucht. Als eine weitere Anwendung des Ordnungsparameter-Modells wird die Formulierung eines topologiebasierten Schädigungsmodells vorgestellt.

Die Flexibilität des Ordnungsparameter-Schädigungsmodells wird anhand der Gegenüberstellung der experimentellen Ergebnisse und der Ergebnisse der numerischen Simulation gezeigt. Die Verwendung des Ordnungsparameter-Modells für die Beschreibung der Maßstabseffekte wird anhand von Standardtests anschaulich demonstriert.

Contents

List of Figures

1

Introduction

Foams are complex and challenging materials with a distinct microstructure. The most prominent example of a foam material is perhaps the cancellous bone (figure 1.1, left) provided by nature as a result of millions of years of evolutionary design. Metallic foams (figure 1.1, right), in particular, are an advanced material which is becoming more and more attractive due to the unique combination of the mechanical properties such as high stiffness, low weight, good damping and energy absorption properties they offer. Today, foam materials are used in the majority of industries such as automotive, acoustics, filtration industry, electronics, and medicine. The diversity of materials used to produce foams is also very large: metal alloys and ceramics, resin, polymers, and glass can be processed to foam structures.

The increasing acknowledgment of foams as an engineering material requires appropriate and validated theoretical and numerical models, which describe each aspect of the complex material behavior of this highly interesting material.

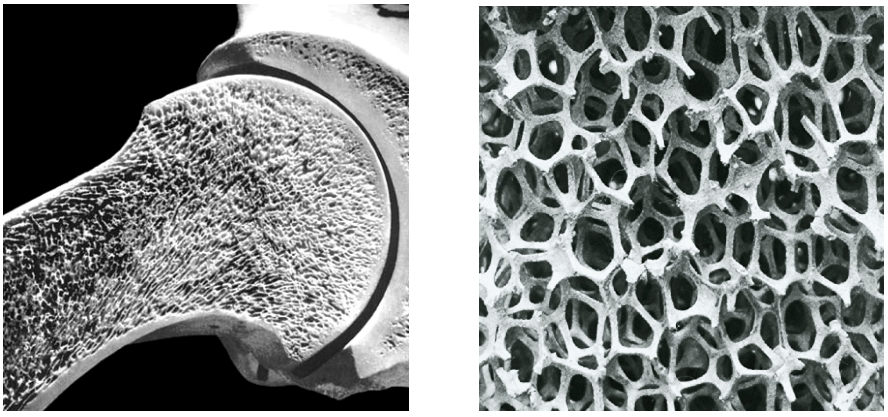

Figure 1.1: Examples of cellular materials: cancellous bone tissue [39] (left) and metal open-cell foam (right).

However, the mechanical behavior of foams is still an unsolved problem regarding theoretical modeling. The classical continuum approach cannot describe the size effects usually observed in cellular materials such as the effective mechanical properties (e. g. stiffness, stress concentration factor) which depend on the ratio between pore size and specimen size.

The mechanical properties of foam materials are mainly defined by the structure of the material on the microscopic level (cf. [33, 120]). The inclusion of the effects caused by the microstructure allows for the prediction of the specific behavior of the cellular materials in the macroscopic model.

Apart from the homogenization techniques described in [2, 57, 60], the material microstructure can be taken into account by an additional quantity characterizing the microstructure. This quantity can be a scalar, vector or some higher-order tensor complementing a classical macroscopic continuum model.

One of the established extended continuum theories was proposed by Cosserat brothers (cf. [25]). Here, the material point is considered as a rigid body with three translational and additional three rotational degrees of freedom. The framework they provided was further developed by Eringen and renamed to *micropolar* theory (cf. [43, 41, 67]). The *micromorphic* theory with the ma-

terial point being a continuum with an infinite number of degrees of freedom (cf. [42, 43]) includes the micropolar theory as the special case. The *second gradient* theory provides another generalization of the classical Cauchy continuum. Here, the constitutive equations are formulated involving the strain gradient (cf. [31, 36, 92, 94]).

The multifield theories introduce a supplementary field to describe the influence of the substructure. This class of models covers the mechanical behavior of materials with substructure in the sense of multiscale approaches (cf. [1, 46, 89]). The *order parameter* approach is a general framework for the formulation of continua with any number of additional degrees of freedom (cf. [18, 19]). An order parameter is a characteristic value representing the material substructure which is associated with a material point. The choice of the order parameter depends on the physical nature of the phenomenon to be predicted by the additional field (cf. [122]).

The scalar valued order parameter is used in *phase-field* formulations to characterize the evolution of the interface position by the continuous variable, which takes two different values depending on the phase domain. In the area of the interface, the value of the variable changes gradually and forms a diffuse interface. The phase-field method allows for the description of the microstructure evolution in a wide range of applications such as solidification (cf. [5, 14, 107, 112]), fracture (cf. [73, 91, 88]), and damage mechanics (cf. [13, 126]). The contributions by [22, 96, 104, 114] provide a comprehensive overview of the developments and applications of the phase-field method.

Apart from the mechanical properties, the modeling of damage evolution is another challenge related to foam materials. The consequence of the damage process is an alteration of several material properties on multiple scales in combination with changes in microstructure. The modeling of the damage effects is carried out using an auxiliary continuous variable representing the damage state (cf. [65, 72, 85]).

The goal of the present contribution is the exploration of applications of

the order parameter approach with a scalar valued field variable. Following aspects related to the description of open-cell foam materials are investigated using the order parameter approach:

prediction of the size effect

damage evolution

The thesis is organized as follows. The motivation and goals of the work are presented in the first chapter.

The second chapter gives an overview of continuum theories utilized in the present work. First the basic concepts of the standard Cauchy continuum theory are presented. This theory is a basis continuum model, whereas the micropolar theory and order parameter approach presented in the subsequent sections are considered as the extensions of the standard theory.

The third chapter deals with the description of the size effect. This is accomplished using three distinct approaches: high-resolution micromechanical model, micropolar theory and order parameter approach. The order parameter model is applied as an alternative providing additional advantages compared to the micropolar theory. The problem of the identification of model parameters is also treated in this chapter.

The fourth chapter considers the application of the order parameter approach in the framework of damage mechanics. Therefore, a short survey of the continuum damage mechanics is given. Next, a model of the damage evolution in an open-cell foam material is proposed. The influence of the model parameters is studied in order to provide a detailed insight into the model behavior. Last but not least the experimental validation is another topic discussed in this chapter.

Finally, the fifth chapter sums up the achieved results and draws the conclusions from this work.

2

Continuum Theories

Continuum mechanics is a phenomenological theory. It describes the phenomena and results observed in experiments based on idealized mathematical models on macroscopic level. Continuum mechanics can be organized in three main categories:

kinematics, considering the motion, geometry and deformation state regardless the cause

balance laws, which apply to all bodies disregarding their constitution

constitutive equations describing the relation between deformation state and stress

In the following the isothermal case is considered. Hence, only the balance equations of linear and rotational momentum are discussed. The order parameter approach discussed in this work is an extension to the classical continuum theory, i. e. so-called *Cauchy* continuum. Therefore, an overview of the continuum theories is presented in this chapter.

2.1 *Cauchy* Continuum Theory

2.1.1 Kinematics

In the context of the Cauchy continuum theory (cf. [10, 56, 58, 61]) a material body $\mathcal{B}$ defined as a set of elements X, called material points, is considered. The material body is bounded by the surface $\partial\mathcal{B}$. The material point X can be set into a one-to-one relation with a point in a physical space. This way the physical properties of the material point can be expressed by a mathematical point.

The configuration of the material body $\mathcal{B}$ is a mapping

$$\mathbf{x} = \boldsymbol{\chi}(\mathbf{X}, t)\,. \tag{2.1}$$

The vector function $\boldsymbol{\chi}$ denotes the position $\mathbf{x}$ of all of the material points of the body $\mathcal{B}$ (figure 2.1) in the actual configuration at time $t > t_0$ with respect to some fixed position $\mathbf{X}$ called reference configuration at a time $t = t_0$. This mapping is assumed to be continuous and uniquely invertible, so that the inverse is given by

$$\mathbf{X} = \boldsymbol{\chi}^{-1}(\mathbf{x}, t)\,. \tag{2.2}$$

The partial differentiation of equation (2.1) with respect to position vector $\mathbf{X}$ of the reference configuration provides the deformation gradient

$$\mathbf{F} = \frac{\partial \boldsymbol{\chi}(\mathbf{X}, t)}{\partial \mathbf{X}} = \operatorname{Grad} \boldsymbol{\chi}\,. \tag{2.3}$$

The inverse deformation gradient is

$$\mathbf{F}^{-1} = \frac{\partial \boldsymbol{\chi}^{-1}(\mathbf{x}, t)}{\partial \mathbf{x}}\,. \tag{2.4}$$

The displacement field $\mathbf{u}$ associated with the deformation map $\boldsymbol{\chi}$ is defined as

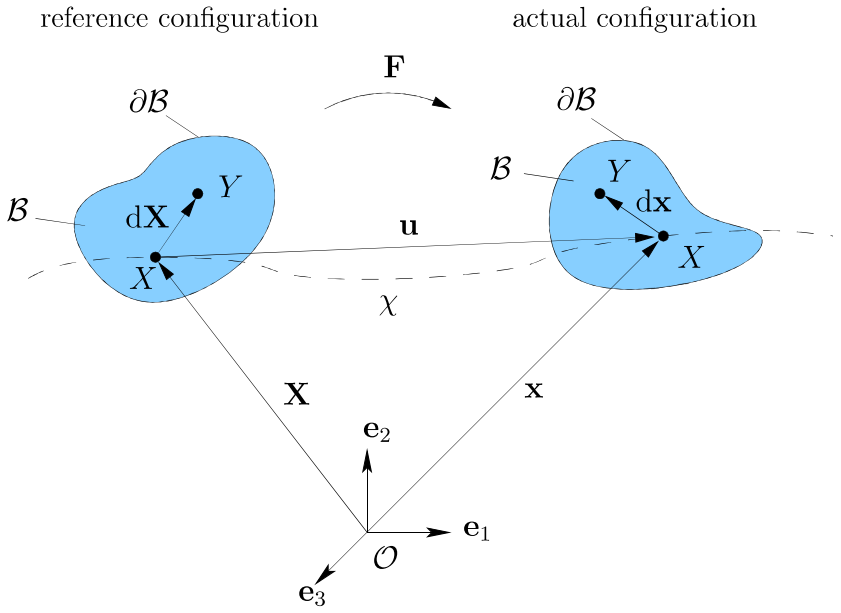

Figure 2.1: Kinematics of Cauchy continuum theory.

the difference of the position vectors of the actual and reference configuration

$$\mathbf{u} = \mathbf{x} - \mathbf{X}\,. \tag{2.5}$$

The deformation gradient can be formulated using the gradient of the displacement field from equation (2.5)

$$\mathbf{F} = \mathbf{I} + \mathrm{Grad}\,\mathbf{u}\,, \tag{2.6}$$

where $\mathbf{I}$ is the identity tensor.

With the deformation gradient $\mathbf{F}$ the relation between a line element $\mathrm{d}\mathbf{X}$ of the reference and a line element $\mathrm{d}\mathbf{x}$ of the actual configuration can be established

$$\mathrm{d}\mathbf{x} = \mathbf{F} \cdot \mathrm{d}\mathbf{X}\,. \tag{2.7}$$

As the measure of deformation between the actual and reference configuration, the squared differential line element in the respective configuration is used

$$\mathrm{d}s^2 = \mathrm{d}\mathbf{x} \cdot \mathrm{d}\mathbf{x}\,, \quad \mathrm{d}S^2 = \mathrm{d}\mathbf{X} \cdot \mathrm{d}\mathbf{X}\,. \tag{2.8}$$

Using the equation (2.7) the product $\mathrm{d}\mathbf{x} \cdot \mathrm{d}\mathbf{x}$ can be expressed in terms of the line elements of the reference configuration

$$\mathrm{d}\mathbf{x} \cdot \mathrm{d}\mathbf{x} = \mathrm{d}\mathbf{X} \cdot \mathbf{C} \cdot \mathrm{d}\mathbf{X}\,, \tag{2.9}$$

where $\mathbf{C}$ is the right Cauchy-Green deformation tensor, expressed in terms of the deformation gradient as

$$\mathbf{C} = \mathbf{F}^T \cdot \mathbf{F}\,. \tag{2.10}$$

The initial product $\mathrm{d}\mathbf{X} \cdot \mathrm{d}\mathbf{X}$ is obtained using the line elements of the actual configuration

$$\mathrm{d}\mathbf{X} \cdot \mathrm{d}\mathbf{X} = \mathrm{d}\mathbf{x} \cdot \mathbf{B}^{-1} \cdot \mathrm{d}\mathbf{x} \tag{2.11}$$

with $\mathbf{B}$ as the left Cauchy-Green tensor, expressed using the deformation gradient

$$\mathbf{B} = \mathbf{F} \cdot \mathbf{F}^T\,. \tag{2.12}$$

The change in scalar product can be expressed using the differential line elements of the reference configuration

$$\mathrm{d}\mathbf{x} \cdot \mathrm{d}\mathbf{x} \; - \mathrm{d}\mathbf{X} \cdot \mathrm{d}\mathbf{X} = \mathrm{d}\mathbf{X} \cdot 2\,\mathbf{E} \cdot \mathrm{d}\mathbf{X}\,, \tag{2.13}$$

where $\mathbf{E}$ is the Lagrangian or Green strain tensor defined as

$$\mathbf{E} = \frac{1}{2}(\mathbf{C} - \mathbf{I})\,. \tag{2.14}$$

The equivalent change in scalar product can also be obtained by means of line elements from the actual configuration

$$\mathrm{d}\mathbf{x} \cdot \mathrm{d}\mathbf{x} \; - \mathrm{d}\mathbf{X} \cdot \mathrm{d}\mathbf{X} = \mathrm{d}\mathbf{x} \cdot 2\,\mathbf{A} \cdot \mathrm{d}\mathbf{x}\,, \tag{2.15}$$

with $\mathbf{A}$ as the Almansi strain tensor

$$\mathbf{A} = \frac{1}{2}(\mathbf{I} - \mathbf{B}^{-1})\,. \tag{2.16}$$

In the framework of the geometric linear theory, where the reference and actual configurations coincide, the linearized Green strain tensor can be reduced to

$$\mathrm{lin}(\mathbf{E}) := \boldsymbol{\varepsilon} = \frac{1}{2}(\mathrm{Grad}\,\mathbf{u} + \mathrm{Grad}^{\,T}\mathbf{u})\,, \tag{2.17}$$

which is a symmetric part of the displacement gradient $\mathrm{Grad}\,\mathbf{u}$.

2.1.2 Translational Momentum

The conservation law for translational momentum states that the change in total linear momentum of a body is affected by external forces. In the static case, with the inertia forces ignored, this means that the sum of forces acting on the body vanishes

$$\int_B \rho\,\mathbf{b}\,\mathrm{d}v + \int_{\partial B} \mathbf{t}\,\mathrm{d}a = 0\,. \tag{2.18}$$

With the Cauchy theorem, stating the existence of the second-order tensor $\mathbf{T}$, relating the normal vector $\mathbf{n}$ to the traction vector $\mathbf{t}$,

$$\mathbf{t} = \mathbf{T} \cdot \mathbf{n}\,, \tag{2.19}$$

the equation (2.18) can be written in terms of the Cauchy stress $\mathbf{T}$

$$\int_B \rho\,\mathbf{b}\,\mathrm{d}v + \int_{\partial B} \mathbf{T}\cdot\mathbf{n}\,\mathrm{d}a = 0\,. \tag{2.20}$$

Transforming the second term of the equation above using the divergence theorem the local form of the equation (2.20) expressed in terms of a differential equation is obtained

$$\operatorname{div}\mathbf{T} + \rho\,\mathbf{b} = \mathbf{0}\,. \tag{2.21}$$

2.1.3 Rotational Momentum

The conservation law of rotational momentum declares that the external torque acting on a body changes its rotational momentum. Neglecting the rotational inertia in the quasi-static case it implies that the total moment of the body and traction forces with respect to any point must vanish

$$\int_B \mathbf{x}\times\rho\,\mathbf{b}\,\mathrm{d}v + \int_{\partial B} \mathbf{x}\times\mathbf{t}\,\mathrm{d}a = \mathbf{0}\,. \tag{2.22}$$

Substituting the result from equation (2.19) into the law of rotational momentum and since the cross product of a second rank tensor and a vector delivers another second rank tensor, the rotational momentum equation becomes

$$\int_B \mathbf{x}\times\rho\,\mathbf{b}\,\mathrm{d}v + \int_{\partial B} (\mathbf{x}\times\mathbf{T})\cdot\mathbf{n}\,\mathrm{d}a = \mathbf{0}\,. \tag{2.23}$$

Applying the divergence theorem gives

$$\int_B \mathbf{x}\times\rho\,\mathbf{b}\,\mathrm{d}v + \int_B \operatorname{div}(\mathbf{x}\times\mathbf{T})\,\mathrm{d}v = \mathbf{0}\,. \tag{2.24}$$

Using the property of the divergence of cross product (cf. [26]) the rotational momentum becomes

$$\int_B (\mathbf{x} \times \rho\,\mathbf{b} + \mathbf{x} \times \operatorname{div} \mathbf{T} + \mathbf{I} \times \mathbf{T})\,\mathrm{d}v = \mathbf{0}\,. \tag{2.25}$$

Taking into account the translational momentum and remembering that the balance of rotational momentum is valid for any region of the body the resulting equation becomes

$$\mathbf{I} \times \mathbf{T} = \mathbf{0}\,, \tag{2.26}$$

which indicates the symmetry of the Cauchy stress tensor $\mathbf{T} = \mathbf{T}^T$.

2.1.4 Constitutive Relation

In the case of linear elastic material behavior the relationship between stress and strain components is considered to be a linear function. This relationship is expressed by the generalized Hooke's law

$$\mathbf{T} = \overset{4}{\mathbf{C}} : \boldsymbol{\varepsilon}\,, \tag{2.27}$$

where $\overset{4}{\mathbf{C}}$ is a material tensor of fourth rank containing elastic coefficients.

For material with isotropic behavior this equation can be rewritten as

$$\mathbf{T} = 2\mu\,\boldsymbol{\varepsilon} + \lambda(\operatorname{tr}\boldsymbol{\varepsilon})\,\mathbf{I}\,, \tag{2.28}$$

with the two independent material parameters μ and λ, also known as Lamé constants. These constants completely define the material behavior in linear elastic isotropic case. Each elastic constant can also be expressed in terms of two other constant pairs (i. e. such as Young's modulus and Poisson's ratio or shear and bulk modulus). The relationships of the Cauchy continuum theory are displayed in figure (2.2).

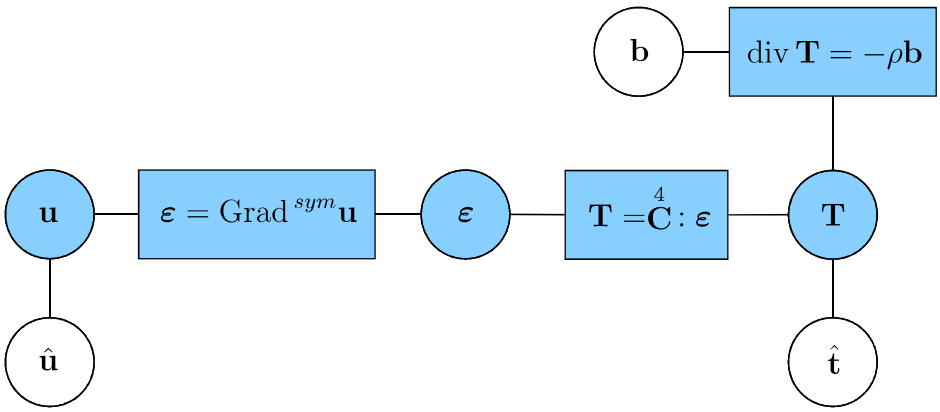

Figure 2.2: Tonti diagram of Cauchy continuum theory.

In general, a constitutive relation links the kinetic quantities such as stresses to the kinematic quantities such as strains. The constitutive relations have to fulfill certain conditions imposed by physical laws. A detailed discussion on constitutive modeling can be found in [56, 58, 61].

2.2 Micropolar Continuum Theory

2.2.1 Kinematics

The description of the kinematics in the framework of the micropolar continuum can be seen as the generalization of the Cauchy continuum theory. The micropolar continuum represents a kinematically extended continuum where every material point has three rotational degrees of freedom in addition to three translational degrees of freedom. The additional independent variable $\bar{\varphi}$ is, therefore, defined. This variable describes the rigid body rotation of the material point.

In addition to the line elements of the Cauchy continuum theory three vectors, the so-called directors describing the orientation, are associated with the material point. Each director has a constant length and remains always perpendicular to the other directors.

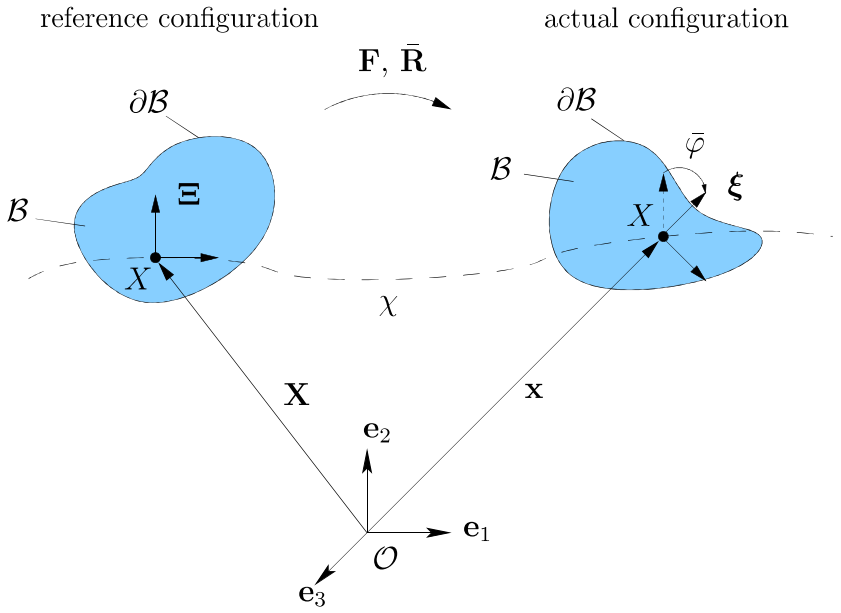

Figure 2.3: Kinematics of the micropolar continuum theory.

The directors denoted by $\boldsymbol{\Xi}_i$ describe the orientation of the material point in the reference configuration, and the directors denoted by $\boldsymbol{\xi}_i$ refer to the actual orientation (figure 2.3). The relation between the directors of the actual and reference configuration is described with the proper orthogonal tensor $\bar{\mathbf{R}}$, the so-called micromotion tensor (cf. [43])

$$\boldsymbol{\xi} = \bar{\mathbf{R}}(\mathbf{X}, t) \cdot \boldsymbol{\Xi} \,. \tag{2.29}$$

An orthogonal tensor maps a vector onto another vector with the identical length and has the properties $\bar{\mathbf{R}} \cdot \bar{\mathbf{R}}^T = \mathbf{I}$ (orthogonal) and $\det \bar{\mathbf{R}} = +1$ (proper orthogonal).

The micromotion tensor $\bar{\mathbf{R}}$ can be written using the Euler-Rodrigues formula (cf. [123])

$$\bar{\mathbf{R}} = \mathbf{e} \otimes \mathbf{e} + \cos\varphi \, (\mathbf{I} - \mathbf{e} \otimes \mathbf{e}) + \sin\varphi \, (\mathbf{e} \times \mathbf{I}) \,, \tag{2.30}$$

where $\mathbf{e}$ is the rotation axis and φ is the rotation angle.

The relation between the line elements $\mathrm{d}\mathbf{x}$ of the actual and line elements $\mathrm{d}\mathbf{X}$ of the reference configuration is identical to the relation in the case of the classical Cauchy continuum

$$\mathrm{d}\mathbf{x} = \mathbf{F} \cdot \mathrm{d}\mathbf{X} \,, \tag{2.31}$$

with the deformation gradient $\mathbf{F}$ defined in equation (2.3).

The micropolar strain tensors (cf. [43, 44]) are defined by building a scalar product of directors and line elements of actual

$$\boldsymbol{\xi} \cdot \mathrm{d}\mathbf{x} = \bar{\mathbf{R}} \cdot \boldsymbol{\Xi} \cdot \mathbf{F} \cdot \mathrm{d}\mathbf{X} \,, \tag{2.32}$$

and reference configurations

$$\boldsymbol{\Xi} \cdot \mathrm{d}\mathbf{X} = \bar{\mathbf{R}}^T \cdot \boldsymbol{\xi} \cdot \mathbf{F}^{-1} \cdot \mathrm{d}\mathbf{x} \,, \tag{2.33}$$

followed by the difference of scalar products

$$\boldsymbol{\xi} \cdot \mathrm{d}\mathbf{x} - \boldsymbol{\Xi} \cdot \mathrm{d}\mathbf{X} = \boldsymbol{\Xi} \cdot \bar{\mathbf{E}} \cdot \mathrm{d}\mathbf{X} = \boldsymbol{\xi} \cdot \bar{\mathbf{A}} \cdot \mathrm{d}\mathbf{x}\,, \tag{2.34}$$

with the strain tensor $\bar{\mathbf{E}}$ of the reference configuration defined as

$$\bar{\mathbf{E}} = \bar{\mathbf{R}}^T \cdot \mathbf{F} - \mathbf{I}\,, \tag{2.35}$$

and strain tensor $\bar{\mathbf{A}}$ of the actual configuration defined as

$$\bar{\mathbf{A}} = \mathbf{I} - \bar{\mathbf{R}} \cdot \mathbf{F}^{-1}\,. \tag{2.36}$$

Apart from the strain tensors defined in equations (2.34 - 2.36) the curvature tensor $\overset{3}{\bar{\mathbf{K}}}$ related to the reference configuration is defined

$$\overset{3}{\bar{\mathbf{K}}} = (\bar{\mathbf{R}}^T \cdot \mathrm{Grad}\,\bar{\mathbf{R}})^{\overset{3}{-}}\,. \tag{2.37}$$

Since the curvature tensor $\overset{3}{\bar{\mathbf{K}}}$ is skew symmetric with respect to the first and second basis systems

$$\overset{3}{\bar{\mathbf{K}}} = -(\overset{3}{\bar{\mathbf{K}}})^{\overset{12}{T}}\,, \tag{2.38}$$

it can be reduced to a curvature tensor of second rank (cf. [32])

$$\bar{\mathbf{K}} = -\frac{1}{2}(\overset{3}{\bar{\mathbf{E}}} : \overset{3}{\bar{\mathbf{K}}})\,, \tag{2.39}$$

where $\overset{3}{\bar{\mathbf{E}}}$ is a permutation tensor defined as

$$\overset{3}{\bar{\mathbf{E}}} = \varepsilon_{ijk}\, \mathbf{e}_i \otimes \mathbf{e}_j \otimes \mathbf{e}_k\,, \tag{2.40}$$

$$\varepsilon_{ijk} = \begin{cases} 1: & \text{even permutation} \\ -1: & \text{odd permutation} \\ 0: & \text{else} \end{cases}\,. \tag{2.41}$$

In the case of small deformations and small rotations following linearized versions of the micromotion, curvature and strain tensors are defined (cf. [123])

$$\operatorname{lin}(\bar{\mathbf{R}}) = \mathbf{I} - \overset{3}{\bar{\mathbf{E}}} \cdot \bar{\boldsymbol{\varphi}}\,, \tag{2.42}$$

$$\bar{\boldsymbol{\kappa}} = \operatorname{Grad} \bar{\boldsymbol{\varphi}}\,, \tag{2.43}$$

$$\bar{\boldsymbol{\varepsilon}} = \operatorname{Grad} \mathbf{u} + \overset{3}{\bar{\mathbf{E}}} \cdot \bar{\boldsymbol{\varphi}}\,. \tag{2.44}$$

The linear strain measures $\bar{\boldsymbol{\varepsilon}}$ and $\bar{\boldsymbol{\kappa}}$ are interrelated with each other by the compatibility condition (cf. [123])

$$\bar{\boldsymbol{\kappa}} = \frac{1}{2}\left(\overset{3}{\bar{\mathbf{E}}} : \left(\operatorname{Grad} \bar{\boldsymbol{\varepsilon}} + \operatorname{Grad}^{\overset{12}{T}} \bar{\boldsymbol{\varepsilon}} - \operatorname{Grad}^{\overset{23}{T}} \bar{\boldsymbol{\varepsilon}}\right)\right). \tag{2.45}$$

The compatibility condition ensures that for given linear strain tensor $\bar{\boldsymbol{\varepsilon}}$ and curvature tensor $\bar{\boldsymbol{\kappa}}$ the macroscopic translational field $\mathbf{u}$ and rotational field $\bar{\boldsymbol{\varphi}}$ exist.

The micropolar strain tensor can be split into a symmetric and skew symmetric part

$$\bar{\boldsymbol{\varepsilon}} = \bar{\boldsymbol{\varepsilon}}_{sym} + \bar{\boldsymbol{\varepsilon}}_{skw}\,, \tag{2.46}$$

where the symmetric part is the linear strain tensor from the classical continuum theory

$$\bar{\boldsymbol{\varepsilon}}_{sym} = \frac{1}{2}(\operatorname{Grad} \mathbf{u} + \operatorname{Grad}^{T} \mathbf{u}) \tag{2.47}$$

and the skew symmetric part consists of the continuum rotation and the free rotation $\overset{3}{\bar{\mathbf{E}}} \cdot \bar{\boldsymbol{\varphi}}$

$$\bar{\boldsymbol{\varepsilon}}_{skw} = \frac{1}{2}(\operatorname{Grad} \mathbf{u} - \operatorname{Grad}^{T} \mathbf{u}) + \overset{3}{\bar{\mathbf{E}}} \cdot \bar{\boldsymbol{\varphi}}\,, \tag{2.48}$$

which describes the connection between the rotational degrees of freedom $\bar{\boldsymbol{\varphi}}$

and the displacement $\mathbf{u}$.

2.2.2 Translational Momentum

The local form of the translational momentum equation in the case of the micropolar continuum theory is identical with the balance equation of the pure translational formulation from the Cauchy continuum theory with the inertia forces neglected

$$\operatorname{div} \mathbf{T} + \rho\, \mathbf{b} = \mathbf{0}\,. \tag{2.49}$$

2.2.3 Rotational Momentum

The conservation law for the rotational momentum with rotational inertia neglected features the following entities linked to the rotational degrees of freedom

$$\int_B (\mathbf{x} \times \rho\, \mathbf{b} + \rho\, \mathbf{c})\, \mathrm{d}v + \int_{\partial B} (\mathbf{x} \times \mathbf{t} + \mathbf{m})\, \mathrm{d}a = \mathbf{0}\,, \tag{2.50}$$

where $\rho\mathbf{b}$ is the vector of the body forces and $\rho\mathbf{c}$ the vector of the body couples acting on the material point.

The relation between the so-called couple stress tensor $\mathbf{M}$ associated with the rotational degrees of freedom and the couple stress vector $\mathbf{m}$ is identical with the relation between the Cauchy stress tensor $\mathbf{T}$ and the traction vector $\mathbf{t}$ represented by the Cauchy theorem (2.19)

$$\mathbf{m} = \mathbf{M} \cdot \mathbf{n}\,. \tag{2.51}$$

Using the relation above in the conservation law (2.50) and applying the

divergence theorem results in

$$\int_B (\mathbf{x} \times \rho\,\mathbf{b} + \rho\,\mathbf{c} + \mathbf{x} \times \operatorname{div}\mathbf{T} + \mathbf{I} \times \mathbf{T} + \operatorname{div}\mathbf{M})\,\mathrm{d}v = \mathbf{0}\,. \tag{2.52}$$

Since the rotational momentum balance is valid for any region of the body and with the translational momentum, the conservation of rotational momentum can be rewritten in the following form

$$\mathbf{I} \times \mathbf{T} + \operatorname{div}\mathbf{M} + \rho\mathbf{c} = \mathbf{0}\,. \tag{2.53}$$

In the case of micropolar continuum theory the tensor $\mathbf{T}$ represents a Cauchy type stress tensor which lacks the symmetry property. The skew symmetric part is described by the axial vector

$$\mathbf{t} = \frac{1}{2}\,\mathbf{I} \times \mathbf{T}\,, \tag{2.54}$$

and is balanced by the divergence of the couple stresses and the body couple.

2.2.4 Constitutive Relations

In the case of linear isotropic material behavior the assumption is made that the couple stress tensor $\mathbf{M}$ is a function of the curvature tensor $\bar{\boldsymbol{\kappa}}$ and the stress tensor $\mathbf{T}$ is dependent only on the micropolar strain tensor $\bar{\boldsymbol{\varepsilon}}$ as in equation (2.44). Therefore, the material behavior can be described by the modified generalized Hooke's law (cf. [27, 28])

$$\mathbf{T} = \overset{4}{\mathbf{C}} : \bar{\boldsymbol{\varepsilon}} \tag{2.55}$$

$$= 2\mu\bar{\boldsymbol{\varepsilon}}_{sym} + 2\mu_c\bar{\boldsymbol{\varepsilon}}_{skw} + \lambda(\bar{\boldsymbol{\varepsilon}} : \mathbf{I})\,\mathbf{I}\,. \tag{2.56}$$

The material parameters μ and λ are the Lamé parameters as found in the classical continuum theory. The additional material constants is the stiffness parameter μ_c and the so-called internal length parameter l_c. The relationships

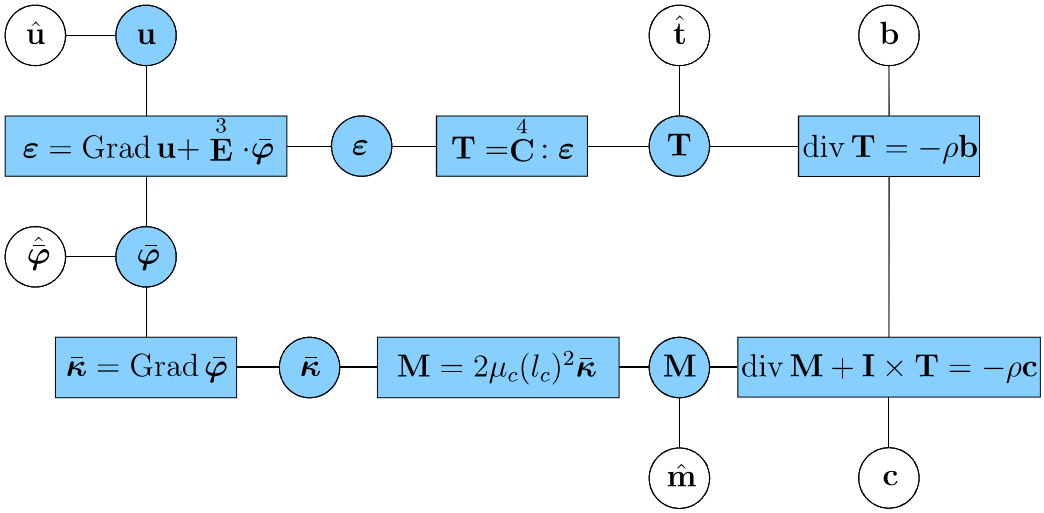

Figure 2.4: Tonti diagram of the micropolar continuum theory.

of the micropolar continuum model are visualized in figure (2.4).

In the case of the missing skew symmetric part of the micropolar strain the stress tensor is identical to the Cauchy stress from the classical continuum approach.

The relation between the couple stress tensor and curvature tensor can be written using the directly proportional relationship (cf. [27, 28])

$$\mathbf{M} = 2\,\mu_c\,(l_c)^2\,\bar{\boldsymbol{\kappa}}\,. \tag{2.57}$$

An in-depth discussion of the micropolar theory can be found e. g. in [25, 40, 44].

2.3 Order Parameter Model

One of the assumptions made in the Cauchy continuum theory is that entities on the microscopic level smaller than a material point do not provide any considerable properties or structure. Therefore, the underlying microstructure is not covered on the macro level. One possibility to include microstructural effects is given by the micropolar continuum. In this approach, the effects originating from the microstructure are introduced in a kinematical interpretation due to the existence of the micromotion.

The so-called order parameter is some characteristic value ξ representing the microstructure which is associated with a material point X. This additional parameter allows for the incorporation of the effects caused by the microstructure into the macroscopic model. The work of Capriz [19] provides in a very general way a framework for the formulation of continua with any number of additional degrees of freedom including the case of micropolar and micromorphic continua as a subset.

In contrast to the micropolar continuum theory the additional degree of freedom represented by the order parameter is not necessary an additional kinematic entity. It can represent a scalar-valued field as in the modeling of phase transitions (cf. [96, 104, 114]) or in the isotropic case of damage mechanics (cf. [65, 85, 125]). In the presented work this additional field is coupled to a linear elastic boundary value problem in terms of an extended constitutive relationship.

The starting point of the order parameter formulation used in this work is the translational momentum equation of the classical Cauchy continuum

$$\operatorname{div} \mathbf{T} + \rho \, \mathbf{b} = \mathbf{0} \,, \tag{2.58}$$

with inertia forces neglected.

The equilibrium equation is here complemented by the additional balance equation (cf. [55, 113])

$$\operatorname{div} \mathbf{S} + \hat{\kappa} = 0\,, \tag{2.59}$$

for the scalar valued order parameter $\xi(\mathbf{x}, t)$.

To obtain the relationships for the quantities $\mathbf{S}$, $\mathbf{T}$ and $\hat{\kappa}$ in equations (2.58 - 2.59) the second law of thermodynamics is evaluated in the sense of Coleman and Noll (cf. [23]). This derivation procedure is consistent with the argumentation pattern as proposed in [19, 64, 113, 116].

The second law of thermodynamics is stated in the form of an extended *Clausius-Duhem* inequality

$$-\rho\dot{\Psi} + \mathbf{T} \,:\, \operatorname{grad}\dot{\mathbf{x}} + \mathbf{S}\cdot\operatorname{grad}\dot{\xi} - \hat{\kappa}\,\dot{\xi} - \rho\,\eta\,\dot{\theta} - \frac{\mathbf{q}}{\theta}\cdot\operatorname{grad}\theta \geq 0\,, \tag{2.60}$$

with $\dot{\Psi}$ as the time rate change of the *Helmholtz* free energy Ψ, η as the entropy, θ as the absolute temperature, and $\mathbf{q}$ as the heat flux vector.

With the assumption of the isothermal case the statement (2.60) is reduced to an extended *Clausius-Planck* inequality

$$-\rho\dot{\Psi} + \mathbf{T} \,:\, \operatorname{grad}\dot{\mathbf{x}} + \mathbf{S}\cdot\operatorname{grad}\dot{\xi} - \hat{\kappa}\,\dot{\xi} \geq 0\,. \tag{2.61}$$

The Clausius-Planck inequality is evaluated with the Helmholtz free energy function chosen as

$$\Psi = \Psi\left(\mathbf{E}, \xi, \operatorname{grad}\xi\right). \tag{2.62}$$

The arguments of the function above are the process variables with the set of response functions

$$\mathcal{R} = \mathcal{R}\left(\Psi, \mathbf{T}, \mathbf{S}, \hat{\kappa}\right). \tag{2.63}$$

With the concept of equipresence it is assumed that every response function is dependent on each process variable. The rate of change of the Helmholtz free energy reads

$$\dot{\Psi} = \frac{\partial \Psi}{\partial \mathbf{E}} \,:\, \dot{\mathbf{E}} + \frac{\partial \Psi}{\partial \xi}\,\dot{\xi} + \frac{\partial \Psi}{\partial\, \mathrm{grad}\, \xi} \cdot (\mathrm{grad}\, \xi)^{\cdot}\,. \tag{2.64}$$

Inserting the rate of change expression into inequality (2.61) and rearranging the terms provides

$$\left(\mathbf{T} - \rho\, \mathbf{F} \cdot \frac{\partial \Psi}{\partial \mathbf{E}} \cdot \mathbf{F}^T\right) : \mathbf{D} + \left(\mathbf{S} - \rho \frac{\partial \Psi}{\partial\, \mathrm{grad}\, \xi}\right) \cdot (\mathrm{grad}\, \xi)^{\cdot} + \left(-\hat{\kappa} - \rho \frac{\partial \Psi}{\partial \xi}\right) \dot{\xi} \geq 0\,. \tag{2.65}$$

The standard Coleman and Noll evaluation procedure (cf. [23]) implies that the inequality (2.61) should be fulfilled for any $\mathbf{D}$, $\dot{\xi}$ or $(\mathrm{grad}\, \xi)^{\cdot}$ and leads to the following constitutive relationships

$$\mathbf{T} = \rho\, \mathbf{F} \cdot \frac{\partial \Psi}{\partial \mathbf{E}} \cdot \mathbf{F}^T\,, \tag{2.66}$$

$$\mathbf{S} = \rho \frac{\partial \Psi}{\partial\, \mathrm{grad}\, \xi}\,, \tag{2.67}$$

$$\hat{\kappa} = -\rho \frac{\partial \Psi}{\partial \xi}\,. \tag{2.68}$$

With the Helmholtz free energy chosen as a quadratic function of its arguments

$$\rho\Psi = \frac{1}{2}\lambda(\mathbf{E} \,:\, \mathbf{I})^2 + \mu(\xi)\, \mathbf{E} \,:\, \mathbf{E} + \frac{1}{2}\alpha\, \xi^2 + \frac{1}{2}\beta(\mathrm{grad}\, \xi)^2\,, \tag{2.69}$$

the following set of constitutive equations is obtained:

$$\mathbf{T} = \rho\,\mathbf{F}\cdot\frac{\partial\Psi}{\partial\mathbf{E}}\cdot\mathbf{F}^T = \rho\,\mathbf{F}\cdot\Big(2\,\mu(\xi)\,\mathbf{E} + \lambda(\xi)\,(\mathbf{E}\,:\,\mathbf{I})\,\mathbf{I}\Big)\cdot\mathbf{F}^T\,, \tag{2.70}$$

$$\mathbf{S} = \rho\,\frac{\partial\Psi}{\partial\,\mathrm{grad}\,\xi} = \beta\,\mathrm{grad}\,\xi\,, \tag{2.71}$$

$$\hat{\kappa} = -\rho\frac{\partial\Psi}{\partial\xi} = -\alpha\,\xi - \frac{\partial\mu(\xi)}{\partial\xi}\,\mathbf{E}\,:\,\mathbf{E}\,. \tag{2.72}$$

In the context of small deformations the Green strain tensor $\mathbf{E}$ can be replaced by the linear strain tensor $\boldsymbol{\varepsilon}$

$$\mathbf{E} \approx \boldsymbol{\varepsilon} = \frac{1}{2}(\mathrm{Grad}\,\mathbf{u} + \mathrm{Grad}^{\,T}\mathbf{u})\,. \tag{2.73}$$

With the linear strain tensor the corresponding form of the constitutive equation (2.70) reads

$$\mathbf{T} = 2\,\mu(\xi)\,\boldsymbol{\varepsilon} + \lambda\,(\mathrm{tr}\,\boldsymbol{\varepsilon})\,\mathbf{I}\,. \tag{2.74}$$

The material parameters $\mu(\xi)$ and $\lambda(\xi)$ represent the local Lamé parameters of the linear elasticity, while the parameters α and β are linked to the order parameter field. The material function $\mu(\xi)$ controls the distribution of the shear modulus and couples the order parameter field to the displacement field, hence, providing an extended form of equation (2.28). For simplicity λ will be assumed constant.

Depending on the applied modeling approach the order parameter and displacement fields can be coupled through constitutive, kinematic or balance relationships. The formulation of the order parameter boundary value problem is shown in figure (2.5).

In equation (2.72), the quadratic term $(\mathbf{E}\,:\,\mathbf{E})$ is neglected due to the assumption of small strains. With the relationships obtained in equations (2.71 - 2.72) the balance equation of the order parameter field can be

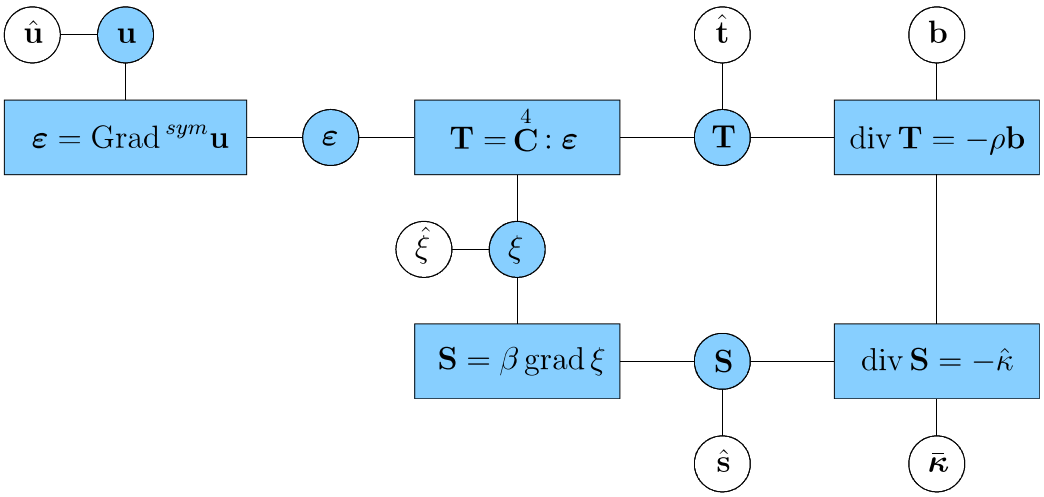

Figure 2.5: Tonti diagram of the order parameter model.

rewritten in the following form

$$\mathrm{div}\,(\beta\,\mathrm{grad}\,\xi) - \alpha\,\xi = 0\,. \tag{2.75}$$

The obtained balance equation (2.75) can be classified as an elliptic partial differential equation of *Helmholtz* type.

3

Application to Size Effect Modeling

In the present chapter the application of the order parameter model is discussed with regard to prediction of size effect phenomena characteristic for the materials with distinctive microstructure such as cellular materials. The order parameter approach is compared to the micropolar theory with regard to macroscopic modeling of size effects.

Furthermore, the subject of the identification of respective model parameters is discussed. The reference for both macroscopic models treated in this chapter is provided by a high-resolution micromechanical foam model based on the Weaire-Phelan structure.

3.1 Size Effect Modeling

The dependency of the mechanical properties on the ratio of the specimen size to the cell size is a property specific to the cellular materials such as cancellous bone, cork, polymer and metal foams. This so-called size effect is most notably observable, when the cell size and specimen size are of the same order of magnitude (cf. [51]). This microstructure initiated effect cannot be captured within the framework of the scale invariant approach such as Cauchy continuum, where the mechanical behavior in the case of small deformations is controlled by only two material constants (i. e. extended continuum models feature additional material parameters such as length scale parameter and additional stiffness as in the micropolar approach).

The size effect modeling techniques can be classified into three main groups:

micromechanical

macroscopic

mixed/multiscale

In the micromechanical approach the microscale structure is resolved in detail using standard structural finite elements (e. g. beam elements, cf. [34, 50, 100, 120]).

In contrast to the micromechanical approach, the macroscopic approach treats foam material as a continuous medium, either in the context of classical continuum mechanics or, taking size effects into account, in the framework of extended continuum mechanics, hence, introducing the additional field equations. However, the formulation of the extended continuum is not necessarily related to additional field variables as in the case of strain-gradient theories (cf. [93, 94]).

The multiscale models describe the material behavior on the macroscale based on homogenization strategies which explicitly use the information from underlying scales. Hence, additional boundary value problems for the microstructure are solved. This procedure leads for example to the so-called FE^2 models (cf. [38, 45, 63, 90]).

In the present work, two types of size effect are investigated: the stiffening effect under shear loading and the weakening effect under tensile loading.

3.2 Micromechanical Model

In the micromechanical model presented here, the microstructure of an open-cell foam is resolved by means of finite elements to provide a detailed reference model. The reference data is obtained in virtual experiments carried out on an idealized and explicitly resolved foam structure.

The reference microstructure is based on the unit cell resulting from the solution of the Kelvin's Problem, which deals with the question of space partitioning with the cells of equal volume and with minimal surface between the cells.

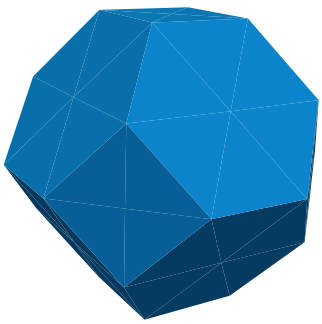

Figure 3.1: Truncated octahedron.

The *Kelvin's conjecture* states that the structure based on bitruncated cubic honeycomb, which in turn consists of four truncated octahedra (figure 3.1) around each vertex, is the most efficient solution of the space partitioning problem (cf. [121]).

The *Weaire-Phelan* structure (cf. [127]) is a periodic cell consisting of eight subcells (six tetradecahedra and two irregular pentagonal dodecahedra, figure 3.2) and provides a more efficient solution of the Kelvin problem. It allows for the implementation of closed-cell and open-cell foams as well.

The Weaire-Phelan structure will be used as a basis for the creation of artificial cellular structures in the present work.

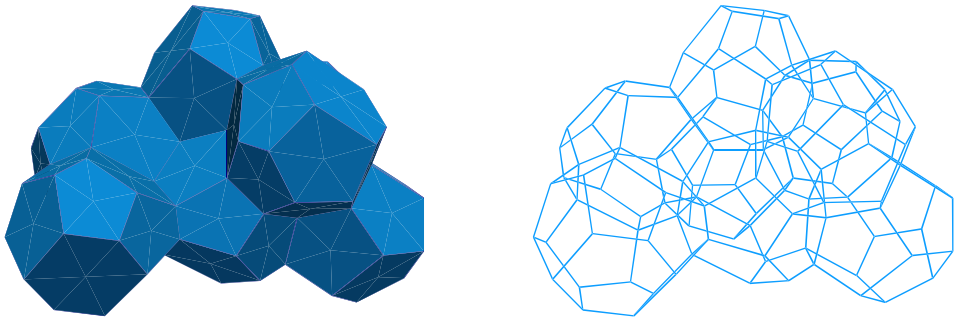

Figure 3.2: Idealized foam material: Weaire-Phelan structure (left) and its discretization with beam elements (right).

Due to the periodic nature of the Weaire-Phelan cell it is possible to efficiently generate large samples of idealized foams. The edges of polyhedra in the Weaire-Phelan cell represent the struts of an open-cell foam (figure 3.2). This idealized geometry is, therefore, discretized with linear Timoshenko beam elements with a constant square cross-section of 0.16 mm^2. The length of the struts of the Weaire-Phelan cell varies between 2.772 mm and 6.3 mm. With these values the average strut length amounts to 4.536 mm.

The degrees of freedom comprise translations $\mathbf{u}$ and rotations of the beam

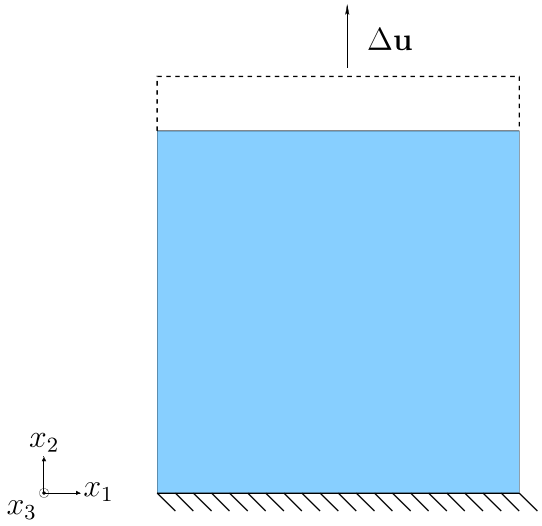

Figure 3.3: Micromechanical model. Boundary conditions of tensile test.

cross-section φ. By using beam elements a detailed description of the microstructural geometry is provided. Depending on the specimen's dimensions this approach involves the solution of a system with a large number of unknowns. Due to this disadvantage the micromechanical model is only used as a source of reference data.

The advantage of the micromechanical model is that the individual parameters of the foam microstructure can be changed independently and the boundary conditions of the virtual experiments can be exactly controlled. Furthermore, all required information can be extracted from the virtual micromechanical model while this is not possible in the real experiment.

The simulations were performed using the finite element analysis solver RADIOSS® [106]. The standard shear and tensile tests were carried out on Weaire-Phelan based structures to determine the effective material parameters such as Lamé constants.

Since the order parameter and micropolar approaches used in this work are covering the isotropic material behavior, the isotropy of the reference micromechanical models is examined in the following.

direction	E [MPa]	ν_1	ν_2
x_1	112.83	0.44	0.41
x_2	82.63	0.40	0.39
x_3	82.91	0.37	0.39
SD	17.35	0.03	0.1

Table 3.1: Regular structure. Results of tension tests in 3 directions and corresponding standard deviations (SD).

Figure (3.3) shows the boundary conditions used in the simulation of the tensile test. The tensile tests performed in 3 orthogonal directions indicate the slightly anisotropic behavior of the regular Weaire-Phelan structures (figure 3.4, left). The obtained values of the effective elastic moduli and Poisson's ratios are listed in table (3.1).

The anisotropic behavior of the regular structure can be attributed to the composition of the single Weaire-Phelan cell and the alignment of its particular edges. Although both polyhedron types of the unit cell have nearly the same volume there are great differences in edge lengths: the length of the shortest edge is only about a half of the longest edge length. These dif-

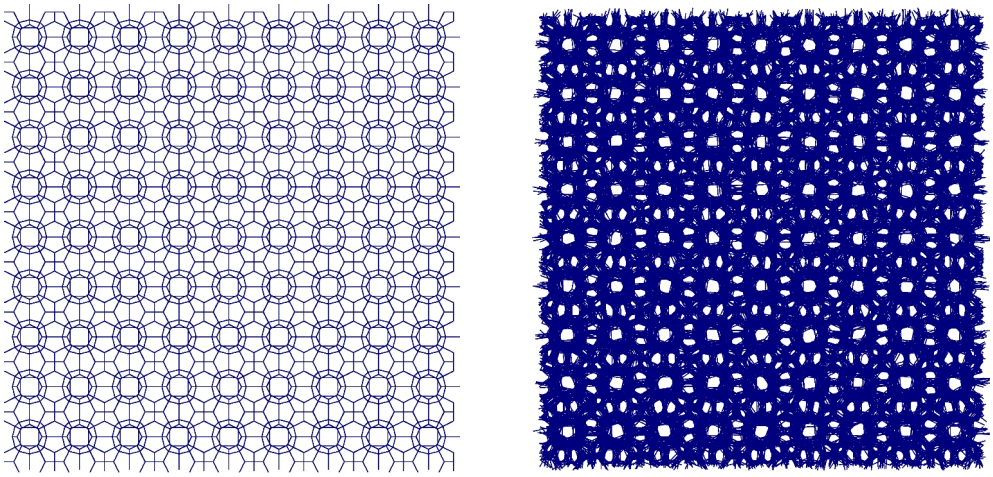

Figure 3.4: Weaire-Phelan specimen: regular (left) and stochastically disturbed (right) structure.

direction	E [MPa]	ν_1	ν_2
x_1	56.43	0.18	0.17
x_2	56.25	0.17	0.17
x_3	53.72	0.16	0.17
SD	1.51	0.01	0.0

Table 3.2: Stochastically disturbed structure. Results of tension tests in 3 directions and corresponding standard deviations.

ferences are reflected in variations of the stiffness values of the polyhedron structures.

To resolve the anisotropy issue of the structures based on regular Weaire-Phelan cell the vertex coordinates have been stochastically disturbed (figure 3.4, right). As a result, the edge lengths and edge orientations were changed and the new disturbed structure reveals mechanical properties nearly independent from the direction. The values of the effective elastic moduli and Poisson's ratios of the disturbed structure are listed in table (3.2).

The comparison of the standard deviation (SD) values listed in table (3.1) and (3.2) indicates that the mechanical properties of the disturbed structure can be considered as nearly isotropic. In the following, the results obtained in tests on disturbed structure will be used as a reference.

The size effect is investigated using a set of simple shear and tensile tests performed on the micromechanical samples.

3.2.1 Simple Shear Test

The boundary conditions of the micromechanical simple shear problem are displayed in figure (3.5). The clamping boundary conditions applied at the top and the bottom of the specimen simulate glued load plates as used in field experiments (figure 3.6).

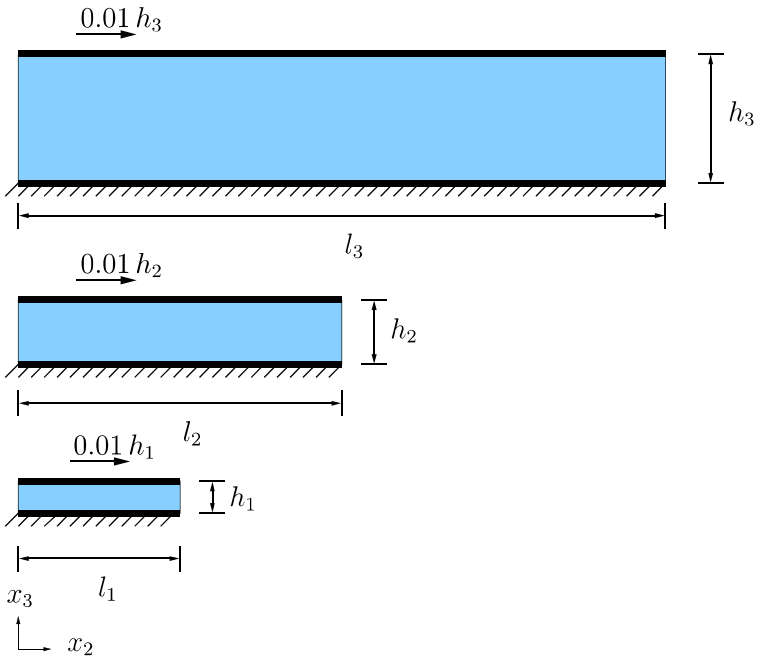

Figure 3.5: Geometrically similar specimens. Boundary conditions of the shear problem.

The length of each specimen is 10 times the height value, i. e. $l_i/h_i = 10$. The shear deformation in all cases amounts to 0.01. The simple shear tests carried out on geometrically similar specimens of different size but constant microstructure (figure 3.5) exhibit the dependency of the effective mechanical

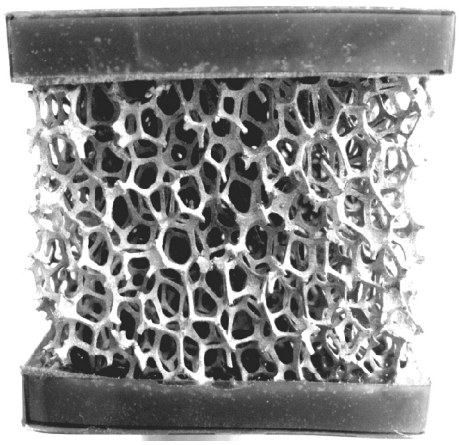

Figure 3.6: Open-cell foam specimen with glued load plates.

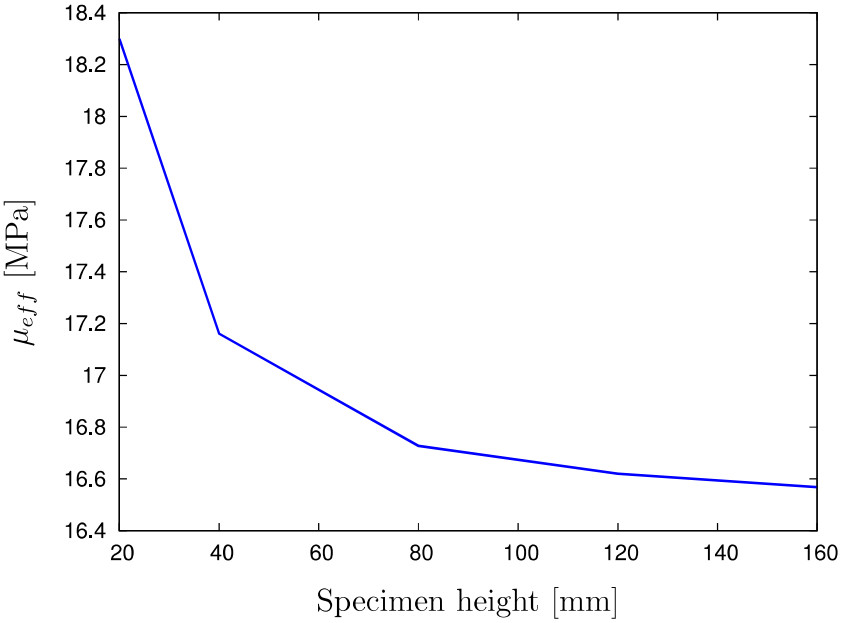

Figure 3.7: Micromechanical model. Size effect in simple shear experiments.

properties on the specimen size, which is a characteristic feature of cellular materials (cf. [33, 100, 108]). Figure (3.7) shows the effective shear modulus

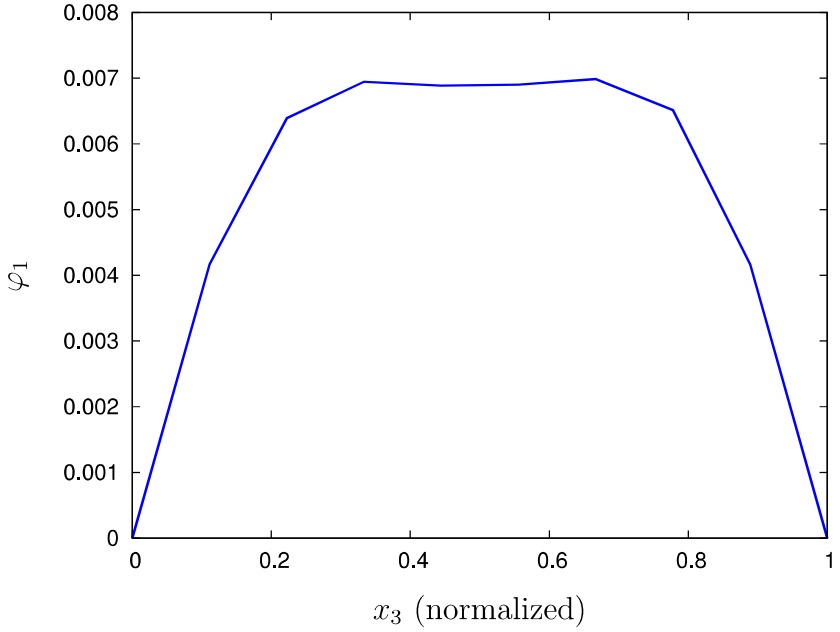

Figure 3.8: Micromechanical model. Distribution of average values of rotations.

as a function of the specimen height. The obtained result reveals the presence of a size effect in the form such as "smaller is stiffer".

The averaged distribution of the rotational degrees of freedom φ_1 obtained in the shear test is presented in figure (3.8). The inspection of the solution for the rotational degrees of freedom indicates the presence of the boundary layer. The clamping boundary conditions, which restrict the rotational degrees of freedom, lead to the appearance of a boundary layer resulting in turn in size-dependent macroscopic properties of the model (cf. [33]).

3.2.2 Tensile Test

The boundary conditions of the micromechanical tensile test problem used to investigate scale effects in tension are displayed in figure (3.9).

The performed tensile tests show the dependency of the effective elastic modulus from specimen size, which is, however, different from the effect observed under shear loading. Here, the larger specimens have increasing values of elastic moduli. The opposite effect of decreasing compressive strength is documented in [3, 6]. The results of tensile tests are depicted in figure (3.10).

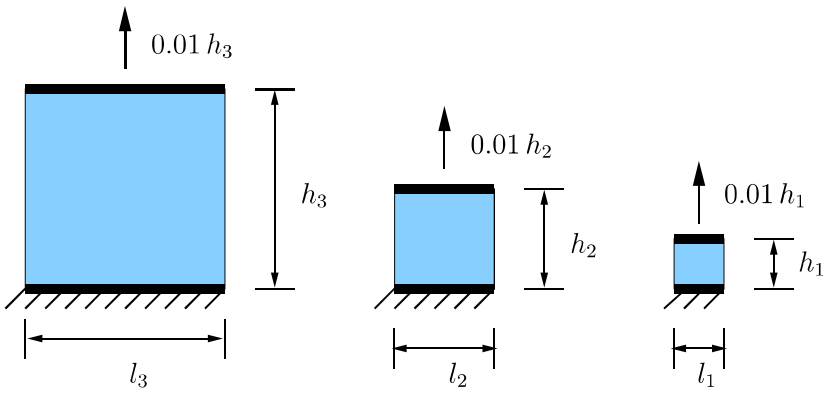

Figure 3.9: Geometrically similar specimens. Boundary conditions of the tensile test.

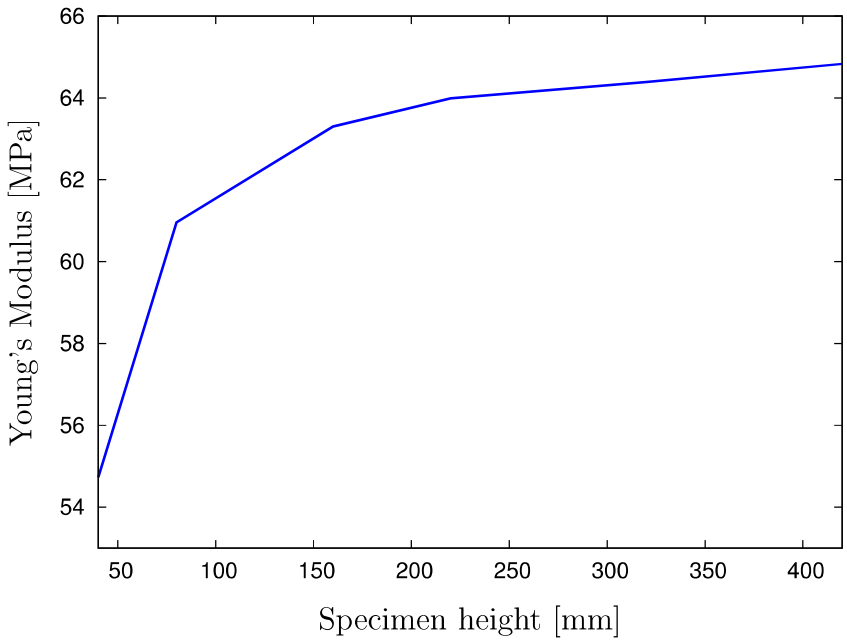

Figure 3.10: Micromechanical model. Size effect in tensile loading.

To motivate the weakening effect observed in tensile tests the constraints of foam cells within the specimen and on its unloaded boundaries have to be considered. The cells on the boundary have less neighbors than the cells in the bulk of the sample. Therefore, these cells are less restricted in their movements (cf. [119]).

3.3 Modeling by Micropolar Approach

In order to model the size effects observed in virtual experiments an extended continuum model is chosen on the macroscale. The extended continuum theories introduce additional degrees of freedom for each material point (cf. [43]). This additional information can be linked to the underlying microstructure of a statistically inhomogeneous body, so that it can be replaced with a macroscopic homogeneous one. In case of the extended continuum theory as proposed by brothers Cosserat [25], the material point is considered as a rigid body on the microscale. Thus, the translational degrees of freedom $\mathbf{u}$ are complemented by rotational degrees of freedom $\bar{\boldsymbol{\varphi}}$.

The rotational degrees of freedom are independent from the translational ones and do not scale with the displacement field. Hence, the influence of rotations increases with decreasing size of the specimen. This characteristic property provides the means to reproduce the size effect observed in shear

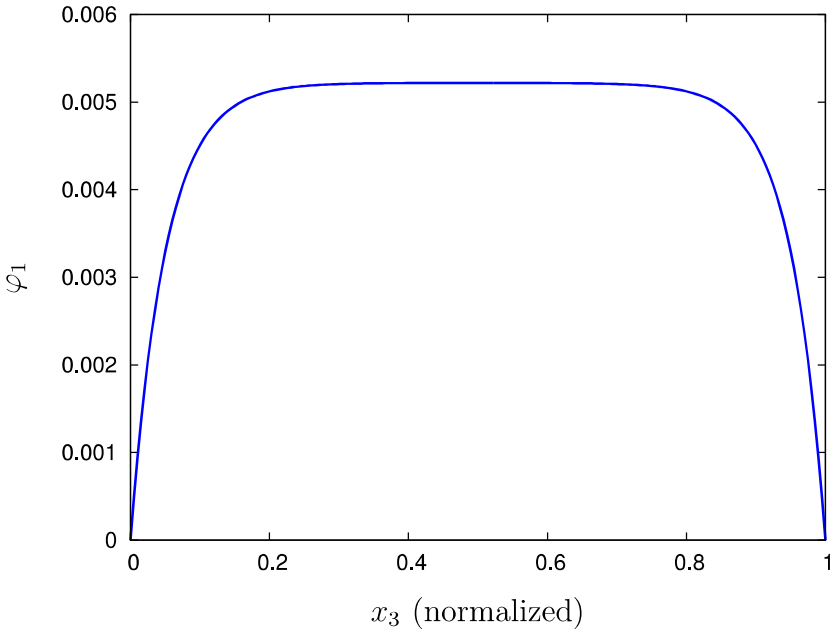

Figure 3.11: Micropolar model. Distribution of rotations under shear loading.

tests performed on micromechanical models (cf. section 3.2).

The solution of the rotational degrees of freedom obtained in the simple shear test (figure 3.11) shows the presence of the boundary layer and corresponds to constraints resulting from the boundary conditions applied in tests (cf. [119]).

3.3.1 Boundary Value Problem Formulation

The formulation of the boundary value problem of the quasi-static micropolar model contains apart from the kinematic relationships, constitutive relationships, and balance equations, also the boundary conditions applied to the boundary Γ of the material body.

On the boundaries Γ_u^D and Γ_φ^D the Dirichlet boundary conditions for the translational

$$\mathbf{u} = \hat{\mathbf{u}} \quad \text{on} \quad \Gamma_u^D \,, \tag{3.1}$$

and rotational degrees of freedom

$$\bar{\boldsymbol{\varphi}} = \hat{\bar{\boldsymbol{\varphi}}} \quad \text{on} \quad \Gamma_\varphi^D \,, \tag{3.2}$$

are prescribed.

On the boundaries Γ_u^N and Γ_φ^N the Neumann boundary conditions for the stress

$$\mathbf{T} \cdot \mathbf{n} = \hat{\mathbf{t}} \quad \text{on} \quad \Gamma_u^N \,, \tag{3.3}$$

and couple stress

$$\mathbf{M} \cdot \mathbf{n} = \hat{\mathbf{m}} \quad \text{on} \quad \Gamma_\varphi^N \,, \tag{3.4}$$

with $\mathbf{n}$ as an outward pointing normal to the boundary Γ are applied.

Furthermore, following conditions are imposed on the boundaries

$$\Gamma_u^D \cup \Gamma_u^N = \Gamma \quad \wedge \quad \Gamma_u^D \cap \Gamma_u^N = \emptyset\,, \tag{3.5}$$

$$\Gamma_\varphi^D \cup \Gamma_\varphi^N = \Gamma \quad \wedge \quad \Gamma_\varphi^D \cap \Gamma_\varphi^N = \emptyset\,. \tag{3.6}$$

The equilibrium equations

$$\operatorname{div} \mathbf{T} = \mathbf{0}\,, \tag{3.7}$$

$$\operatorname{div} \mathbf{M} + \mathbf{I} \times \mathbf{T} = \mathbf{0}\,, \tag{3.8}$$

together with the boundary conditions, and the kinematic and constitutive relationships form the strong form of the micropolar boundary value problem.

3.3.2 Weak Formulation

The weak form of the micropolar boundary value problem is obtained by multiplication of the translational momentum (equation 2.49) as well as rotational momentum (equation 2.50) equations with the test functions $\boldsymbol{v} \in \{\delta\mathbf{u}, \delta\bar{\boldsymbol{\varphi}}\}$, followed by integration over the domain Ω with the boundary Γ

$$\int_\Omega \delta\mathbf{u} \cdot \operatorname{div} \mathbf{T}\, \mathrm{d}\Omega = \mathbf{0}\,, \qquad \forall\, \delta\mathbf{u} \in \tilde{\mathcal{U}}\,, \tag{3.9}$$

$$\int_\Omega \delta\bar{\boldsymbol{\varphi}} \cdot \Big[\operatorname{div} \mathbf{M} + \mathbf{I} \times \mathbf{T}\Big]\, \mathrm{d}\Omega = \mathbf{0}\,, \qquad \forall\, \delta\bar{\boldsymbol{\varphi}} \in \tilde{\Phi}\,, \tag{3.10}$$

$$\tilde{\mathcal{U}} := \Big\{\delta\mathbf{u} \in \mathcal{H}^1(\Omega), \quad \delta\mathbf{u}|_{\Gamma_u^D} = \mathbf{0}\Big\}\,, \tag{3.11}$$

$$\tilde{\Phi} := \Big\{\delta\bar{\boldsymbol{\varphi}} \in \mathcal{H}^1(\Omega), \quad \delta\bar{\boldsymbol{\varphi}}|_{\Gamma_\varphi^D} = \mathbf{0}\Big\}\,. \tag{3.12}$$

Applying integration by parts and using the divergence theorem we obtain

$$\int_{\Omega} \operatorname{grad} \delta\mathbf{u} \cdot \mathbf{T} \, \mathrm{d}\Omega = \int_{\Gamma_u^N} \delta\mathbf{u} \cdot \hat{\mathbf{t}} \, \mathrm{d}\Gamma \,, \tag{3.13}$$

$$\int_{\Omega} \left[\operatorname{grad} \delta\bar{\boldsymbol{\varphi}} \cdot \mathbf{M} - \delta\bar{\boldsymbol{\varphi}} \cdot \mathbf{I} \times \mathbf{T} \right] \mathrm{d}\Omega = \int_{\Gamma_{\varphi}^N} \delta\bar{\boldsymbol{\varphi}} \cdot \hat{\mathbf{m}} \, \mathrm{d}\Gamma \,. \tag{3.14}$$

The solution $\boldsymbol{u} \in \{\mathbf{u}, \bar{\boldsymbol{\varphi}}\}$ for the translational as well as rotational degrees of freedom lies in the function space $\mathcal{U} \times \Phi$ with

$$\mathcal{U} := \left\{ \mathbf{u} \in \mathcal{H}^1(\Omega), \quad \mathbf{u}|_{\Gamma_u^D} = \hat{\mathbf{u}} \right\} , \tag{3.15}$$

$$\Phi := \left\{ \bar{\boldsymbol{\varphi}} \in \mathcal{H}^1(\Omega), \quad \bar{\boldsymbol{\varphi}}|_{\Gamma_{\varphi}^D} = \hat{\bar{\boldsymbol{\varphi}}} \right\} . \tag{3.16}$$

The Sobolev space $\mathcal{H}^1$ is the space of square integrable functions v with finite integrals for v^2 and $|\nabla v|$ over domain Ω.

The variational formulation of the micropolar problem reads as follows:
Find $\boldsymbol{u} \in \mathcal{U} \times \Phi$ such that

$$a(\boldsymbol{u}, \boldsymbol{v}) = l(\boldsymbol{v}) \,, \quad \forall \, \boldsymbol{v} \in \tilde{\mathcal{U}} \times \tilde{\Phi} \,. \tag{3.17}$$

In the present problem we have

$$a(\boldsymbol{u}, \boldsymbol{v}) := \int_{\Omega} \left[\operatorname{grad} \delta\mathbf{u} \cdot \mathbf{T} + \operatorname{grad} \delta\bar{\boldsymbol{\varphi}} \cdot \mathbf{M} - \delta\bar{\boldsymbol{\varphi}} \cdot \mathbf{I} \times \mathbf{T} \right] \mathrm{d}\Omega \,, \tag{3.18}$$

$$l(\boldsymbol{v}) := \int_{\Gamma_u^N} \delta\mathbf{u} \cdot \hat{\mathbf{t}} \, \mathrm{d}\Gamma + \int_{\Gamma_{\varphi}^N} \delta\bar{\boldsymbol{\varphi}} \cdot \hat{\mathbf{m}} \, \mathrm{d}\Gamma \,. \tag{3.19}$$

The numerical solution $\boldsymbol{u}_h$ of the micropolar model is obtained by casting the continuous variational problem (3.17) into a discrete variational problem with functions lying in the finite-dimensional function spaces based on the

geometric triangulation $\mathcal{T}$ of the domain Ω

$$\boldsymbol{v}_h \in \tilde{\mathcal{U}}_h \times \tilde{\Phi}_h \subset \tilde{\mathcal{U}} \times \tilde{\Phi}\,, \quad \boldsymbol{v}_h \in \{\delta\mathbf{u}_h, \delta\bar{\boldsymbol{\varphi}}_h\}\,, \tag{3.20}$$

$$\boldsymbol{u}_h \in \mathcal{U}_h \times \Phi_h \subset \mathcal{U} \times \Phi\,, \quad \boldsymbol{u}_h \in \{\mathbf{u}_h, \bar{\boldsymbol{\varphi}}_h\}\,. \tag{3.21}$$

The discrete variational problem can now be stated as:
Find $\boldsymbol{u}_h$ such that

$$a(\boldsymbol{u}_h, \boldsymbol{v}_h) = l(\boldsymbol{v}_h)\,. \tag{3.22}$$

The approximations $\mathbf{u}_h$ and $\bar{\boldsymbol{\varphi}}_h$ are formulated using shape functions $\mathbf{N}^i$ and $\mathbf{M}^i$ with corresponding unknown expansion coefficients $\mathbf{u}^i$ and $\bar{\boldsymbol{\varphi}}^i$

$$\mathbf{u}_h = \sum_i \mathbf{N}^i(\mathbf{x})\,\mathbf{u}^i\,, \tag{3.23}$$

$$\bar{\boldsymbol{\varphi}}_h = \sum_i \mathbf{M}^i(\mathbf{x})\,\bar{\boldsymbol{\varphi}}^i\,. \tag{3.24}$$

In the present work the translational and rotational degrees of freedom utilize the same finite element shape functions. However, a mixed formulation, where the different physical degrees of freedom make use of different shape functions, is also possible (cf. [4, 118, 128]).

The test functions $\boldsymbol{v}_h$ are approximated with the same set of functions as used for the solution approximation $\boldsymbol{u}_h$. This procedure corresponds to the standard Galerkin method (cf. [7, 109])

$$\boldsymbol{v}_h = \sum_i \mathbf{N}^i(\mathbf{x})\,. \tag{3.25}$$

3.3.3 Numerical Examples

The size effect is investigated by performing the simple shear test on a set of geometrically similar specimens. Figure (3.12) shows the boundary conditions used in simulations.

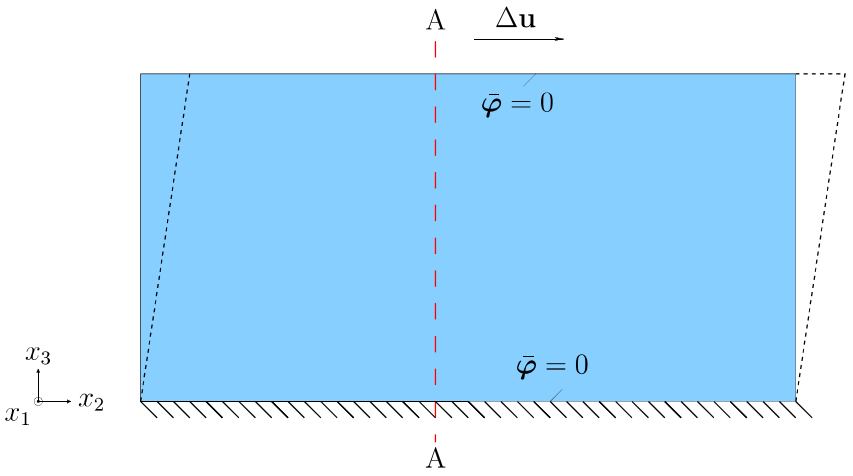

Figure 3.12: Micropolar model. Boundary conditions of simple shear test.

Figure (3.13) shows the values of the effective shear modulus obtained using linear micropolar model. The characteristic length parameter l_c controls the thickness of the boundary layer. Small values of the length parameter decrease the size of the boundary layer.

The variation of the internal length parameter l_c has a direct effect on the macroscopic stiffness μ_{eff} (figure 3.13). These results confirm the capability of the micropolar approach to describe the size effect under shear loading on macroscopic level. Figure (3.14) displays the solutions for the rotational degrees of freedom obtained with different values of l_c.

The parameter μ_c controls the stiffness of the boundary layer. Higher values of this parameter have an effect of lower magnitudes of rotations. Figure (3.15) depicts the solutions for the rotational degrees of freedom obtained with different values of the parameter μ_c.

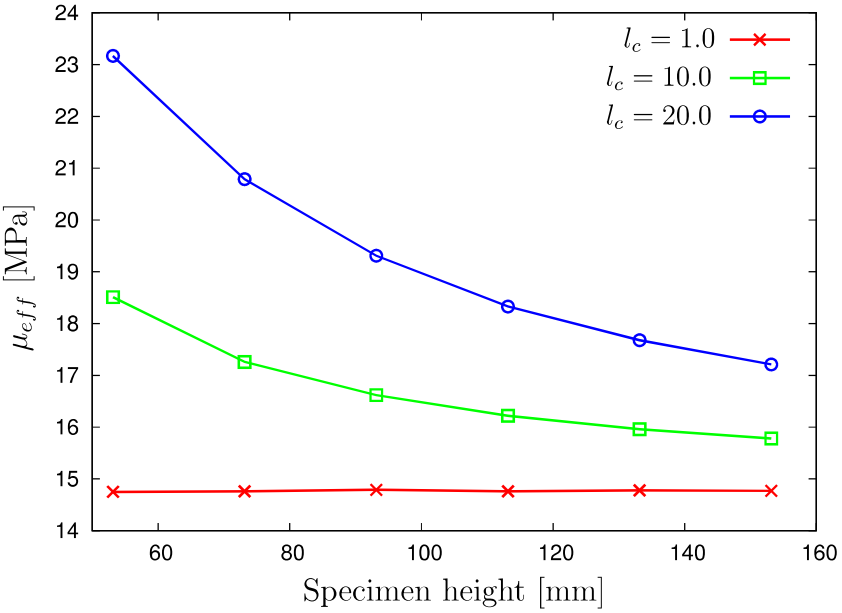

Figure 3.13: Size effect modeled with micropolar approach.

Contrary to the results obtained in tests using micromechanical models, the micropolar approach fails to predict the size effect under tensile loading. This is motivated by the fact that the rotational degrees of freedom are not being

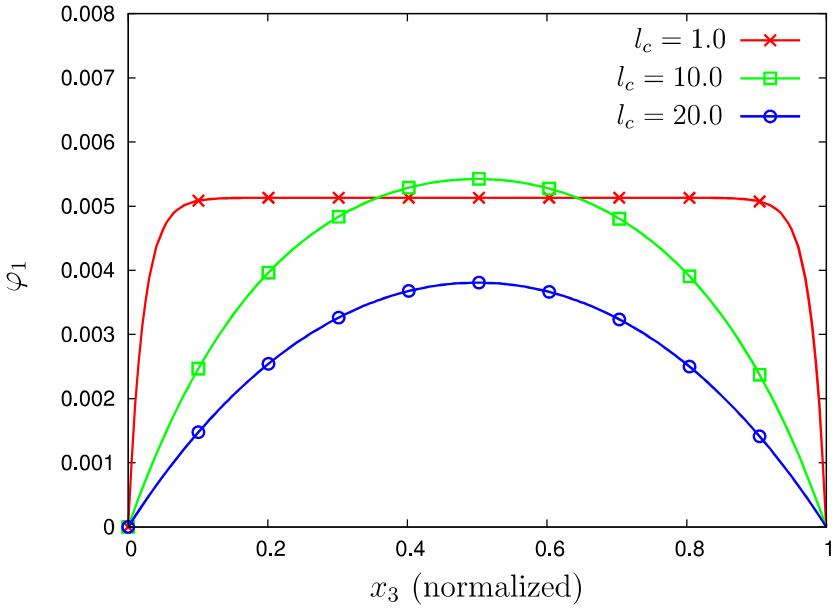

Figure 3.14: Parameter study. Characteristic length l_c.

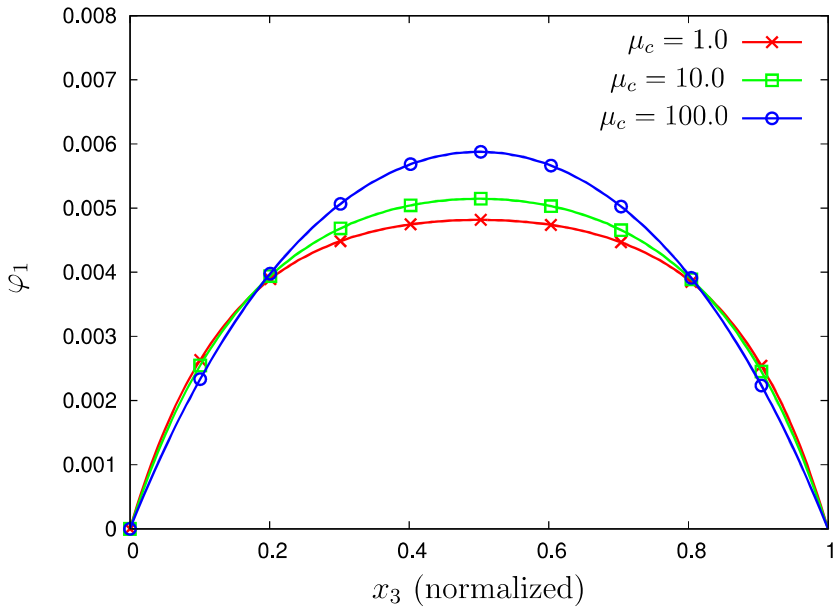

Figure 3.15: Parameter study. Stiffness μ_c.

activated in tension. In this case the solution delivered by the micropolar theory is identical to the solution obtained using the classical continuum theory (cf. [119]).

To quantitatively reproduce the mechanical behavior of the micromechanical model with the micropolar model on macroscopic level a set of suitable model parameters (Lamé parameters μ and λ plus the additional micropolar parameters l_c and μ_c) has to be determined. The identification of these parameters involves a solution of an inverse problem and will be discussed in the subsequent section.

3.4 Modeling by Order Parameter Approach

The order parameter formulation is investigated as an alternative to the micropolar approach with regard to modeling of the size effects. The distribution of the order parameter variable (figure 3.16) shows the presence of a boundary layer similar to the distribution of rotations from the micromechanical (figure 3.8) and the micropolar (figure 3.11) problems.

The order parameter field complements the linear elasticity problem as an additional field controlling the spatial distribution of stiffness and, therefore, used to reproduce a boundary layer observed in experiments.

The thickness of the boundary layer independent from the specimen size can be reproduced by incorporating the linear mixture rule

$$\mu(\xi) = (1-\xi)\mu_1 + \xi\mu_2 \tag{3.26}$$

into the order parameter formulation. The parameter μ_1 represents the local

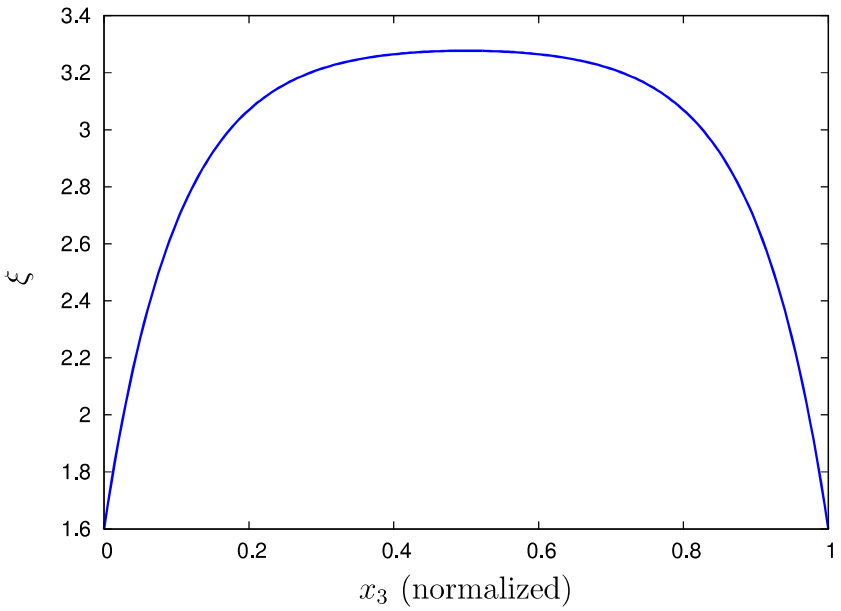

Figure 3.16: Distribution of the order parameter.

stiffness in the bulk material of the sample and the material parameter μ_2 describes the stiffness in the region close to the boundary of the sample.

In contrast to the micropolar approach with translational and rotational degrees of freedom, the order parameter model is a formulation based on the classical Cauchy continuum with translational degrees of freedom only. Hence, the equilibrium equation and kinematics are identical with the corresponding relations in the theory of linear elasticity. This way the symmetry of the strain tensor $\mathbf{E}$ used in the order parameter model is preserved, contrary to the unsymmetrical micropolar strain measure $\bar{\boldsymbol{\varepsilon}}$.

Both micropolar and order parameter approaches represent an extended continuum model. However, while the micropolar theory is an example of kinematically extended continuum, the order parameter setting extends the classical continuum model at the level of the constitutive relations and acts as a non-kinematic quantity.

The main advantage of the order parameter approach compared to the micropolar model setting is the capability to reproduce the size effect under tensile and compressive loadings, while the micropolar approach is able to describe the size-dependent behavior in shear test only.

Another advantage of the order parameter model refers to the computational efficiency. Compared to the micropolar model with six degrees of freedom (three translational plus three rotational) the order parameter model exhibits a lower numerical complexity since a total number of four degrees of freedom (three classical translational plus one additional degree of freedom of order parameter field) is used.

3.4.1 Boundary Value Problem Formulation

The boundary value problem of the order parameter approach is composed of the relationships of linear elasticity and an additional order parameter

equilibrium equation. The boundary value problem is completed by the set of boundary conditions imposed on the material body.

The Dirichlet boundary conditions are prescribed for the kinematic degrees of freedom

$$\mathbf{u} = \hat{\mathbf{u}} \quad \text{on} \quad \Gamma_u^D \,, \tag{3.27}$$

and for the degrees of freedom associated with the order parameter field

$$\xi = \hat{\xi} \quad \text{on} \quad \Gamma_\xi^D \,. \tag{3.28}$$

The Neumann boundary conditions are prescribed on the boundaries Γ_u^N and Γ_ξ^N for the kinematic degrees of freedom

$$\mathbf{T} \cdot \mathbf{n} = \hat{\mathbf{t}} \quad \text{on} \quad \Gamma_u^N \tag{3.29}$$

and for the order parameter

$$\mathbf{S} \cdot \mathbf{n} = \hat{\mathrm{s}} \quad \text{on} \quad \Gamma_\xi^N \tag{3.30}$$

with $\mathbf{n}$ as an outward pointing normal to the boundary Γ.

Following conditions have to be fulfilled on the boundaries

$$\Gamma_u^D \cup \Gamma_u^N = \Gamma \quad \wedge \quad \Gamma_u^D \cap \Gamma_u^N = \emptyset \,, \tag{3.31}$$

$$\Gamma_\xi^D \cup \Gamma_\xi^N = \Gamma \quad \wedge \quad \Gamma_\xi^D \cap \Gamma_\xi^N = \emptyset \,. \tag{3.32}$$

The balance equations

$$\operatorname{div} \mathbf{T} = \mathbf{0} \,, \tag{3.33}$$

$$\operatorname{div} \mathbf{S} + \hat{\kappa} = 0 \,, \tag{3.34}$$

together with the constitutive relationships

$$\mathbf{T} = 2\mu(\xi)\boldsymbol{\varepsilon} + \lambda(\operatorname{tr}\boldsymbol{\varepsilon})\,\mathbf{I}\,, \tag{3.35}$$

$$\mu(\xi) = (1-\xi)\,\mu_1 + \xi\,\mu_2\,, \tag{3.36}$$

$$\mathbf{S} = \operatorname{grad}\xi\,, \tag{3.37}$$

$$\hat{\kappa} = -\alpha\,\xi\,, \tag{3.38}$$

and with the kinematic relationship

$$\boldsymbol{\varepsilon} = \frac{1}{2}(\operatorname{grad}\mathbf{u} + \operatorname{grad}^T\mathbf{u})\,, \tag{3.39}$$

govern the strong form of the order parameter boundary value problem in the quasi-static case. The equation (3.35) describes the relationship between deformation and stress as a function of the order parameter field ξ.

3.4.2 Weak Formulation

In order to solve the boundary value problem formulated in the previous section using the finite element method the weak formulation of the problem is required.

The weak form of the order parameter boundary value problem is obtained by multiplication of the translational momentum (2.58) and order parameter field equation (2.59) with the test functions $\boldsymbol{v} \in \{\delta\mathbf{u}, \delta\xi\}$, followed by integration over the domain Ω with the boundary Γ

$$\int_\Omega \delta\mathbf{u}\cdot\operatorname{div}\mathbf{T}\,\mathrm{d}\Omega = \mathbf{0}\,, \qquad \forall\,\delta\mathbf{u}\in\tilde{\mathcal{U}}\,, \tag{3.40}$$

$$\int_\Omega \delta\xi\cdot\left[\operatorname{div}\mathbf{S} + \hat{\kappa}\right]\mathrm{d}\Omega = 0\,, \qquad \forall\,\delta\xi\in\tilde{\mathcal{P}}\,, \tag{3.41}$$

$$\tilde{\mathcal{U}} := \left\{ \delta\mathbf{u} \in \mathcal{H}^1(\Omega), \quad \delta\mathbf{u}|_{\Gamma_u^D} = \mathbf{0} \right\} , \tag{3.42}$$

$$\tilde{\mathcal{P}} := \left\{ \delta\xi \in \mathcal{H}^1(\Omega), \quad \delta\xi|_{\Gamma_\xi^D} = \mathbf{0} \right\} . \tag{3.43}$$

Applying integration by parts and using the divergence theorem we obtain

$$\int_\Omega \operatorname{grad} \delta\mathbf{u} \,:\, \mathbf{T} \, \mathrm{d}\Omega = \int_{\Gamma_u^N} \delta\mathbf{u} \cdot \hat{\mathbf{t}} \, \mathrm{d}\Gamma \,, \tag{3.44}$$

$$\int_\Omega \left[\operatorname{grad} \delta\xi \cdot \mathbf{S} + \delta\xi \, \hat{\kappa} \right] \mathrm{d}\Omega = \int_{\Gamma_\xi^N} \delta\xi \, \hat{\mathrm{s}} \, \mathrm{d}\Gamma \,. \tag{3.45}$$

The solution $\boldsymbol{u} \in \{\mathbf{u}, \xi\}$ for the translational and order parameter degrees of freedom lies in the function space $\mathcal{U} \times \mathcal{P}$ with

$$\mathcal{U} := \left\{ \mathbf{u} \in \mathcal{H}^1(\Omega), \quad \mathbf{u}|_{\Gamma_u^D} = \hat{\mathbf{u}} \right\} , \tag{3.46}$$

$$\mathcal{P} := \left\{ \xi \in \mathcal{H}^1(\Omega), \quad \xi|_{\Gamma_\xi^D} = \hat{\xi} \right\} . \tag{3.47}$$

The variational formulation of the order parameter problem reads as follows: Find $\boldsymbol{u} \in \mathcal{U} \times \mathcal{P}$ such that

$$a(\boldsymbol{u}, \boldsymbol{v}) = l(\boldsymbol{v}) \,, \quad \forall \; \boldsymbol{v} \in \tilde{\mathcal{U}} \times \tilde{\mathcal{P}} \,. \tag{3.48}$$

In the current problem we have

$$a(\boldsymbol{u}, \boldsymbol{v}) := \int_\Omega \left[\operatorname{grad} \delta\mathbf{u} \,:\, \mathbf{T} + \operatorname{grad} \delta\xi \cdot \mathbf{S} + \delta\xi \, \hat{\kappa} \right] \mathrm{d}\Omega \,, \tag{3.49}$$

$$l(\boldsymbol{v}) := \int_{\Gamma_u^N} \delta\mathbf{u} \cdot \hat{\mathbf{t}} \, \mathrm{d}\Gamma + \int_{\Gamma_\xi^N} \delta\xi \, \hat{\mathrm{s}} \, \mathrm{d}\Gamma \,. \tag{3.50}$$

The approximated solution $\boldsymbol{u}_h$ of the order parameter model is formulated by transforming the continuous variational problem (3.48) into a discrete variational problem with test functions and shape functions lying in the finite-

dimensional function spaces based on the geometric triangulation $\mathcal{T}$ of the domain Ω

$$\boldsymbol{v}_h \in \tilde{\mathcal{U}}_h \times \tilde{\mathcal{P}}_h \subset \tilde{\mathcal{U}} \times \tilde{\mathcal{P}}\,, \quad \boldsymbol{v}_h \in \{\delta\mathbf{u}_h, \delta\xi_h\}\,, \tag{3.51}$$

$$\boldsymbol{u}_h \in \mathcal{U}_h \times \mathcal{P}_h \subset \mathcal{U} \times \mathcal{P}\,, \quad \boldsymbol{u}_h \in \{\mathbf{u}_h, \xi_h\}\,. \tag{3.52}$$

The discrete variational problem is stated as:
Find $\boldsymbol{u}_h$ such that

$$a(\boldsymbol{u}_h, \boldsymbol{v}_h) = l(\boldsymbol{v}_h)\,. \tag{3.53}$$

The next step is the formulation of the approximations $\mathbf{u}_h$ and ξ_h with shape functions $\mathbf{N}^i$ and P^i and corresponding unknown expansion coefficients $\mathbf{u}^i$ and ξ^i

$$\mathbf{u}_h = \sum_i \mathbf{N}^i(\mathbf{x})\,\mathbf{u}^i\,, \tag{3.54}$$

$$\xi_h = \sum_i P^i(\mathbf{x})\,\xi^i\,. \tag{3.55}$$

The test functions $\boldsymbol{v}_h$ are approximated with the same set of functions as used for the solution approximation $\boldsymbol{u}_h$

$$\boldsymbol{v}_h = \sum_i \mathbf{N}^i(\mathbf{x})\,. \tag{3.56}$$

3.4.3 Numerical Examples

In the following examples the macroscopic behavior of the micromechanical reference specimens is modeled by the order parameter approach. Furthermore the influence of the model parameters is demonstrated.

A set of simple shear and tensile test experiments is carried out using geometrically similar specimens. The corresponding boundary conditions and specimen geometries can be found in figure (3.17).

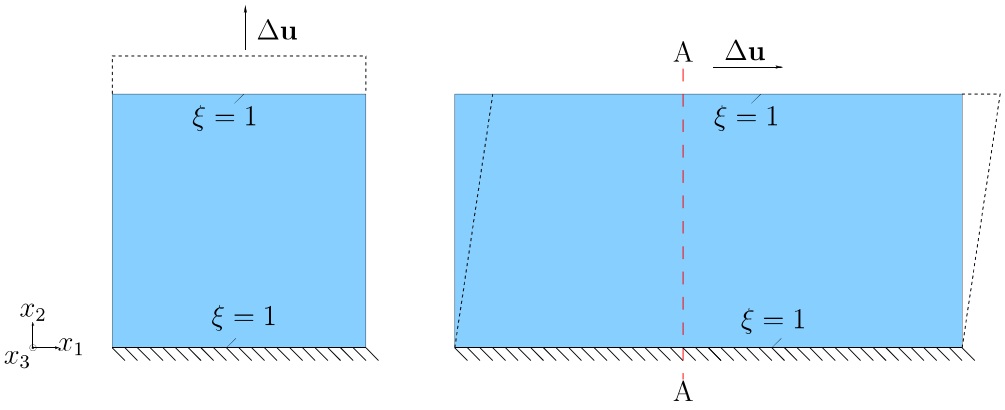

Figure 3.17: Order parameter model. Boundary conditions of tensile test (left) and simple shear test (right).

The results of virtual tensile test experiments are shown in figure (3.18). With the appropriate boundary conditions, the weakening effect is observed for results computed using the order parameter approach.

The additional parameter α controls the distribution of the order parameter variable ξ. In figure (3.19), the field variable ξ is plotted over the height of specimen. For higher values of the parameter α the boundary layer effect dominates the distribution of the order parameter.

The stiffness $\mu(\xi)$ is defined as the function of the variable ξ, which depends on the parameter α. Thus, the latter also controls the distribution of the local stiffness of the specimen bulk. While μ_1 represents the local stiffness in the

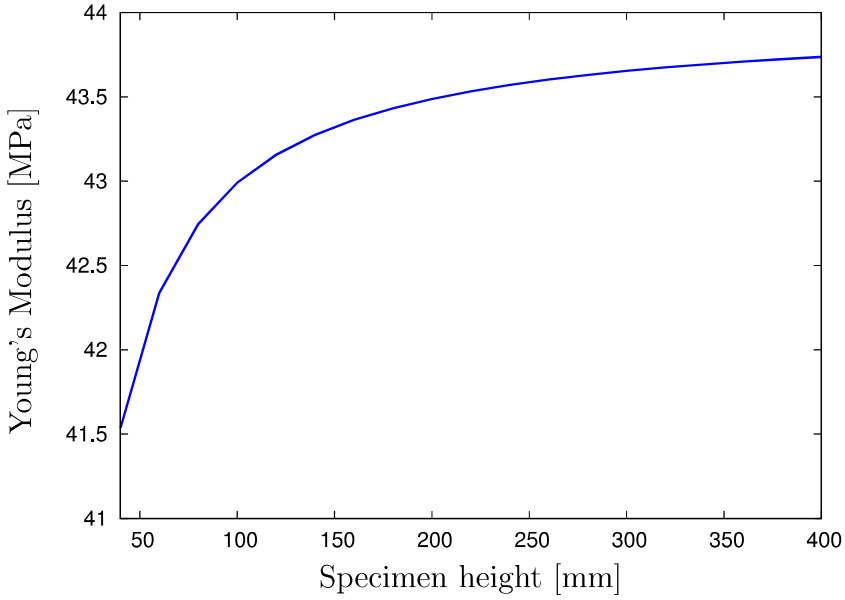

Figure 3.18: Order parameter approach. Size effect in tensile loading.

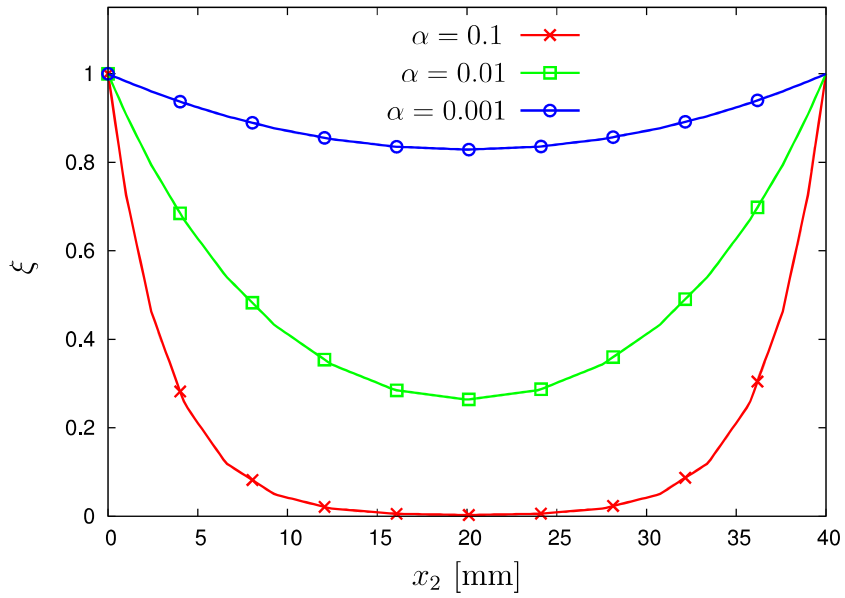

Figure 3.19: Parameter study for model parameter α.

bulk of the specimen which is unaffected by the boundary, μ_2 stands for the stiffness close to the specimen boundary. Using the variation $\Delta\mu = (\mu_2 - \mu_1)$ the material stiffness on the boundaries can be modified.

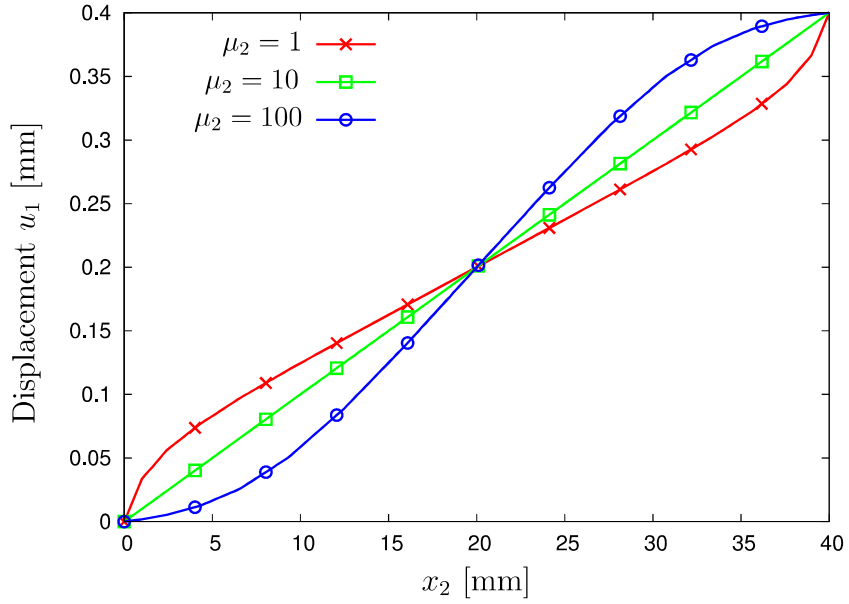

Figure 3.20: Parameter study for model parameter μ_2.

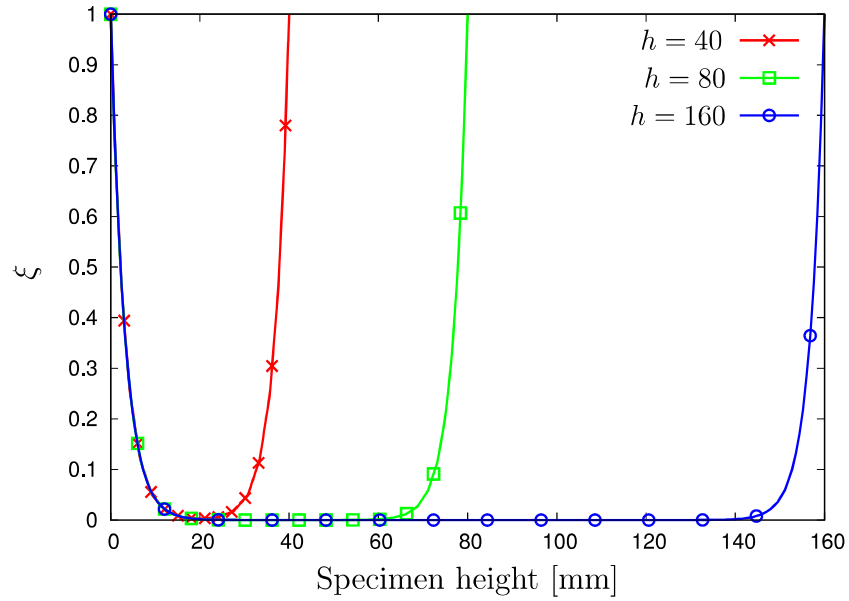

Figure 3.21: Distribution of order parameter ξ for specimens of different size.

The effect of the parameter μ_2 on the displacement field $\mathbf{u}$ in x_1-direction is shown in figure (3.20). The effective stiffness values on the boundaries are

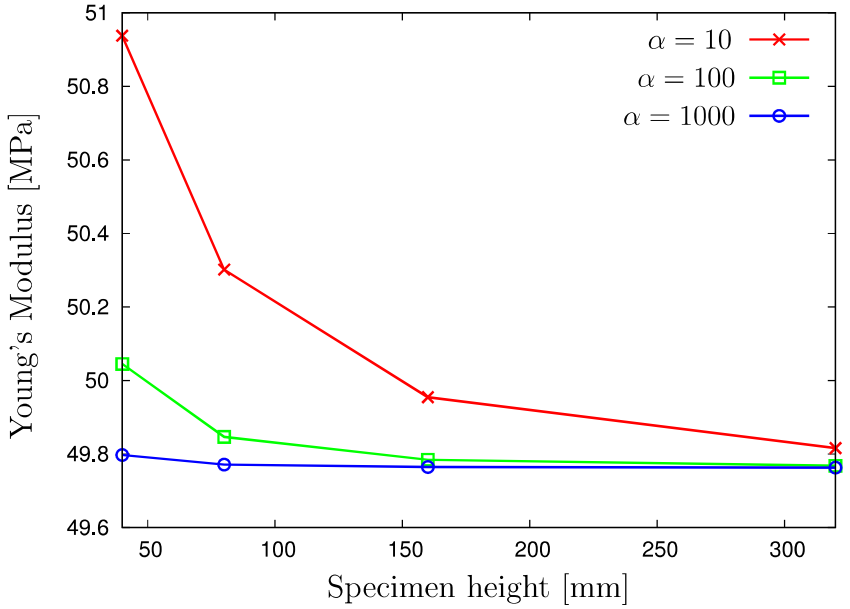

Figure 3.22: Order parameter approach. Size effect in shear loading.

rising directly proportional to the value of μ_2.

Figure (3.21) shows the distribution of the field ξ over the specimen height for specimens of different size. It reveals a constant value of the boundary layer thickness in all of the considered specimens.

The results of the variation of the model parameter α are displayed in figure (3.22). The values of the effective Young's modulus show size-dependent behavior under shear loading conditions. Thereby, the magnitude of the size dependency is controlled by the parameter α. Smaller values of this model parameter are reflected in significantly present size effects whereas large values of α lead to barely observable size effects.

The simulations of standard experiments such as simple shear and tensile test using the order parameter model with the appropriate set of model parameters prove the capability of the order parameter model to describe size effects.

3.5 Identification of Model Parameters

The problem of identification of model parameters is a so-called *inverse problem*. This kind of problem setting consists of deducing the values of the parameters characterizing the system using results obtained from the system investigation. The solution of inverse problem turns out to be a non-trivial task for multiple reasons. The main problems are the size of the parameter space needed to be examined and the parameter uniqueness.

The problem of parameter identification considered in this work can be set as an optimization problem written as

$$\mathcal{Q} = \min_{\boldsymbol{\omega}}[f(\boldsymbol{\omega})]\,, \tag{3.57}$$

where $f(\boldsymbol{\omega})$ is the objective function to be minimized and $\boldsymbol{\omega}$ the vector containing the function parameters. In general, the objective function is chosen as the error between a data set obtained in experiments and the model response for a given set of parameters.

The solution of an optimization problem can be achieved using two basic classes of optimization methods: *gradient-based* and *stochastic* methods. The gradient-based methods are employing the gradient of the function at the current point in the parameter space to define the search direction of the minimum. One of the drawbacks of the gradient-based methods is the susceptibility of running into one of the local minima before finding the global one. The other disadvantage of these methods is the problem of stability. In the case of significant sensitivity of the solution with respect to model parameters (cf. [33]) the arising gradient may become extremely high.

The stochastic optimization methods include an element of randomness in the optimization process. One of the advantages of the stochastic algorithms is the possibility to replace the analytic solution of the investigated problem with a numerical approximation. Furthermore, the stochastic algorithms are

suitable for problems with nonlinear and discontinuous objective functions. Another advantage of the stochastic optimization algorithm is its capability of solving global optimization problems.

A large class of stochastic optimization methods is represented by the *genetic algorithms*, which solve an optimization problem using the principles of biological evolution such as mutation, selection, and recombination (cf. [11, 95, 110]). The goal of the algorithm is to minimize the so-called *fitness function* also known as the objective function in the context of regular optimization algorithms. The algorithm starts with an initial population consisting of a random set of solutions. In each iteration the population of solutions is evaluated with regard to the fitness of each individual. Based on computed scores the parents of the individuals of the next generation are selected. Following the principle of natural selection only the parents with the best scores are selected for the replication. The children are created by performing random modifications to the single parent or by combining the entities of a parents pair. Over multiple generations the initial population undergoes the process of evolutionary development and delivers a population containing individuals with the optimal fitness values.

Another example of a stochastic optimization algorithm is the *particle swarm optimization* (cf. [37, 103, 111]). Here, similar to the genetic algorithms, a random population of solutions is considered as particles, which are moving around in the search space. The movement of the population is controlled by the best found positions of single particles.

With the mentioned advantages the application of the genetic algorithm appears to be a reasonable choice to determine the macroscopic model parameters of the micropolar and order parameter approaches.

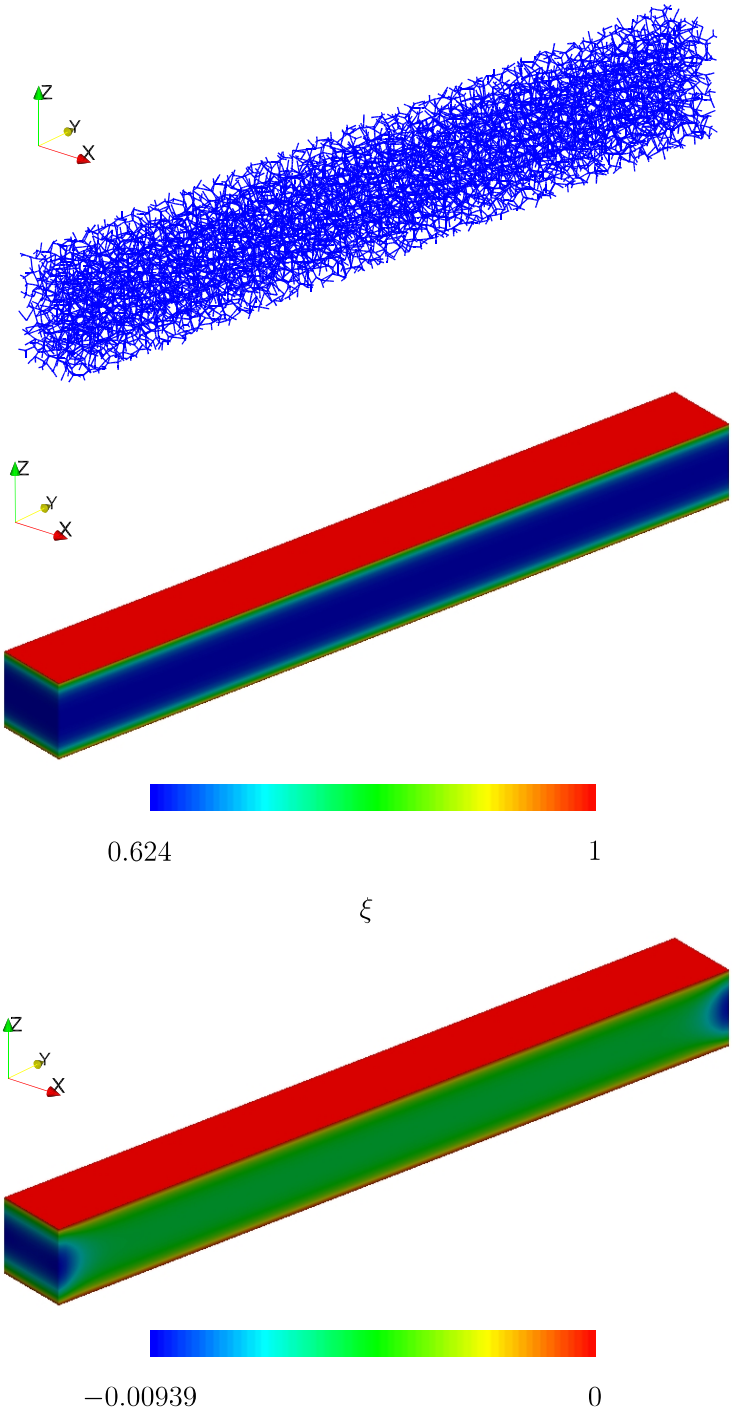

Figure 3.23: Models reproducing the size effect: micromechanical (top), order parameter (middle), and micropolar (bottom).

3.5.1 Micropolar Model Parameters

The vector of model parameters to be determined using the optimization routine for the micropolar problem reads

$$\omega_\varphi = (\lambda, \mu, \mu_c, l_c)\,, \tag{3.58}$$

with λ and μ as the Lamé parameters and μ_c and l_c as the additional micropolar parameters.

Figure (3.23) shows an example of the macroscopic micropolar specimen used to determine the micropolar model parameters. The fitness function used for the parameter identification compares the average shear stress τ obtained from the micromechanical and macroscopic computations performed on a set of the geometrically similar specimens and takes the following form (cf. [21])

$$\mathbf{f}(\omega_\varphi) = \sum_{i=1}^{n} \left(\frac{\tau_i^{macro} - \tau_i^{micro}}{\tau_i^{micro}} \right)^2 , \tag{3.59}$$

with n as the number of different size specimens used.

The following strategy is applied splitting the problem of parameter identification into multiple sub-problems:

1. The shear modulus μ is determined in a single shear test on a sample with large size, where the effect governed by the boundary layer is negligible compared to the macroscopic stiffness.
2. The Lamé parameter λ is determined in a single uniform compression test performed on a large specimen.
3. The additional micropolar parameters l_c and μ_c are identified using the genetic algorithm. For this purpose the simple shear experiment is carried out on specimens with different sizes in each iteration of the genetic algorithm.

All specimens are scaled in size with the constant height-to-length ratio. For all specimens the same effective shear angle $\gamma = \frac{\bar{u}_i}{h_i} = 0.01$ (with h_i as specimen height and $\bar{u}_i$ as displacement) is applied.

The micropolar parameters acquired as the result of the parameter identification procedure are listed in table (3.3). The effective stiffness values computed with the identified set of model parameters are compared with the stiffness values from the micromechanical reference model in figure (3.24).

λ [MPa]	μ [MPa]	μ_c [MPa]	l_c [mm]
28.71	16.53	12.257	4.323

Table 3.3: Identified parameters of micropolar model.

In the presented example the determined model parameters of the macroscopic micropolar model predict the size-dependent mechanical behavior in a simple shear test with the maximum relative error of 1.05% (figure 3.25).

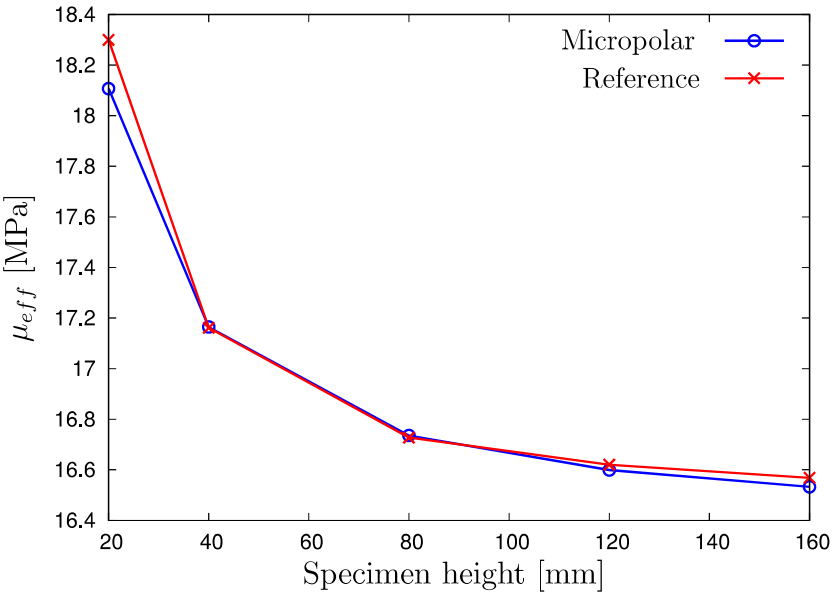

Figure 3.24: Micropolar model. Simple shear test predicted with identified model parameters.

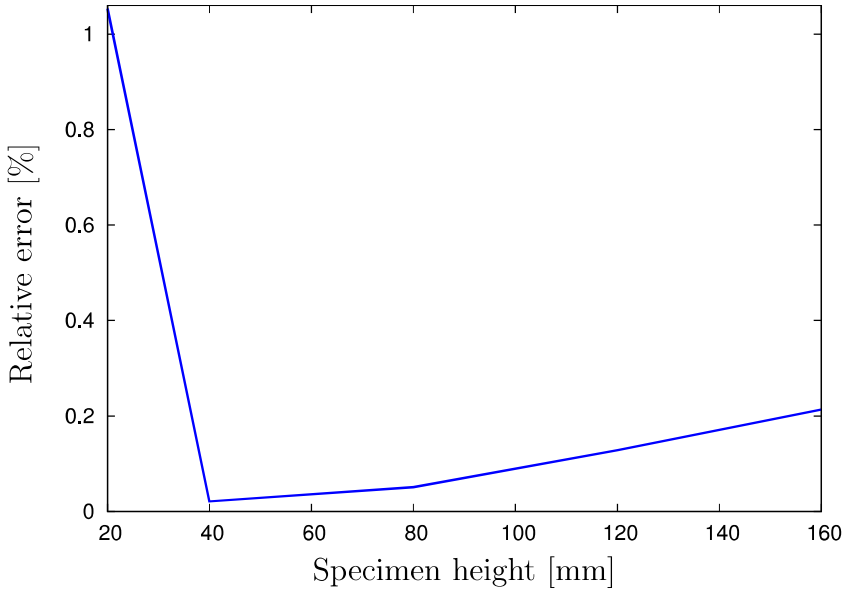

Figure 3.25: Size effect in shear test. Relative error between micropolar and reference models.

The determined value of the internal length parameter ($l_c = 4.323$ mm) is of the same magnitude as the average strut length of the microstructure (4.536 mm). Therefore, the internal length parameter l_c can be linked to the microstructure, providing the average strut length of the cells in the microstructure as a reasonable initial value for the parameter identification procedure.

3.5.2 Order Parameter Constants

The size of the vector of model parameters for the order parameter approach is identical with the vector size in the micropolar case. It contains, however, a different parameter set

$$\omega_\xi = (\lambda, \mu_1, \mu_2, \alpha)\,, \tag{3.60}$$

with λ as Lamé parameter, μ_1 and μ_2 as stiffness parameters and α as the parameter controlling the boundary layer thickness.

The fitness function used here is identical to the function in the micropolar case, hence, minimizing the difference in the mechanical response computed using geometrically similar specimens of micromechanical and macroscopic order parameter models

$$\mathbf{f}(\omega_\xi) = \sum_{i=1}^{n} \left(\frac{\tau_i^{macro} - \tau_i^{micro}}{\tau_i^{micro}} \right)^2 \tag{3.61}$$

with n as the number of different size specimens used.

The identification of parameters is divided into following steps:

1. The initial value of the shear stiffness μ_1 is determined in a single shear test performed on a large specimen.

   The reasonable initial values are obtained by interpretation of the parameter μ_1 as the effective stiffness of larger specimens, where the size effect is barely observable.

2. The Lamé parameter λ is determined in the compression test performed on a single specimen of a large size.

3. The remaining parameters μ_2 and α are identified by means of the genetic algorithm. For this purpose the shear tests on geometrically

similar specimens with different sizes are carried out in every iteration of the genetic algorithm.

The initial value of the parameter μ_2 can be approximated by the evaluation of the effective stiffness values obtained from a test on smaller size specimens, where the size effect has a strong influence.

The constants of the order parameter model determined using the parameter identification routine are listed in table (3.4). The effective stiffness values

λ [MPa]	μ_1 [MPa]	μ_2 [MPa]	α [MPa]
28.71	16.455	31.061	0.34891

Table 3.4: Identified parameters of order parameter model.

computed with the identified parameters are compared with the values from the micromechanical model (figure 3.26). With the identified set of model parameters the order parameter approach predicts the size effect in simple shear test with the maximum relative error of 0.39% , which is comparable to

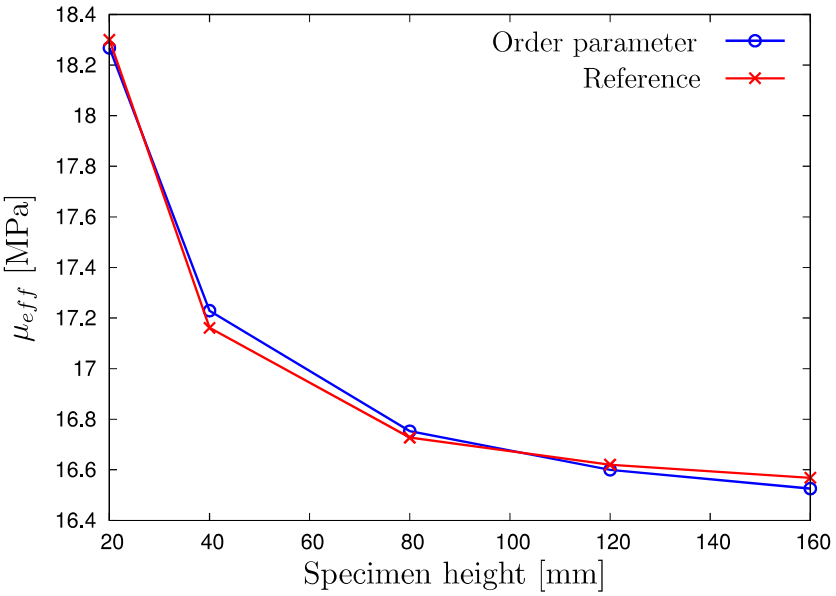

Figure 3.26: Order parameter model. Simple shear test predicted using identified model parameters.

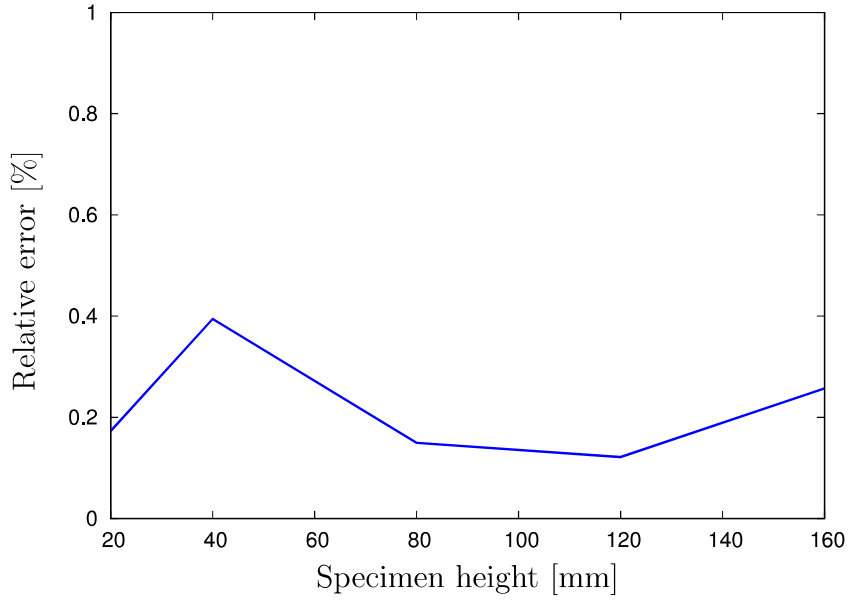

Figure 3.27: Size effect in shear test. Relative error between the order parameter and the reference models.

the precision achieved using the micropolar model. Figure (3.27) shows the relative error between the order parameter simulation and micromechanical model as the function of the specimen's size.

Compared to the size effect observed in tensile tests performed on micromechanical models (figure 3.10), the order parameter constants identified in simple shear tests (table 3.4) provide only a qualitative prediction of the size effect in tensile loading (figure 3.18).

4

Application to Damage Modeling

This chapter deals with the application of the order parameter approach in the context of damage mechanics. The order parameter acts here as a field variable associated with the microstructural property of an open-cell foam. Furthermore, the conceptual background of the continuum damage mechanics is presented.

The numerical properties of the presented damage formulation are demonstrated in standard benchmark tests. In addition, the influence of the model parameters on the damage evolution is discussed. An extended formulation based on the additional microstructural data such as strut orientation is presented.

Another crucial aspect discussed in the present chapter is the comparison of the results obtained with the numerical model and in a real world experiment.

4.1 Continuum Damage Mechanics

The subject of the continuum damage mechanics is dedicated to the description of the processes related to structural changes of the material resulting from nucleation of new and growth of the existing defects. The final stage of the damage process results in a total breakup of all bounds and as a consequence in alteration of the effective material properties.

The deterioration process is modeled using an internal damage state with a scalar or tensor valued variable related to it. The description of change of the damage state requires the evolution equation of the damage variable. The domain of analysis of continuum damage mechanics can be classified by scale ranging between the micro-level and meso-level.

4.1.1 A Short Historical Overview

The development of the field of continuum damage mechanics begins in 1958 with the pioneering work of L. M. Kachanov [66] in which a first concept of a field variable called continuity associated with the loss of strength of metals undergoing creep was introduced. In 1968 Rabotnov [105] proposed the concept of effective stress, representing the effect of stress increased due to the reduction of undamaged area.

Lemaitre [79] generalized the concept of the effective stress stating that the constitutive equation of a damaged material can be derived from the constitutive relation of an undamaged material by substitution of the stress tensor with the corresponding effective stress tensor. This generalization is called strain equivalence principle and describes the coupling between damage and strain.

In the middle of 1970s, first applications of damage mechanics to creep of

structures (cf. [78]) and creep-fatigue interaction (cf. [82]) were made. In the work of Gurson [54] a rupture model with approximate yield criteria and flow rules for porous ductile materials were proposed. This work also exhibits the role of the hydrostatic stress in plastic yield and void growth processes.

Addressing the irreversible nature of the damage process the treatment of the damage variable within the framework of thermodynamics was presented by Lemaitre and Chaboche [83], Krajcinovic [71], and Kachanov [65].

Since the late 1980s, an increasing number of damage models corresponding to different failure mechanisms has been proposed. These include the formulation of damage concepts for composites (cf. [117]), low cycle fatigue (cf. [35]), and treatment of the damage localization problem (cf. [12]).

A so-called *non-local* damage approach was proposed in [8, 9], with the evolution equation of the damage at a point governed by the local state variable and neighboring fields. The non-local damage theory provides an efficient method to deal with the issue of strain localization. The description of the isotropic damage was extended to the general state of three-dimensional anisotropic damage in the work of Murakami [97].

A number of formulations addressing the multiscale nature of the damage mechanisms have been introduced since the 1990s. To describe the damage in quasi-brittle materials where no dissipation occurs before crack initiation a two-scale damage model was presented by Lemaitre [81]. The two-scale damage approach was also applied to describe the damage effects such as nonlinear accumulation of damage and initial strain hardening related to high cycle fatigue processes (cf. [86]). Later on, the gradient-enhanced damage model for quasi-brittle materials was proposed by Peerlings et al. [102].

The framework of micropolar continuum theory was used by Steinmann [115] to formulate the elastoplastic damage concept for ductile materials. In the work of Forest [48] the micromorphic approach is applied to damage thermomechanics together with an overview of the available damage gradient

models.

A number of works dealing with the problems of damage and fracture of composite materials has come out since the end of 1990s (cf. [49, 77]). The complex failure mechanisms of composite materials led to increased development and application of multiscale approaches (cf. [47, 75, 76]).

A comprehensive review of the available damage mechanics models related to various material behavior and degradation phenomena can be found in [65, 72, 84, 98, 124].

4.1.2 Damage Variable

In the scope of the continuum damage mechanics the damage state of the material is represented in terms of the damage variable. This variable is used to characterize the mechanical behavior of the damaged material and the evolution of the damage.

The damage process is reflected in changes of many different material properties (i. e. alteration of effective stiffness, hardness, density, electrical resistance, yield stress etc.) taking effect on a multitude of scales. The changes in material which are observable and measurable in experiments can be used to define a damage variable.

The geometrical quantification is a straightforward possibility to describe the damage state. This concept was proposed by Kachanov to predict the brittle creep rupture time of metals under tension (cf. [66]).

Consider a damaged body displayed in figure (4.1) with an isolated representative volume element (RVE). The damage variable is defined by the surface density of the damaged area $\mathrm{d}A_D$ on a plane cutting through the RVE with

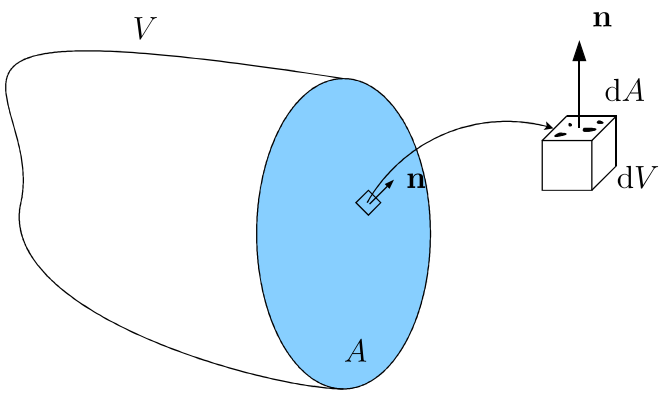

Figure 4.1: Geometrical quantification of damage.

a cross section $\mathrm{d}A$ with the normal vector $\mathbf{n}$

$$\omega(\mathbf{n}) = \frac{\mathrm{d}A_D}{\mathrm{d}A}\,, \quad 0 \leq \omega(\mathbf{n}) \leq 1\,. \tag{4.1}$$

The value $\omega = 0$ corresponds to the undamaged material and the value $\omega = 1$ implies the totally damaged material with macroscopic crack initiation taking place. However, the values of damage determined in experiments can be lower, resulting in total failure of the material with a critical value $\omega_c < 1$.

In the equation (4.1), the respective intrinsic variable $\boldsymbol{\omega}$ is a second order tensor (cf. [99]) providing the definition of the damage in the orthotropic case. This tensor maps the surface $\mathrm{d}A$ with the corresponding normal vector $\mathbf{n}$ to the surface $\mathrm{d}\tilde{A} = \mathrm{d}A - \mathrm{d}A_D$ with the normal vector $\tilde{\mathbf{n}}$ indicating the change of surface orientation due to the anisotropy of damage

$$(\mathbf{I} - \boldsymbol{\omega}) \cdot \mathbf{n}\,\mathrm{d}A = \tilde{\mathbf{n}}\,\mathrm{d}\tilde{A}\,. \tag{4.2}$$

Assuming that the damage is equally distributed in all directions, the damage variable becomes independent from the normal vector $\mathbf{n}$. Thus, the definition of the damage variable for the case of isotropy can be written in the following form

$$\omega = \frac{\mathrm{d}A_D}{\mathrm{d}A}\,, \tag{4.3}$$

with the damage tensor from the equation (4.1) reduced to a scalar.

In particular cases it may be advantageous to utilize the so-called continuity function as proposed by Kachanov (cf .[65, 66])

$$\psi = 1 - \omega \,. \tag{4.4}$$

Apart from the area-based variable definitions a number of concepts of the damage variable exist. The definition of the damage variable can be extended to a fourth order tensor $\overset{4}{\mathbf{D}}$

$$\overset{4}{\mathbf{D}} = \overset{4}{\mathbf{I}} - \overset{4}{\mathbf{C}}\,(\overset{4}{\mathbf{D}}) : (\overset{4}{\mathbf{C}}_0)^{-1} \,, \tag{4.5}$$

acting as an operator changing the elasticity tensor

$$\overset{4}{\mathbf{C}}\,(\overset{4}{\mathbf{D}}) = (\overset{4}{\mathbf{I}} - \overset{4}{\mathbf{D}}) : \overset{4}{\mathbf{C}}_0 \,, \tag{4.6}$$

with $\overset{4}{\mathbf{C}}_0$ as the elasticity tensor of an undamaged material (cf. [20]). As an example for another alternative definition, the void volume fraction can be adopted to describe the damage state in the material (cf. [54])

$$\omega = \frac{\mathrm{d}V_D}{\mathrm{d}V} \,, \tag{4.7}$$

where $\mathrm{d}V$ is the volume of RVE and $\mathrm{d}V_D$ is the volume of voids. Depending on the considered scale of the damage phenomenon further damage variable definitions incorporating the microstructural features such as geometrical configuration of micro-voids (cf. [99]) or directional distribution of defect density (cf. [68]) can be found in the literature.

4.1.3 Effective Stress Concept

The mechanical behavior of damaged material is described using the concept of effective stress, introducing a stress vector $\tilde{\mathbf{t}}$ acting on the surface $\mathrm{d}\tilde{A}$

effectively resisting the load (cf. [85])

$$\tilde{\mathbf{t}} = \mathbf{t}\,\frac{\mathrm{d}A}{\mathrm{d}\tilde{A}} = \frac{\mathbf{t}}{1-\omega}\,. \tag{4.8}$$

The effective stress tensor in the general case of damage is given by

$$\tilde{\mathbf{T}} = (\mathbf{I} - \boldsymbol{\omega})^{-1}\,\mathbf{T}\,. \tag{4.9}$$

The lack of symmetry of the effective stress in the equation above makes it in general rather unsuitable for the formulation of constitutive equations. This issue can be solved by various symmetrization techniques as summarized in [98].

In the case of isotropic damage the effective stress tensor can be simplified to

$$\tilde{\mathbf{T}} = \frac{\mathbf{T}}{1-\omega}\,. \tag{4.10}$$

4.1.4 Strain Equivalence Hypothesis

With the assumption that the deformation is only affected by the effective stress, the strain equivalence hypothesis proposed by Lemaitre [80] states that strains in the damaged material are equivalent to the strains in the undamaged material with the stress tensor $\mathbf{T}$ replaced by the effective stress tensor $\tilde{\mathbf{T}}$

$$\boldsymbol{\varepsilon} = \boldsymbol{\varepsilon}\,(\mathbf{T},\,\omega) = \boldsymbol{\varepsilon}\,(\tilde{\mathbf{T}})\,. \tag{4.11}$$

As a consequence, the constitutive equations of the undamaged material with the effective stress substitution can be employed to describe the material behavior of the damaged material. The hypothesis of strain equivalence is visualized in figure (4.2).

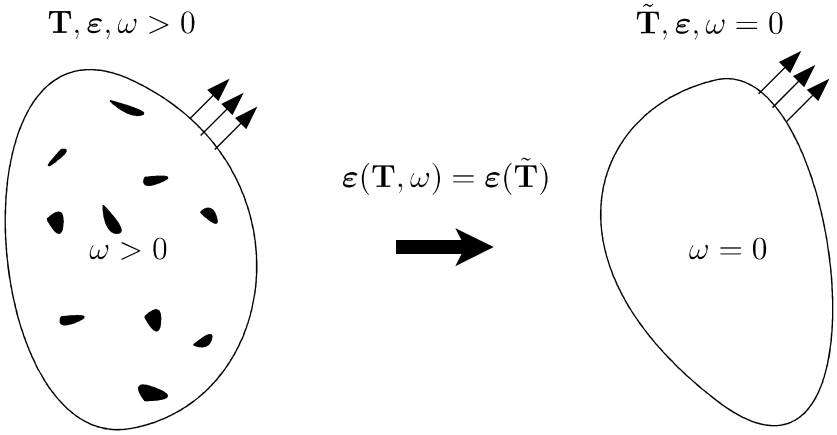

Figure 4.2: Strain equivalence hypothesis.

According to the hypothesis of strain equivalence the values of Young's and shear moduli of the damaged material are decreased by the factor $(1 - \omega)$, therefore, the damage state in the isotropic case in uniaxial tension can be identified by the measurement of the effective Young's modulus $\tilde{E}$

$$\tilde{E} = (1 - \omega) E_0 \,, \tag{4.12}$$

$$\omega = 1 - \frac{\tilde{E}}{E_0} \,, \tag{4.13}$$

with E_0 as the Young's modulus of the virgin material.

4.1.5 Damage Evolution

The process of the damage development is described by the evolution equation in the form

$$\frac{\partial \omega}{\partial \lambda} = f(\mathbf{T}, \omega, \boldsymbol{\alpha}) \,, \tag{4.14}$$

where $\boldsymbol{\alpha}$ is the vector consisting of further model-dependent parameters having effect on damage evolution (e. g. temperature, plastic strain rate, porosity etc.) and $\lambda > 0$ a monotonically increasing parameter (e. g. time, entropy,

etc.) describing the loading of the volume element.

The consequence of the damage evolution is the loss of material stiffness associated with the release of energy. The release rate of elastic strain energy Y is introduced as a conjugate variable associated with the damage and derived from the state potential in the form of Helmholtz free energy Ψ

$$Y = -\rho \frac{\partial \Psi}{\partial \omega} \,. \tag{4.15}$$

For the case of isotropic elastic damage, the Helmholtz free energy is written as a function of the linear strain and the damage variable

$$\rho\, \Psi(\boldsymbol{\varepsilon}, \omega) = (1 - \omega)\, \Psi^e \,, \tag{4.16}$$

with the elastic strain energy density given by

$$\Psi^e = \frac{1}{2} \lambda \left(\boldsymbol{\varepsilon} : \mathbf{I}\right)^2 + \mu\, \boldsymbol{\varepsilon} : \boldsymbol{\varepsilon} \,. \tag{4.17}$$

Combining the equations (4.16) and (4.17) the elastic energy release rate is written as

$$Y = \Psi^e = \frac{1}{2} \lambda \left(\boldsymbol{\varepsilon} : \mathbf{I}\right)^2 + \mu\, \boldsymbol{\varepsilon} : \boldsymbol{\varepsilon} \,. \tag{4.18}$$

The actual damage evolution can be represented using phenomenological, thermodynamical or micromechanical approaches. In the framework of thermodynamics the evolution equation of dissipative damage variables can be derived from the potential of dissipation F (cf. [80, 85])

$$\dot{\omega} = -\frac{\partial F}{\partial Y} \,. \tag{4.19}$$

The choice of the potential function F is not obvious and depends in the first place on the observations and insights gained in experiments. The essential requirement for the potential of dissipation is that it must be a scalar convex function of flux variables or of their dual variables (cf. [85]).

4.2 Damage Modeling of Open-Cell Foams

4.2.1 Topology-based Damage Variable

The mechanical properties of foam materials are mainly defined by the material structure on the microscopic level. The characterization of the cellular material microstructure can be made based on the following properties (cf. [50]):

porosity

mean cell diameter

dispersion of cell size

symmetry

edge-connectivity

Several material properties are affected as a consequence of the damage process. In the present contribution, the topological information such as edge-connectivity obtained from the microstructure is used to define a damage evolution approach for an open-cell foam structure.

For the sake of convenience we consider a two-dimensional open-cell lattice structure shown in figure (4.3). Each cell is connected with the neighboring cells through struts. The number of the neighboring cells depends on the foam morphology. The edge-connectivity Z_e is one of the properties characterizing cellular materials and is defined as the average number of edges linked to a vertex (cf. [50]).

In the structure depicted in figure (4.3) the edge-connectivity values within the bulk material are always higher than the connectivity values on the spec-

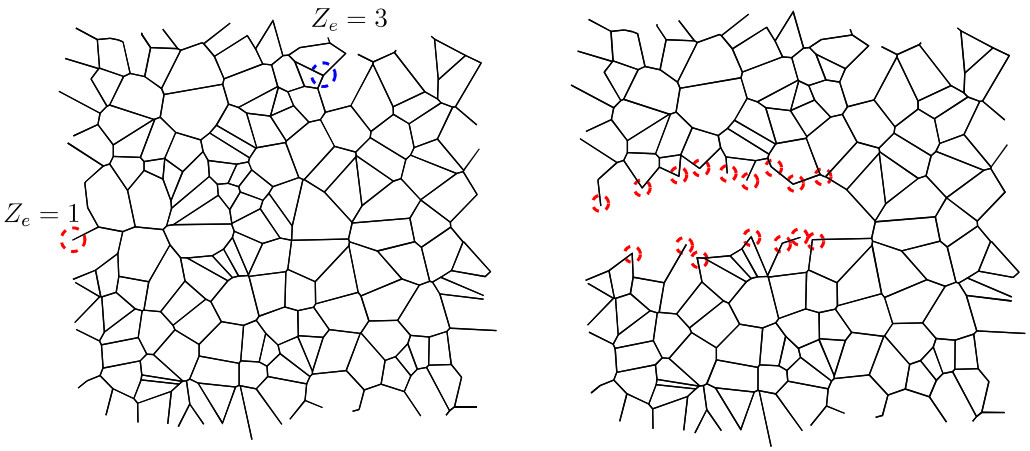

Figure 4.3: Edge-connectivity of foam: virgin (left) and damaged (right) states.

imen boundary (cf. weak boundary layer, section 3.2.2), resulting in magnitudes of edge-connectivities in the following range

$$1 \leq Z_e \leq 4\,. \tag{4.20}$$

Since the mechanical stability of an open-cell foam is directly linked to the number of connections between cells and the edge-connectivity deteriorates with the ongoing damage process (figure 4.3, right), a measure based on the edge-connectivity can be used to represent the damage state of the foam.

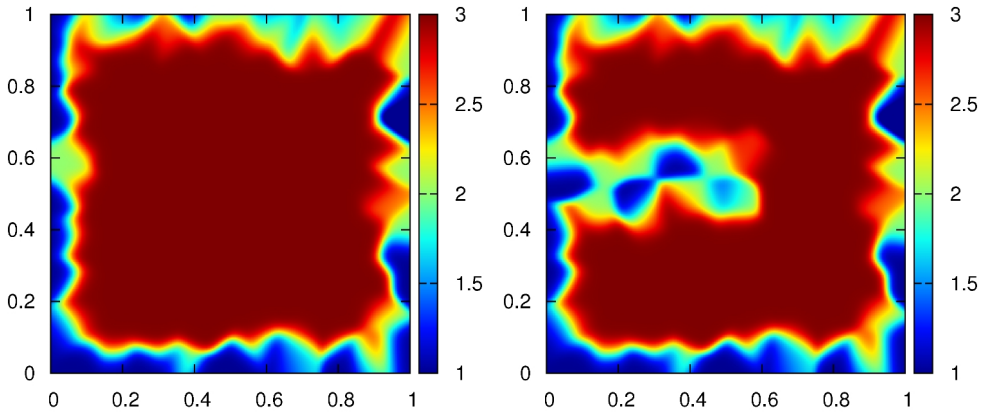

Figure 4.4: Average edge-connectivity distribution: virgin (left) and damaged (right) states.

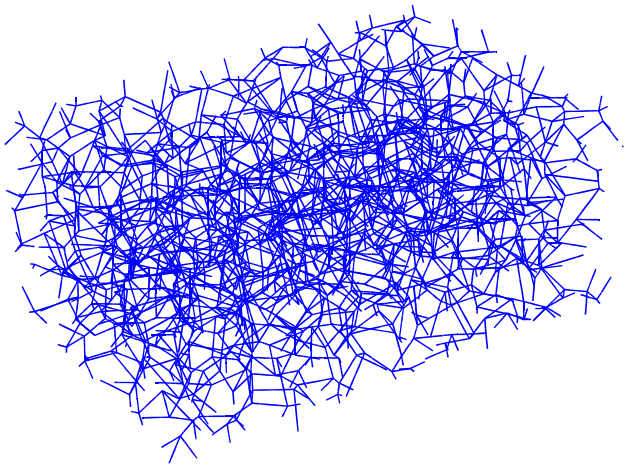

Figure 4.5: Three-dimensional foam specimen.

The edge-connectivity distributions corresponding to specimen in the initial virgin state and in the damaged state is shown in figure (4.4). The edge-connectivity distribution present in the two-dimensional case is also observed in three-dimensional foam specimens (figure 4.5). An example of the distribution of edge-connectivity along the x_1-direction is displayed in figure (4.6). Due to the random spatial distribution of the cell vertexes the raw distribution data is unsuitable for the visualization of the edge-connectivity field. For this purpose, the utilization of the moving average appears to be an appropriate technique (figure 4.7).

The starting point of the order parameter-based damage formulation is the definition of the damage variable. With the continuity function (not to be confused with the free Helmholtz energy introduced in equation (2.60)) defined as

$$\Psi = 1 - \xi \,, \tag{4.21}$$

we formulate the continuity relationship as a function of edge-connectivity Z_e

$$\Psi = \frac{Z_e}{Z_0} \,, \tag{4.22}$$

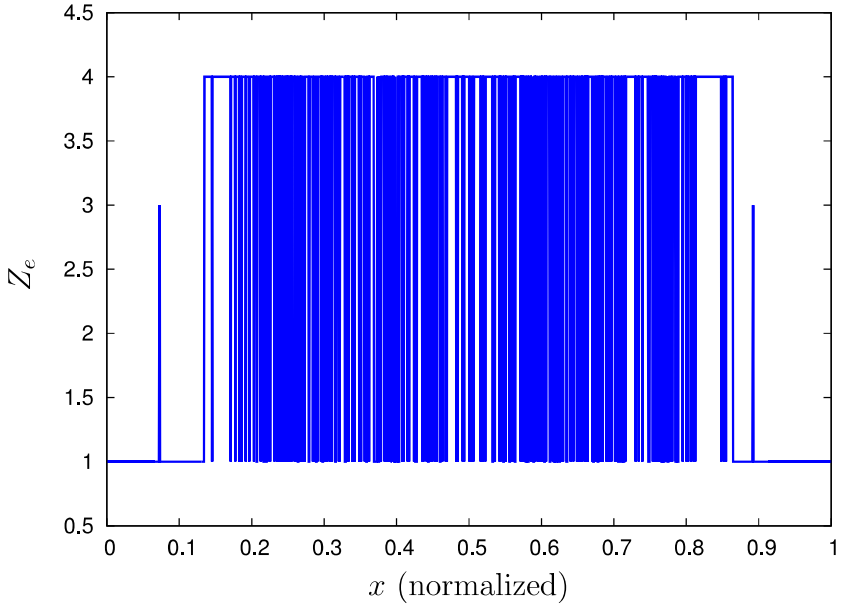

Figure 4.6: Distribution of the edge-connectivity Z_e over specimen length.

with Z_e as the current number of connections to neighboring cells and Z_0 the number of connections in the initial undamaged state.

With the equation (4.21) the topology-based damage variable reads as follows

$$\xi = 1 - \frac{Z_e}{Z_0}, \quad 0 \leq \xi \leq 1\,. \tag{4.23}$$

The damage variable takes the values $\xi = 0$ for the material without damage (i. e. the cell has full number of connections) and $\xi = 1$ for the completely damaged material (i. e. all of the connections to neighboring cells are lost, the cell is cut off from the remaining structure).

Due to the boundary layer in the edge-connectivity distribution the order parameter approach is a natural choice for the description of the damage field. Hereby, the material is considered containing two distinct phases: the phase containing undamaged material and the phase with the material in damaged state. Hence, the damage variable is used to describe the separation of two phases together with the interface development. This approach is similar to the procedure used in phase filed models as proposed in [17].

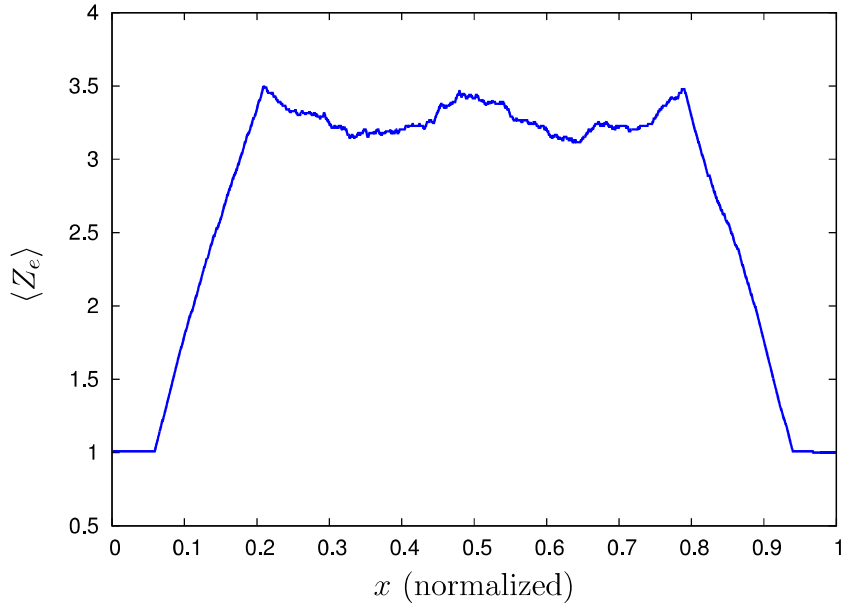

Figure 4.7: Distribution of the average edge-connectivity $\langle Z_e \rangle$ over specimen length.

4.2.2 Damage Formulation

In the following we consider a space-time domain $\Omega \times T$ with a boundary $\Gamma \times T$. The order parameter damage formulation is governed by the translational momentum equation, kinematic and constitutive relations in the isotropic linear elastic case, together with the balance equation of the damage field modeled by the order parameter. The boundary value problem is completed by the set of initial boundary conditions at the time $t = T_0$ prescribed on the material body boundary.

On the boundaries Γ_u^D and Γ_ξ^D the Dirichlet boundary conditions for the kinematic degrees of freedom

$$\mathbf{u} = \hat{\mathbf{u}} \quad \text{on} \quad \Gamma_u^D \times T_0 \,, \tag{4.24}$$

and the degrees of freedom associated with the order parameter damage field

$$\xi = \hat{\xi} \quad \text{on} \quad \Gamma_{\xi}^{D} \times T_0 \,, \tag{4.25}$$

are prescribed.

On the boundaries Γ_u^N and Γ_ξ^N a set of Neumann boundary conditions for the kinematic degrees of freedom

$$\mathbf{T} \cdot \mathbf{n} = \hat{\mathbf{t}} \quad \text{on} \quad \Gamma_{u}^{N} \times T_0 \,, \tag{4.26}$$

and for the order parameter

$$\mathbf{S} \cdot \mathbf{n} = \hat{\mathrm{s}} \quad \text{on} \quad \Gamma_{\xi}^{N} \times T_0 \,, \tag{4.27}$$

with $\mathbf{n}$ as an outward pointing normal to the boundary Γ, are required.

Furthermore, following conditions have to be fulfilled on the boundaries

$$\Gamma_u^D \cup \Gamma_u^N = \Gamma \quad \wedge \quad \Gamma_u^D \cap \Gamma_u^N = \emptyset \,, \tag{4.28}$$

$$\Gamma_\xi^D \cup \Gamma_\xi^N = \Gamma \quad \wedge \quad \Gamma_\xi^D \cap \Gamma_\xi^N = \emptyset \,. \tag{4.29}$$

The set of balance equations with neglected body forces reads as follows

$$\operatorname{div} \mathbf{T} = \mathbf{0} \,, \tag{4.30}$$

$$\operatorname{div} \mathbf{S} + \hat{\kappa} = \frac{\partial \xi}{\partial t} \,. \tag{4.31}$$

The constitutive relationships are derived starting from the Helmholtz free energy chosen as

$$\rho \boldsymbol{\Psi} = \Psi_u(\mathbf{E}, \, \xi) + \Psi_\xi(\xi, \, \operatorname{grad} \xi) \,, \tag{4.32}$$

where $\Psi_u(\mathbf{E}, \, \xi)$ is the elastic part of the Helmholtz free energy depending

linearly on damage ξ

$$\rho\Psi_u(\mathbf{E},\,\xi) = (1-\xi)\tilde{\Psi}_u(\mathbf{E})\,, \tag{4.33}$$

with

$$\rho\tilde{\Psi}_u(\mathbf{E}) = \frac{1}{2}\lambda(\mathbf{E}\,:\,\mathbf{I})^2 + \mu\,\mathbf{E}\,:\,\mathbf{E}\,. \tag{4.34}$$

The order parameter contribution $\Psi_\xi(\xi,\,\mathrm{grad}\,\xi)$ is defined as

$$\rho\Psi_\xi(\xi,\,\mathrm{grad}\,\xi) = \frac{1}{2}\alpha\,\xi^2 + \frac{1}{2}\beta(\mathrm{grad}\,\xi)^2\,. \tag{4.35}$$

With the derivation procedure outlined in section (2.3) following constitutive relationships are obtained

$$\mathbf{T} = \rho\,\mathbf{F}\cdot\frac{\partial\boldsymbol{\Psi}}{\partial\mathbf{E}}\cdot\mathbf{F}^T = (1-\xi)\,\tilde{\mathbf{T}}\,, \tag{4.36}$$

$$\mathbf{S} = \rho\,\frac{\partial\boldsymbol{\Psi}}{\partial\,\mathrm{grad}\,\xi} = \beta\,\mathrm{grad}\,\xi\,, \tag{4.37}$$

$$\hat{\kappa} = -\rho\frac{\partial\boldsymbol{\Psi}}{\partial\xi} = \tilde{\Psi}_u - \alpha\,\xi\,. \tag{4.38}$$

Using the kinematic relation for the geometrically linear case obtained by replacement of the Green strain tensor $\mathbf{E}$ with the linear strain tensor $\boldsymbol{\varepsilon}$

$$\mathbf{E} \approx \boldsymbol{\varepsilon} = \frac{1}{2}(\mathrm{Grad}\,\mathbf{u} + \mathrm{Grad}^T\mathbf{u})\,, \tag{4.39}$$

the effective stress is written in the following form

$$\tilde{\mathbf{T}} = \frac{\mathbf{T}}{1-\xi} = 2\mu\,\boldsymbol{\varepsilon} + \lambda\,(\mathrm{tr}\,\boldsymbol{\varepsilon})\,\mathbf{I}\,. \tag{4.40}$$

Substitution of the relationships (4.37) and (4.38) in the balance equation (4.31) provides the evolution equation of the order parameter formulation of

the damage field

$$\operatorname{div}(\beta \operatorname{grad} \xi) - \alpha\, \xi + \tilde{\Psi}_u = \gamma \frac{\partial \xi}{\partial t} \,. \tag{4.41}$$

Here, the term $\tilde{\Psi}_u$ corresponds to the elastic energy release rate from equation (4.18).

4.2.3 Weak Formulation of the Model Equations

The weak form of the boundary value problem of the order parameter damage approach is obtained by multiplication of the balance equations at a time $t \in T$, $T = [0, I]$ with the test functions and integration over the domain Ω

$$\int_\Omega \delta\mathbf{u} \cdot \operatorname{div} \mathbf{T} \, \mathrm{d}\Omega = \mathbf{0} \,, \qquad \forall\, \delta\mathbf{u} \in \tilde{\mathcal{U}} \,, \tag{4.42}$$

$$\int_\Omega \delta\xi \cdot \left[\operatorname{div} \mathbf{S} + \hat{\kappa} - \frac{\partial \xi}{\partial t}\right] \mathrm{d}\Omega = 0 \,, \qquad \forall\, \delta\xi \in \tilde{\mathcal{P}} \,, \tag{4.43}$$

$$\tilde{\mathcal{U}} := \left\{ \delta\mathbf{u} \in \mathcal{H}^1(\Omega), \quad \delta\mathbf{u}|_{\Gamma_u^D} = \mathbf{0} \right\} \,, \tag{4.44}$$

$$\tilde{\mathcal{P}} := \left\{ \delta\xi \in \mathcal{H}^1(\Omega), \quad \delta\xi|_{\Gamma_\xi^D} = \mathbf{0} \right\} \,. \tag{4.45}$$

We consider test functions $\boldsymbol{v} \in \{\delta\mathbf{u}, \delta\xi\}$ which depend on spatial coordinates only. The time derivative is approximated by the finite difference method.

Performing the integration by parts and using the divergence theorem we obtain

$$\int_\Omega \operatorname{grad} \delta\mathbf{u} \,:\, \mathbf{T} \, \mathrm{d}\Omega = \int_{\Gamma_u^N} \delta\mathbf{u} \cdot \hat{\mathbf{t}} \, \mathrm{d}\Gamma \,, \tag{4.46}$$

$$\int_\Omega \left[\operatorname{grad} \delta\xi \cdot \mathbf{S} + \delta\xi\, \hat{\kappa} - \delta\xi \frac{\partial \xi}{\partial t}\right] \mathrm{d}\Omega = \int_{\Gamma_\xi^N} \delta\xi\, \hat{\mathrm{s}} \, \mathrm{d}\Gamma \,. \tag{4.47}$$

The solution $\boldsymbol{u} \in \{\mathbf{u}, \xi\}$ for the translational and order parameter degrees of freedom lies in the function space $\mathcal{U} \times \mathcal{P}$ with

$$\mathcal{U} := \left\{ \mathbf{u} \in \mathcal{H}^1(\Omega), \quad \mathbf{u}|_{\Gamma_u^D} = \hat{\mathbf{u}} \right\}, \tag{4.48}$$

$$\mathcal{P} := \left\{ \xi \in \mathcal{H}^1(\Omega), \quad \xi|_{\Gamma_\xi^D} = \hat{\xi} \right\}. \tag{4.49}$$

The variational formulation of the order parameter damage model reads as follows:
Find $\boldsymbol{u} \in \mathcal{U} \times \mathcal{P}$ such that

$$\left(\frac{\partial \xi}{\partial t}, \boldsymbol{v} \right) + a(\boldsymbol{u}, \boldsymbol{v}) = l(\boldsymbol{v}), \quad \forall\, \boldsymbol{v} \in \tilde{\mathcal{U}} \times \tilde{\mathcal{P}}, \quad \forall\, t \in T. \tag{4.50}$$

In the current problem we have

$$a(\boldsymbol{u}, \boldsymbol{v}) := \int_\Omega \left[\operatorname{grad} \delta\mathbf{u} \,:\, \mathbf{T} + \operatorname{grad} \delta\xi \cdot \mathbf{S} + \delta\xi\, \hat{\kappa} \right] \mathrm{d}\Omega, \tag{4.51}$$

$$l(\boldsymbol{v}) := \int_{\Gamma_u^N} \delta\mathbf{u} \cdot \hat{\mathbf{t}}\, \mathrm{d}\Gamma + \int_{\Gamma_\xi^N} \delta\xi\, \hat{\mathrm{s}}\, \mathrm{d}\Gamma, \tag{4.52}$$

$$\left(\frac{\partial \xi}{\partial t}, \boldsymbol{v} \right) := \int_\Omega \delta\xi\, \frac{\partial \xi}{\partial t}\, \mathrm{d}\Omega, \tag{4.53}$$

with $(\cdot, \cdot)$ as an inner product of the function space L^2 of square integrable functions.

The numerical solution of the order parameter damage model is obtained by the transformation of the continuous variational problem (4.50) into a discrete variational problem with functions lying in the finite-dimensional function spaces based on the geometric triangulation $\mathcal{T}$ of the domain Ω

$$\boldsymbol{v}_h \in \tilde{\mathcal{U}}_h \times \tilde{\mathcal{P}}_h \subset \tilde{\mathcal{U}} \times \tilde{\mathcal{P}}, \quad \boldsymbol{v}_h \in \{\delta\mathbf{u}_h, \delta\xi_h\}, \tag{4.54}$$

$$\boldsymbol{u}_h \in \mathcal{U}_h \times \mathcal{P}_h \subset \mathcal{U} \times \mathcal{P}, \quad \boldsymbol{u}_h \in \{\mathbf{u}_h, \xi_h\}. \tag{4.55}$$

The semi-discrete variational problem can be stated as:
Find $\boldsymbol{u}_h$ such that

$$\left(\frac{\partial \xi}{\partial t}, \boldsymbol{v}_h\right) + a(\boldsymbol{u}_h, \boldsymbol{v}_h) = l(\boldsymbol{v}_h)\,, \quad \forall\, t \in T\,. \tag{4.56}$$

The next step is the formulation of the approximations $\mathbf{u}_h$ and ξ_h with shape functions $\mathbf{N}^i$ and P^i

$$\mathbf{u}_h = \sum_i \mathbf{N}^i(\mathbf{x})\, \mathbf{u}^i(t)\,, \tag{4.57}$$

$$\xi_h = \sum_i P^i(\mathbf{x})\, \xi^i(t)\,, \tag{4.58}$$

with corresponding unknown expansion coefficients $\mathbf{u}^i$ and ξ^i depending on time t.

The test functions $\boldsymbol{v}_h$ are approximated with the same set of functions as used for the solution approximation $\boldsymbol{u}_h$

$$\boldsymbol{v}_h = \sum_i^m \mathbf{N}^i(\mathbf{x})\,. \tag{4.59}$$

With the degrees of freedom of the semi-discretized problem for each node of triangulation $\mathcal{T}$ merged in a vector

$$\boldsymbol{u}_h = \Big((\mathbf{u}_h^1,\, \xi_h^1), \ldots, (\mathbf{u}_h^n,\, \xi_h^n)\Big)^T \tag{4.60}$$

the variational problem (4.56) can be written as a system of differential-algebraic equations

$$\mathbf{F}\left(t,\, \boldsymbol{u}_h(t),\, \boldsymbol{u}_h'(t)\right) = \mathbf{0}\,, \tag{4.61}$$

with the initial condition

$$\boldsymbol{u}_h(t_0) = \boldsymbol{u}_0\,. \tag{4.62}$$

With the time derivative approximated by the *backward Euler* method the time discretized system (4.61) reads

$$\mathbf{F}\left(t^{n+1},\, \boldsymbol{u}^{n+1},\, \frac{\boldsymbol{u}^{n+1}-\boldsymbol{u}^{n}}{\Delta t}\right) = \mathbf{0}\,, \tag{4.63}$$

with the index n noting the current and index $(n+1)$ noting the next time steps.

The problem (4.63) is in general a nonlinear system of equations solved for $\boldsymbol{u}^{n+1}$ using *Newton*'s method.

4.2.4 Numerical Simulation of Tensile Test

The examples presented in the following are implemented using the finite element analysis software package COMSOL Multiphysics [24] which allows for the modeling of systems of partial differential equations based on the weak formulation.

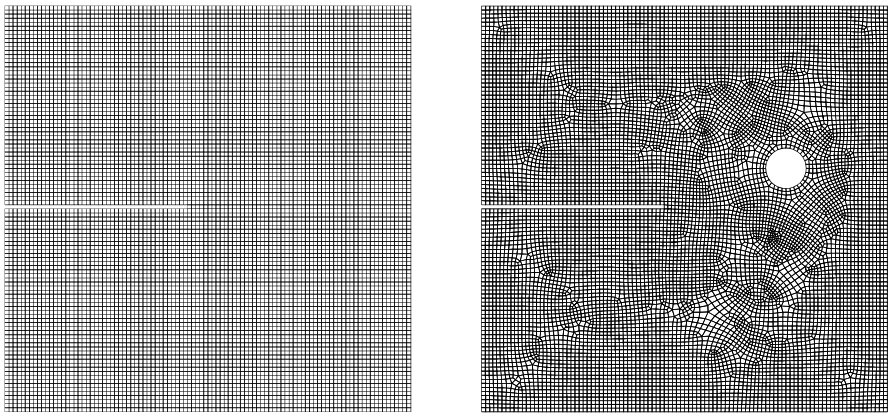

Figure 4.8: Discretized specimen geometries: SEN (left) and SENP (right) specimens.

The discretized specimen geometries used in the benchmarks described in the next sections are depicted in figure (4.8). The single edge notched specimen(SEN) and single edge notched perforated specimen (SENP) geometries

are discretized with quadrilateral elements. Table (4.1) presents an overview of the model parameters used in the current example.

E [MPa]	ν [-]	β [N]	α [MPa]	γ [-]
200	0.33	334	0.16	0.016

Table 4.1: Numerical tensile test. Model parameters.

SEN-specimen

In the present example, a tensile test is performed using the SEN-specimen. The boundary conditions are depicted in figure (4.9). The computation is performed with monotonic driven displacements with an increment of $\Delta u = 1$ mm.

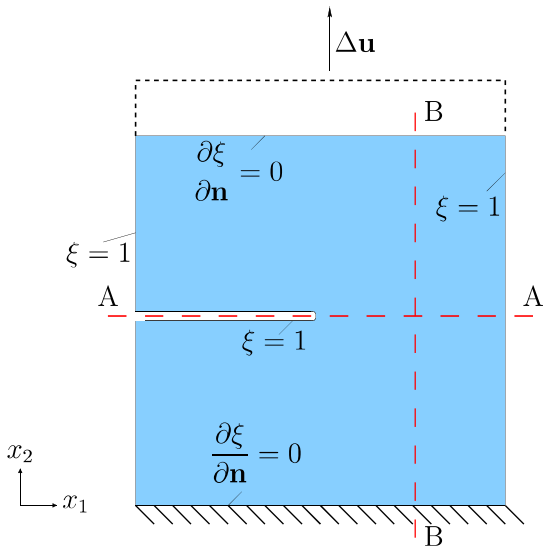

Figure 4.9: Boundary conditions of tensile test.

The Dirichlet boundary condition $\xi = 1$ is chosen to describe the influence of free boundaries on the connectivity, i. e. to take into account the reduced connectivity close to free boundaries. In contrast, the Neumann boundary condition $\frac{\partial \xi}{\partial \mathbf{n}} = 0$ is chosen in the sense of a symmetry condition. In this case $\hat{s} = 0$ preserves the connectivity close to these boundaries.

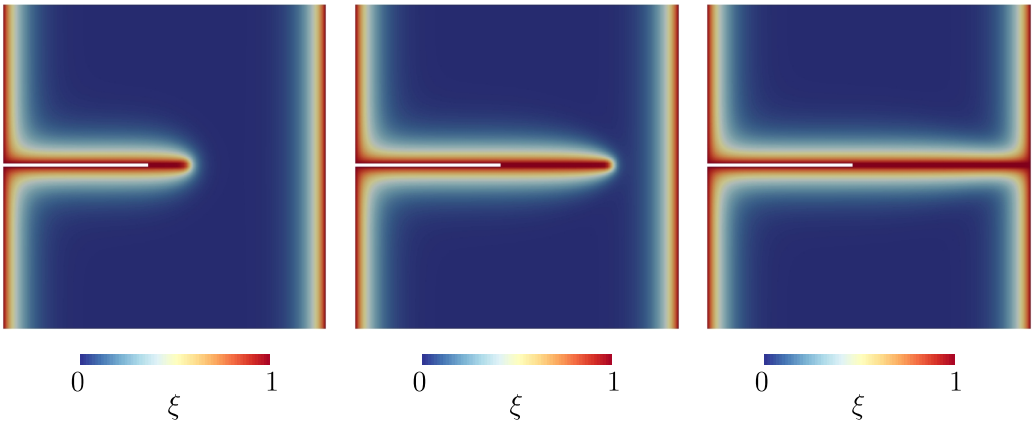

Figure 4.10: Damage propagation under tensile loading: $\Delta u = 13$ mm (left), $\Delta u = 15$ mm (middle), $\Delta u = 16$ mm (right).

The evolution of the damage zone during the tensile test is displayed in figure (4.10). The red color corresponds to the state of the total damage where the connections to the neighboring cells are lost and the blue color displays the undamaged state of the structure where all of the connections to the neighbors are present.

The damage is initiated at the notch tip and grows in horizontal direction towards the right boundary of the specimen. The distribution of von Mises stress values during the tensile test is shown in figure (4.11). The comparison of the results of stress and damage zone calculations indicates that the

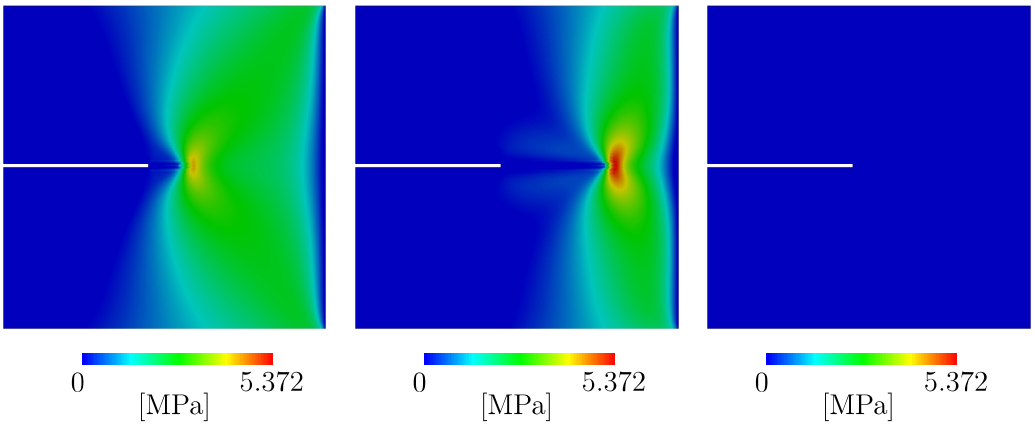

Figure 4.11: Von Mises stress under tensile loading: $\Delta u = 13$ mm (left), $\Delta u = 15$ mm (middle), $\Delta u = 16$ mm (right).

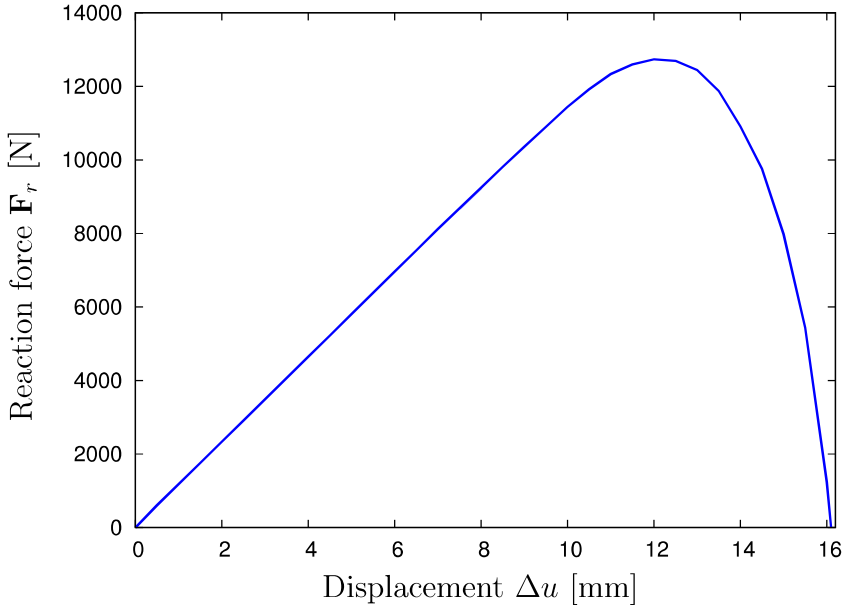

Figure 4.12: Tensile test. Force-displacement curve.

maximum stress values are at all times located around the damage zone tip while the structure is unloaded in the regions of growing damage. The force-displacement curve obtained in the tensile test is shown in diagram (4.12). The displacement value at which the maximum reaction force value is reached

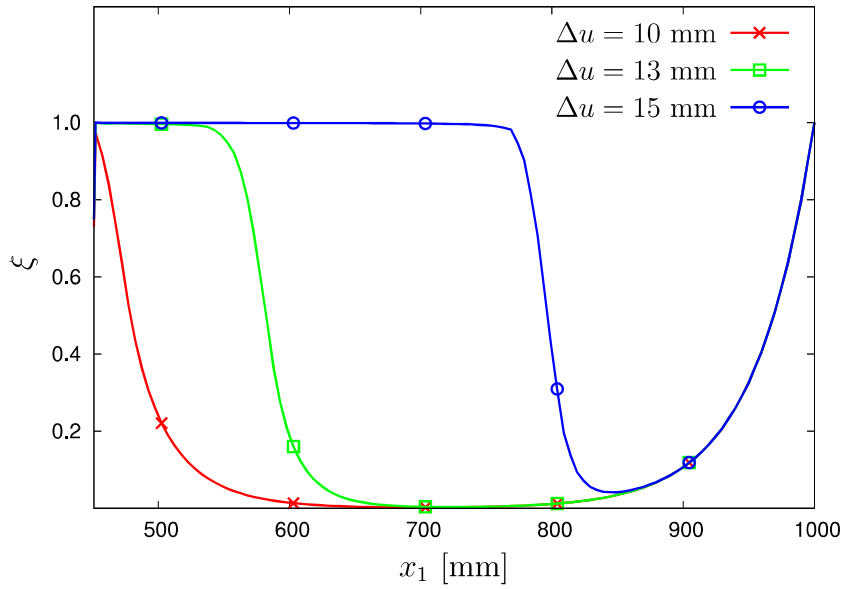

Figure 4.13: Tensile test. Damage tip propagation along cutting line A-A.

corresponds to the initialization of the damage growth around the notch area (figure 4.10). After this point the specimen's overall stiffness is decreasing as the damage zone grows and the connections between cells are deteriorating.

The diagram (4.13) visualizes the profiles of the damage zone tip propagation extracted at the different time points during the tensile test. The red curve represents the position of the damage zone tip at the beginning of the test, so only the area around the notch is affected by damage. The blue curve stands for the damage end state where the damage zone has reached the right boundary. The remaining curves show the positions of the damage zone tip at intermediate stages. The development of the damage zone profile

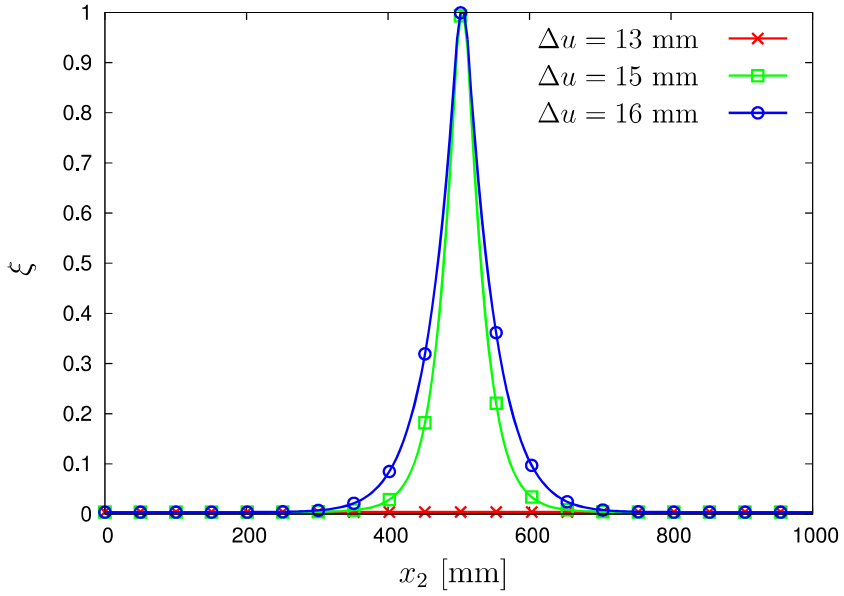

Figure 4.14: Tensile test. Damage zone profiles along cutting line B-B.

is shown in figure (4.14). The comparison of the damage profiles proves that the damage growth rate increases proportional to the amount of damage.

SENP-specimen

In this example, the tensile test is performed using the SENP-specimen. The setup of the test is shown in figure (4.15). Compared to the previous test

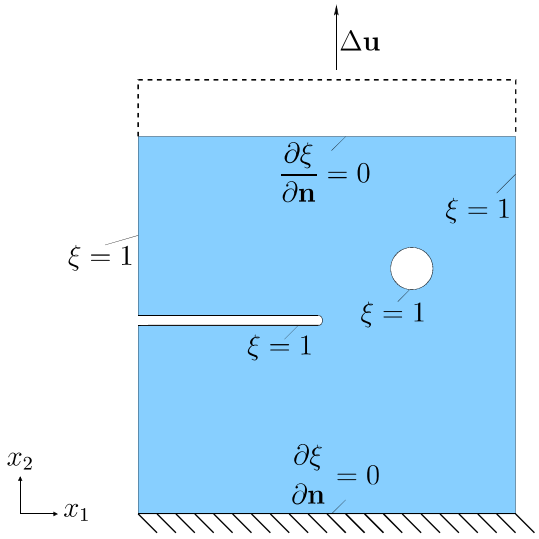

Figure 4.15: Boundary conditions of tensile test (SENP-specimen).

the SENP-specimen leads to a more complex boundary value problem and a non-trivial damage pattern.

Figure (4.16) shows the damage development during the tensile test. The depicted results present a different damage pattern, with the damage zone trajectory first heading towards the perforated area and then in the direction of the boundary on the right-hand side.

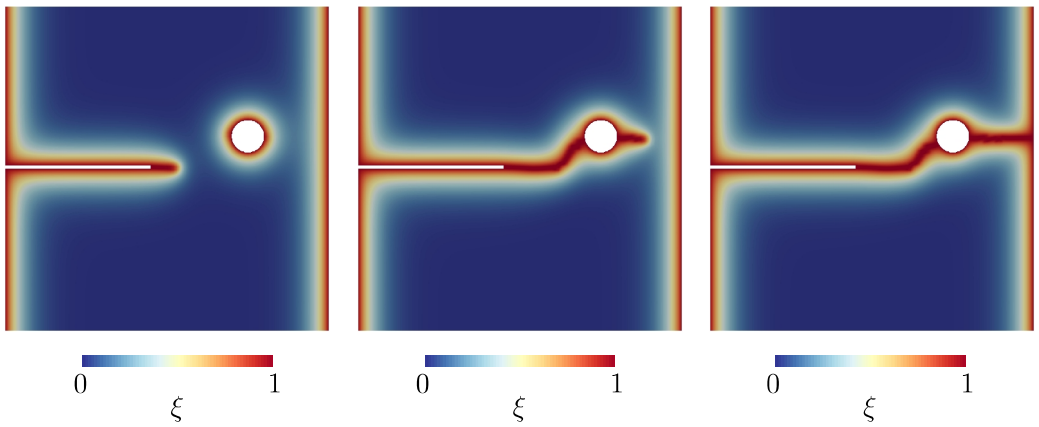

Figure 4.16: SENP-specimen. Damage propagation under tensile loading: $\Delta u = 12$ mm (left), $\Delta u = 13.5$ mm (middle), $\Delta u = 14$ mm (right).

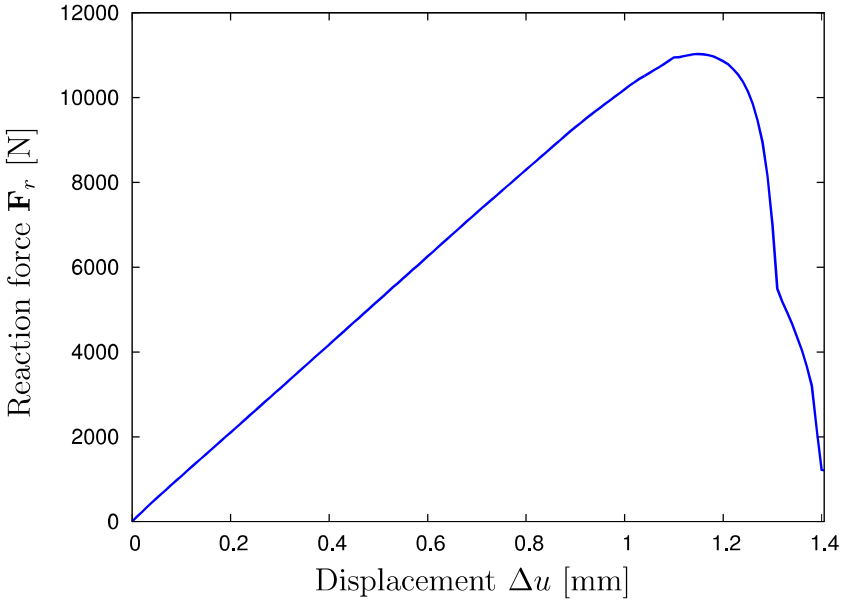

Figure 4.17: SENP-specimen. Force-displacement curve.

The force-displacement curve obtained in the tensile test on SENP-specimen is depicted in figure (4.17). The second knee in the force-displacement curve corresponds to the damage zone reaching the circular hole in the specimen.

4.2.5 Mesh Sensitivity

In the following, we discuss the issue of the damage localization and mesh dependency of the solution. The mesh sensitivity occurring at a certain damage level is a problem emerging from incorporation of the damage evolution in the framework of continuum models (cf. [29]).

With the evolving damage process, the material softening originating from damage may occur. The consequence is the loss of the uniqueness and numerical stability. The problems related to softening and mesh sensitivity are investigated in [9, 30, 98].

The numerical tensile test setup is displayed in figure (4.18). The mesh

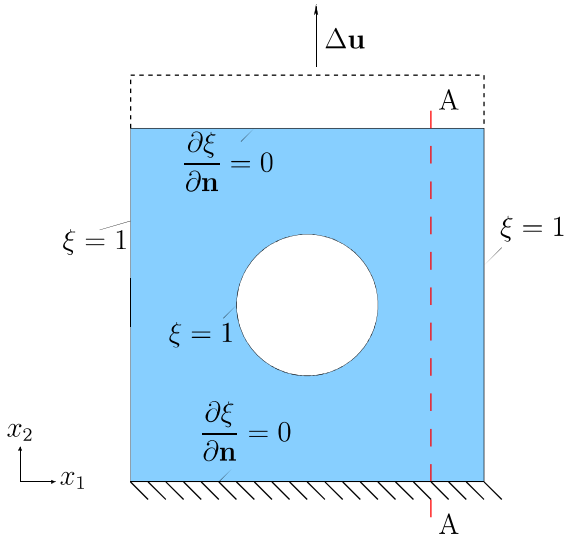

Figure 4.18: Plate with a circular hole under tensile loading. Boundary conditions.

dependency of the order parameter damage model is examined by means of the damage analysis of tensile test performed on a plate with a circular hole using four distinct discretizations displayed in figure (4.19).

The discretizations shown in figures (4.19(a) - 4.19(c)) contain only quadrilateral elements and differ with regard to the element density. The discretization displayed in figure (4.19(d)) is an example of an unstructured grid and consists of triangular elements. The model parameters as well as the basic numerical data are listed in table (4.2).

Parameter	Mesh A	Mesh B	Mesh C	Mesh D
Young's Modulus [Pa]	200			
Poisson's Ratio	0.33			
Diffusion coefficient	0.0033			
Absorption coefficient	0.00166			
Time-scaling coefficient	0.00166			
Number of Elements	1000	3000	12000	3776
Number of Degrees of Freedom	3360	9600	38400	5964

Table 4.2: Sensitivity test. Model parameters.

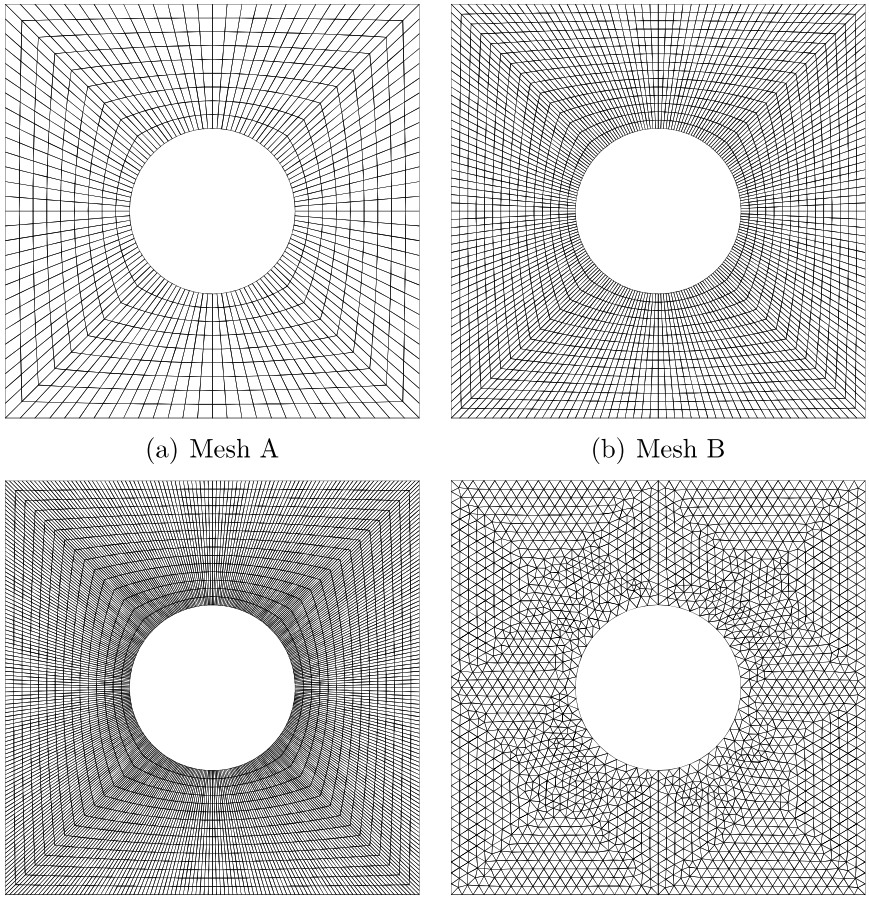

(a) Mesh A (b) Mesh B

(c) Mesh C (d) Mesh D

Figure 4.19: Discretizations of the plate with circular hole.

The damage distributions obtained using different discretizations are shown in figure (4.20). The damage zone in the tensile test propagates in horizontal direction from the hole in the center of the specimen towards the left and right boundaries.

The examination of solutions displayed in figure (4.20) indicates high similarities between the obtained results. A detailed comparison is provided by the damage zone profiles shown in figure (4.21).

These results confirm the mesh independence of the solution. The solution resulting from the coarse mesh "A" appears to be a case where the solution

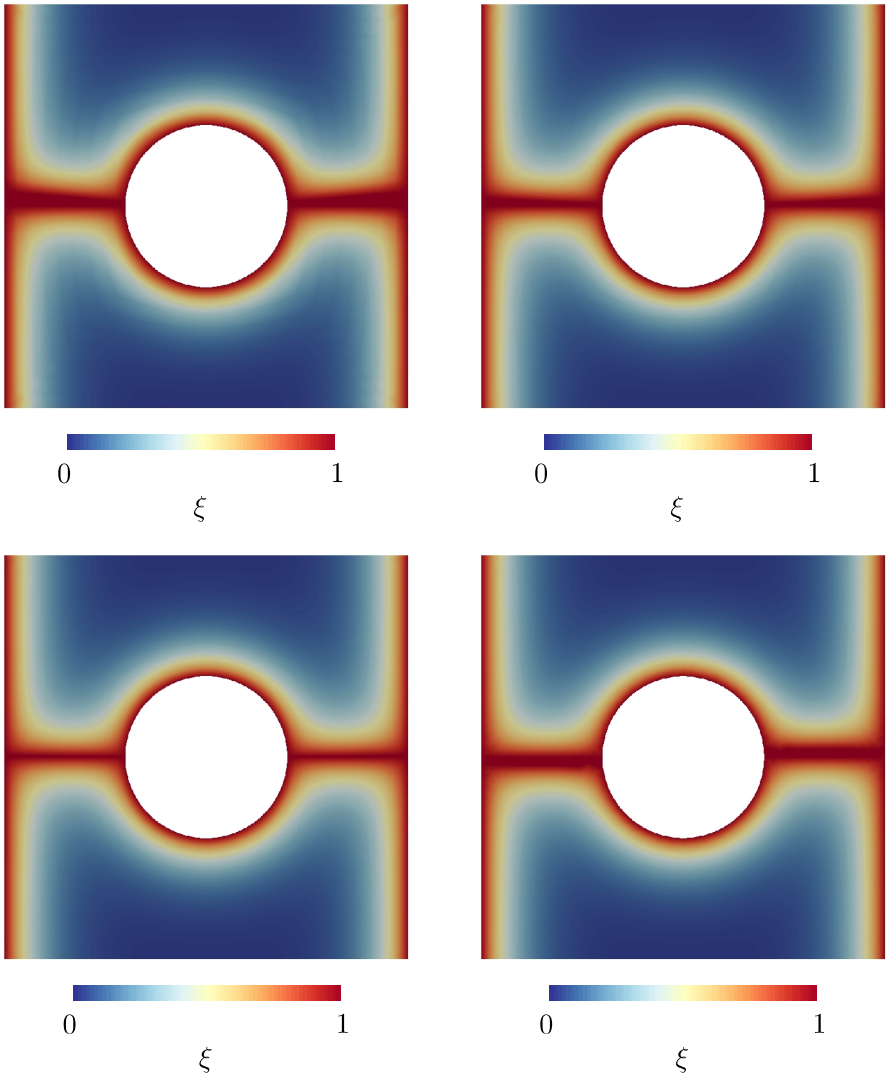

Figure 4.20: Mesh sensitivity test. Damage distribution: Mesh A (top left), Mesh B (top right), Mesh C (bottom left), Mesh D (bottom right).

has not yet converged. The difference between damage zone profiles calculated with mesh "B" and extremely fine mesh "C" is negligibly small. This implies that the solution from the coarser mesh "B" is accurate enough to be considered as a converged solution. The solution corresponding to the unstructured mesh "D" features similar precision as the coarsest structured mesh "A".

Next, we examine the force-displacement relationship. The force-

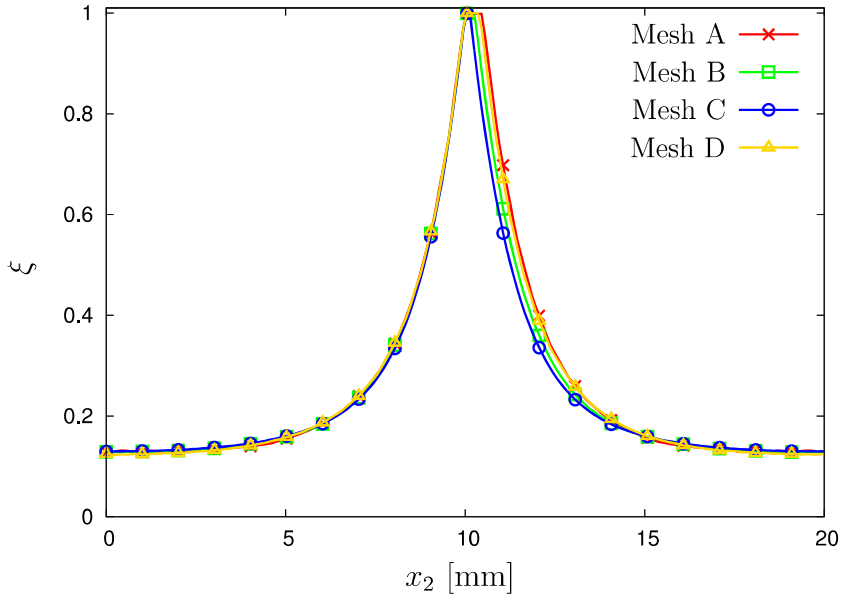

Figure 4.21: Mesh sensitivity test. Damage zone profiles.

displacement curves resulting from performed analysis are presented in figure (4.22). Here, the same situation as with the damage zone profiles is observed. The peak levels of the reaction force curves from mesh "A" and "D" are slightly lower than the peak levels calculated from finer discretizations "B" and "C".

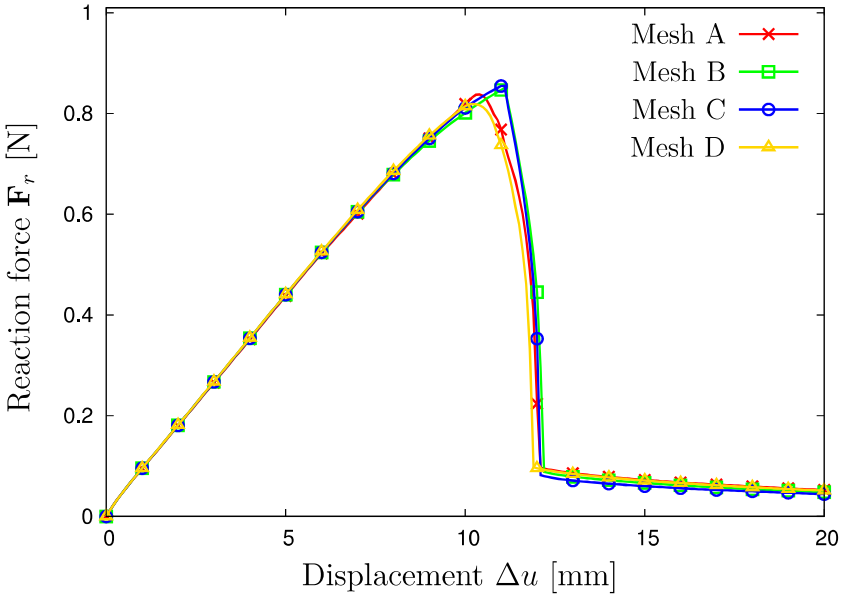

Figure 4.22: Mesh sensitivity test. Force-displacement curves.

The difference between finer meshes ”B” and ”C” as displayed in figure (4.22) becomes even more insignificant.

The relation between reaction force and displacement also clearly shows the mesh independent character of the order parameter damage model with regard to element density as well as the element type.

4.2.6 Model Parameters

The influence of the model parameters on the damage evolution is evaluated in a standard tensile test performed on a SEN-specimen. The values of the damage variable ξ are computed in a point close to the notch tip, the damage zone profiles are evaluated along the cutting line B-B marked with the dashed line (figure 4.23).

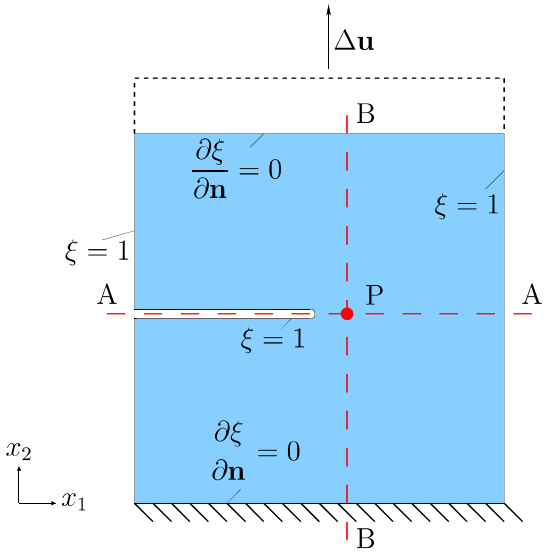

Figure 4.23: Parameters evaluation setup.

Spatial and temporal propagation

We begin with the evaluation of the model parameters such as absorption coefficient α, diffusion coefficient β and time-scaling coefficient γ with regard to damage propagation. In computations corresponding to the results depicted in figures (4.24 - 4.30) the value of the investigated parameter is varied, while the remaining parameters are being held at fixed values.

The time-scaling coefficient γ has an effect primarily on the overall damage propagation rate (figure 4.24). The inspection of the damage zone profiles

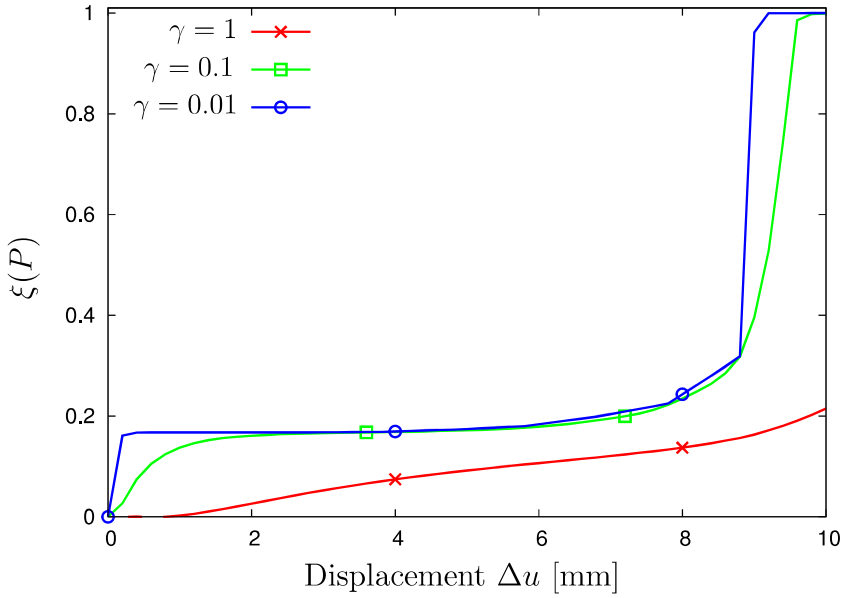

Figure 4.24: Variation of time-scaling coefficient γ. Damage propagation.

shown in figure (4.25) confirms that the damage zone width is barely influenced by the values of parameter γ. The shape of the red curve corresponding to the value of $\gamma = 1$ results from the fact that this value is associated with

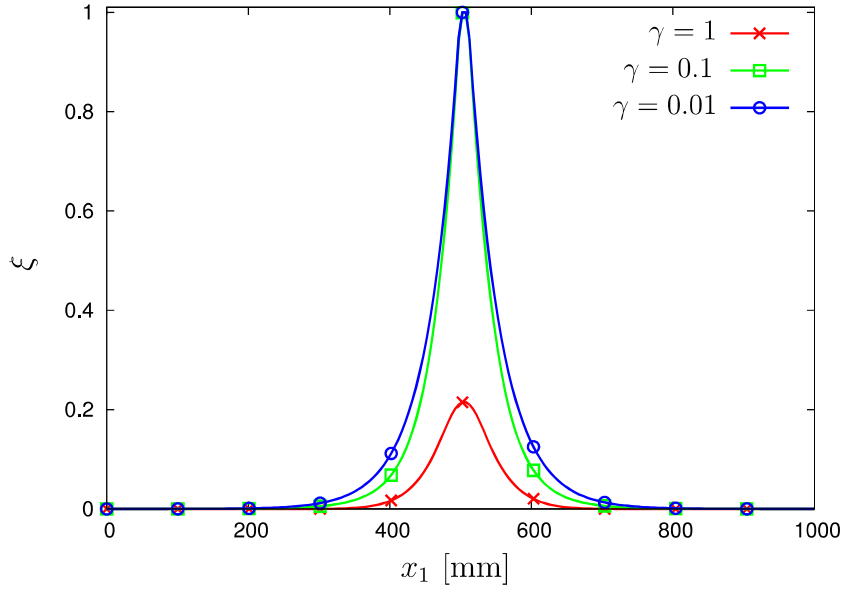

Figure 4.25: Variation of time-scaling coefficient γ. Damage zone profiles along B-B.

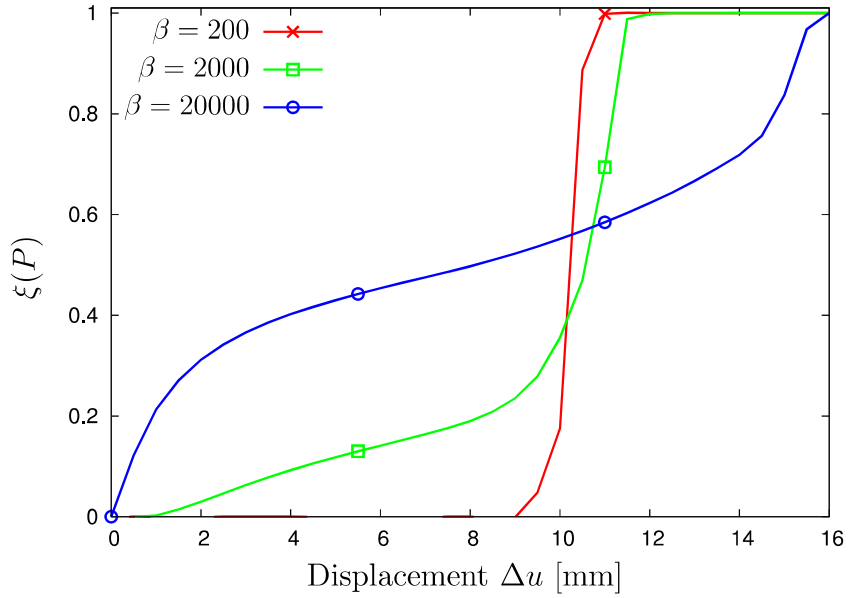

Figure 4.26: Variation of diffusion coefficient β. Damage propagation.

the slow damage propagation rate and at the final time point of $t = 1.0$ the damage has not yet developed. The increasing values of the diffusion parameter β have an effect of speeding up the damage progression (figure

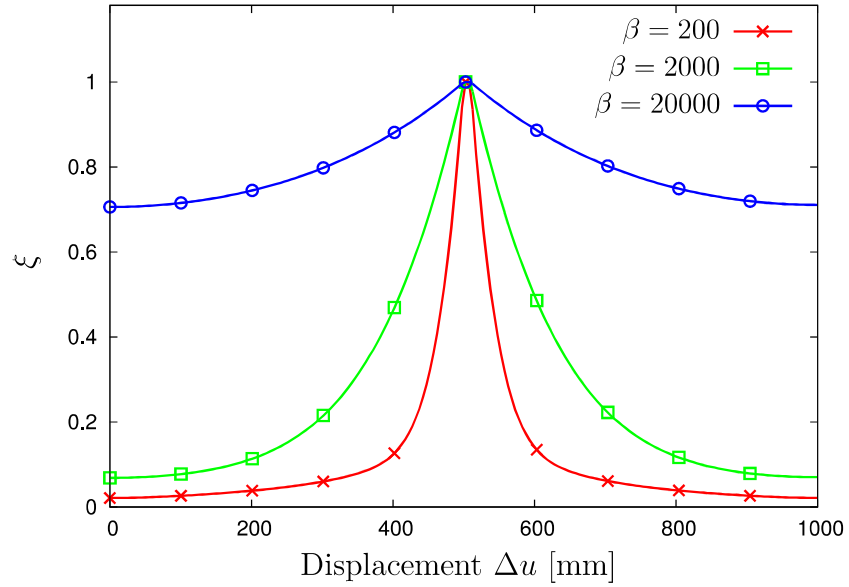

Figure 4.27: Variation of diffusion coefficient β. Damage zone profiles along B-B.

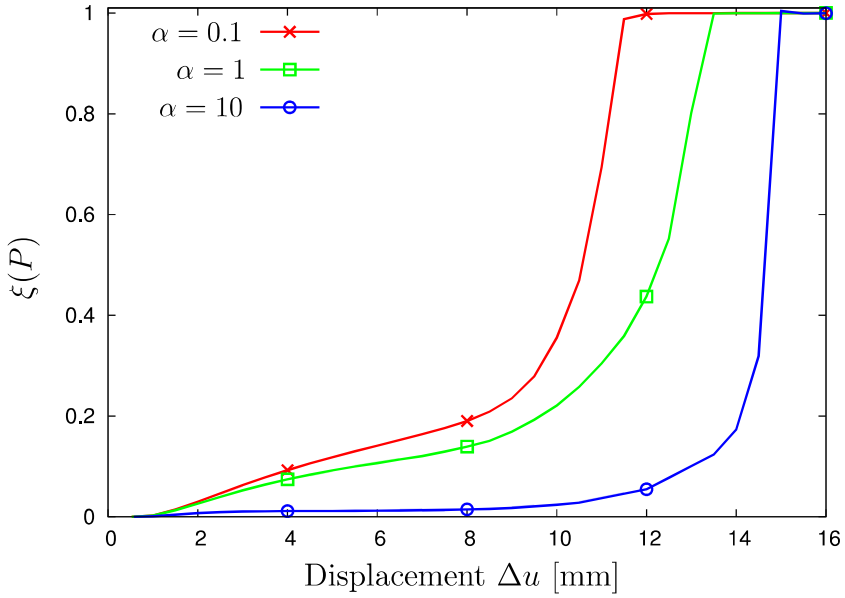

Figure 4.28: Variation of absorption coefficient α. Damage propagation.

4.26). Performing the same with the values of the absorption parameter α as shown in figure (4.28) has an opposite effect on the damage and forces the propagation of the damage zone to slow down.

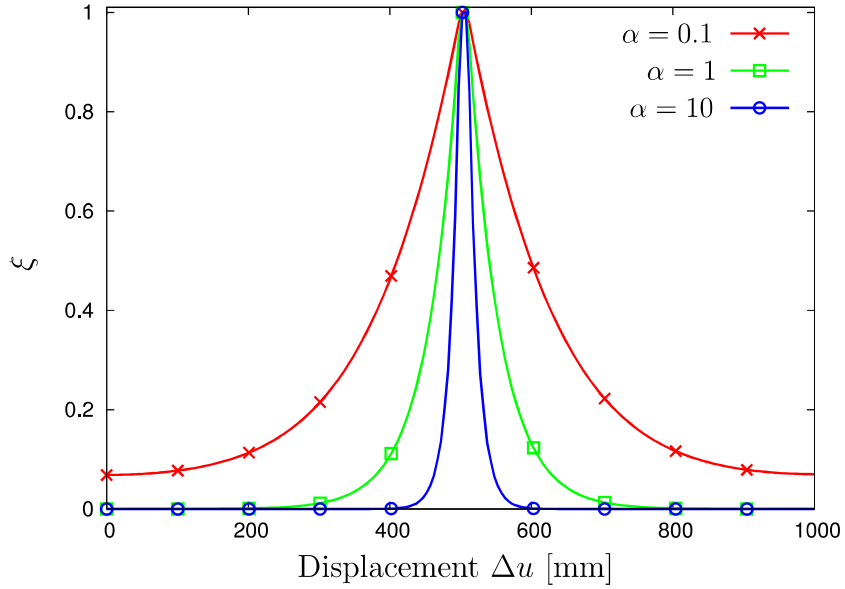

Figure 4.29: Variation of absorption coefficient α. Damage zone profiles along B-B.

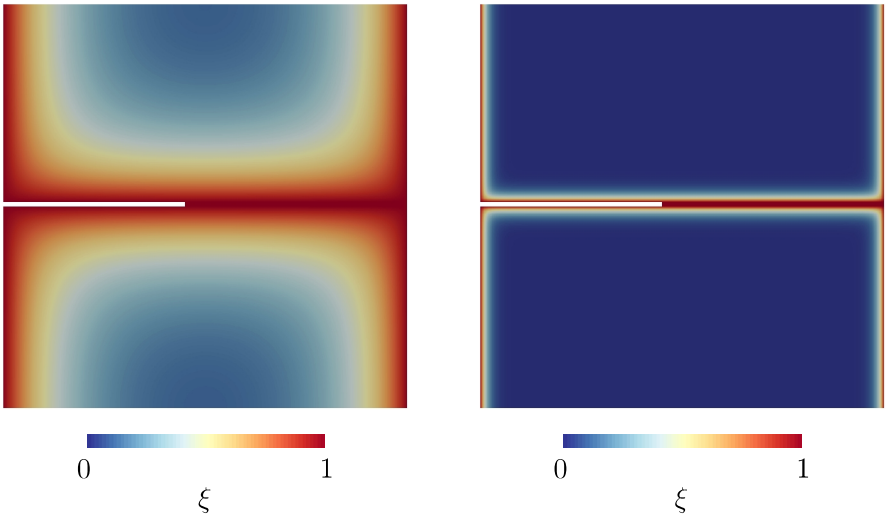

Figure 4.30: Spatial distribution of the damage zone. Absorption coefficient $\alpha = 0.1$ (left) and $\alpha = 10$ (right).

Apart from changes in the damage propagation rate the diffusion parameter β and the absorption parameter α have also a large impact on the spatial properties such as the damage zone width (figures 4.27 and 4.29). The effect related to the propagation rate is also present for the width of the damage zone such that the large values of the diffusion coefficient result in wider damage zones while the large values of the absorption coefficient have an opposite effect. Figure (4.30) demonstrates the influence of the parameter α on the spatial distribution of the damage zone.

Reaction force

Next, we consider the relationship between the model parameters and the reaction force. This issue is of significant importance, since the reaction force is one of the quantities which can be measured in a field experiment.

The inspection of the force-displacement curves shown in figures (4.31 - 4.34) indicates the dependency of the reaction force magnitude on each model parameter. Thus, to adjust the force-displacement curve modeled using the order parameter damage approach to the results of a field experiment each

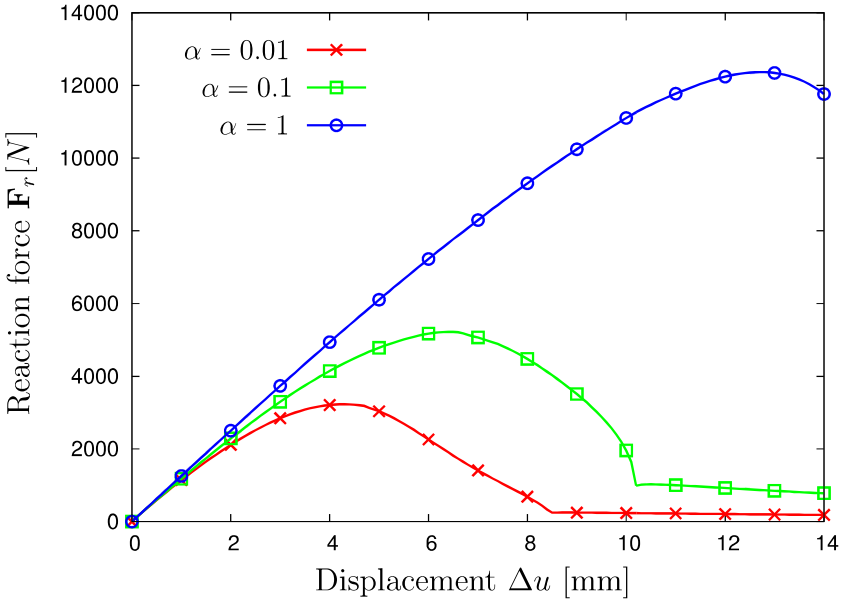

Figure 4.31: Variation of the parameter α. Reaction force.

of the model parameters might be modified. However, since the diffusion and absorption coefficients have an effect on the spatial distribution of the damage the adjustment should be carried out by means of the remaining

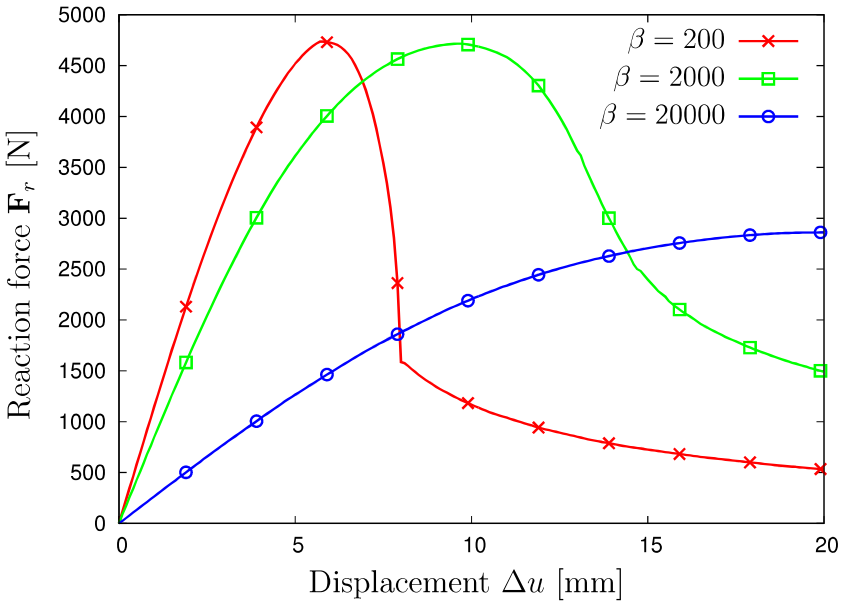

Figure 4.32: Variation of the parameter β. Reaction force.

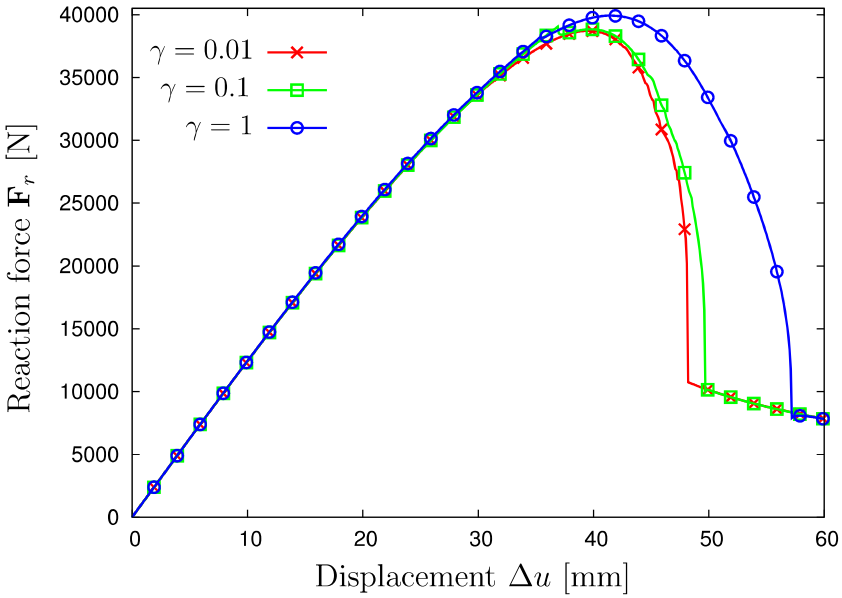

Figure 4.33: Variation of the parameter γ. Reaction force.

model parameters such as time-scaling coefficient γ or Young's modulus E. Since the time-scaling coefficient has an effect on the overall damage rate extreme values of γ would have an effect of total retardation of the damage evolution process. In an extreme case the result would be a failing damage

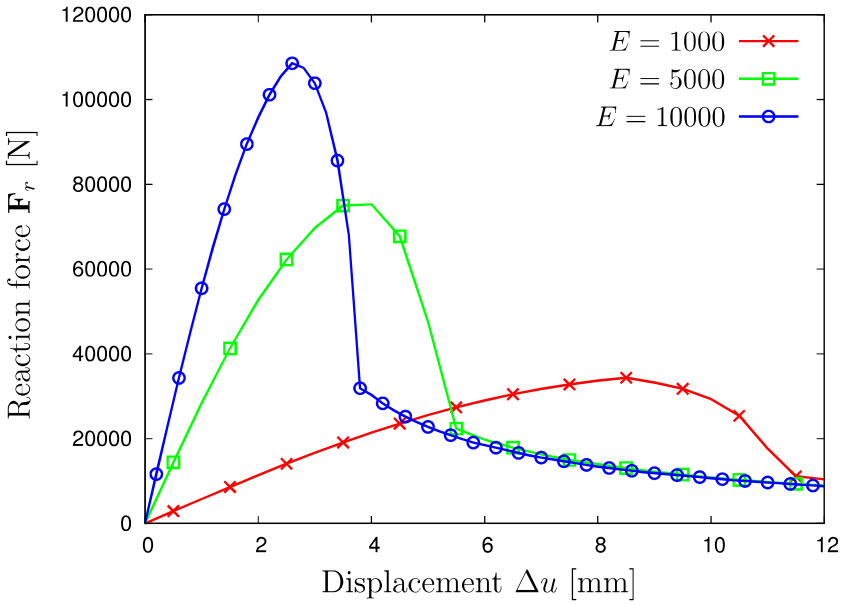

Figure 4.34: Variation of the Young's modulus E. Reaction force.

initiation. With the mentioned considerations the remaining possibility to adjust a force-displacement curve is the Young's modulus E. As the change of the Young's modulus value modifies not only the maximum value of the reaction force but also the point at which this value is achieved, the curve adjustment using single model parameter appears to be a tedious task.

We introduce an additional criterion which drives the damage evolution process by imposing a set of restrictions in the manner of *Kuhn-Tucker conditions* (cf. [15, 74, 101]) on the elastic energy $\tilde{\Psi}_u$ from the evolution equation (4.41)

$$\tilde{\Psi}_u \geq 0\,; \quad H(\varepsilon_1, \varepsilon_c) \geq 0\,; \quad H(\varepsilon_1, \varepsilon_c)\,\tilde{\Psi}_u > 0\,, \tag{4.64}$$

with $H(\varepsilon_1, \varepsilon_c)$ as the Heaviside step function defined as follows

$$H(\varepsilon_1, \varepsilon_c) := \begin{cases} 1\,, & \varepsilon_1 - \varepsilon_c \geq 0 \\ 0\,, & \varepsilon_1 - \varepsilon_c < 0 \end{cases}\,. \tag{4.65}$$

The first condition in (4.64) requires the elastic strain energy to be non-negative. The second requirement demands a certain level of deformation. The last equation in (4.64) implies that the damage evolves only when the elastic energy is non-negative and at the same time some minimum value ε_c of the first principal strain is reached.

Therefore, the parameter ε_c is the strain value at which the coupling between deformation and damage is triggered. As long as the critical strain value is not reached the damage initiation will not occur. Figure (4.35) shows the force-displacement curve and the effect of the critical strain value on the reaction force.

With the increasing values of critical strain the peak value of the reaction force is shifted to the higher strain levels. This scales also the magnitude of the maximum reaction force and moves the damage initiation to larger strain values. Changes in critical strain values do not affect the slope of the curve.

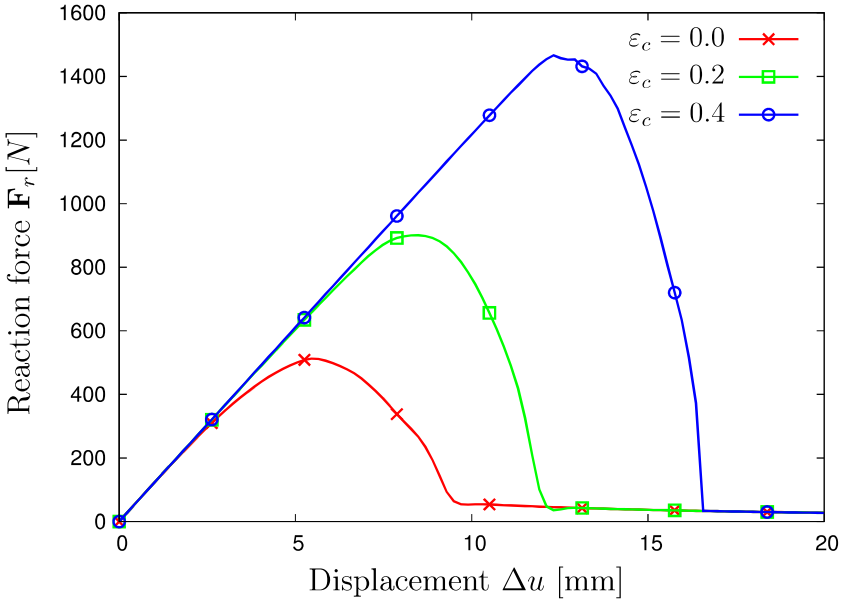

Figure 4.35: Variation of the critical strain ε_c. Reaction force.

Combining the effect of the Young's modulus and critical strain value mentioned above we can adjust the slope and the peak value of the force-displacement curve. Figure (4.36) shows an example where the slope of the

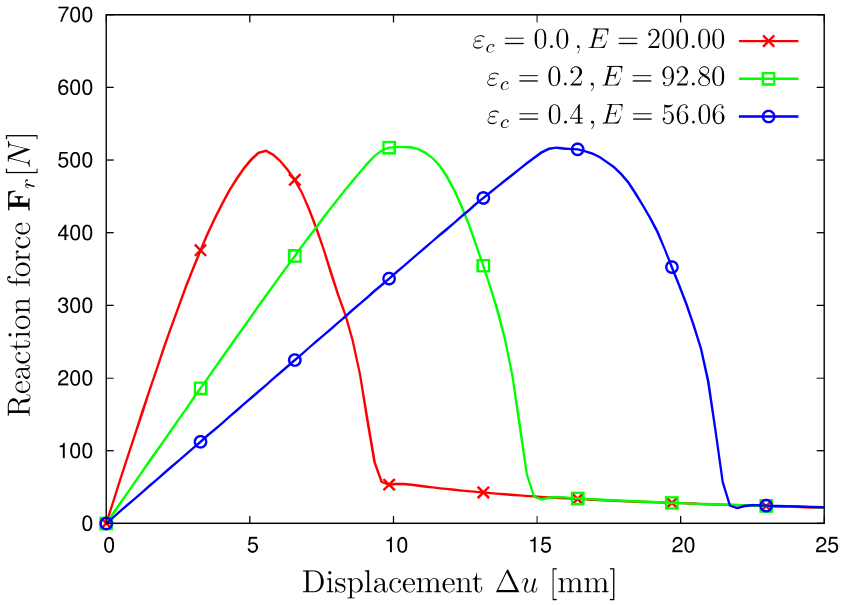

Figure 4.36: Force-displacement curve adjustment.

force-displacement curve is adjusted to a fixed value of the maximum reaction force. This is accomplished by modification of the critical strain value ε_c together with the Young's modulus E.

Behavior under shear loading

In the following, we will discuss the effects of model parameters such as critical strain ε_c and time-scaling coefficient γ on the damage evolution under shear loading.

The geometry of the specimen and the applied boundary conditions can be found in figure (4.37). The computation is performed with monotonic driven displacements with an increment of $\Delta u = 1$ mm.

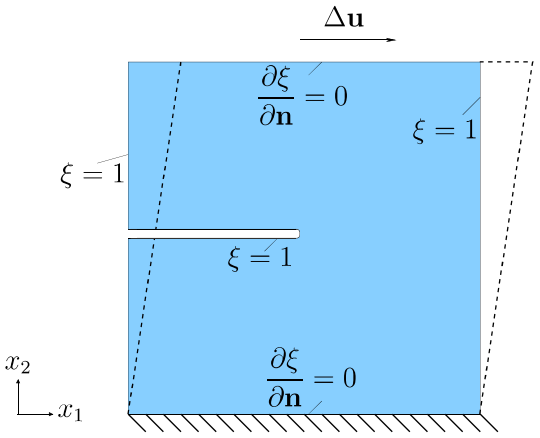

Figure 4.37: Simple shear test. Boundary conditions.

Figure (4.38, left) features simultaneous propagation of the damage zone into two different directions. This damage distribution is obtained using a relatively high value of the time-scaling coefficient $\gamma = 100$. A repeated calculation with a lower time-scaling coefficient value of $\gamma = 10$ leads to a single damage zone path as shown in figure (4.38, right).

The observed effect is similar to the splitting of a single crack into multiple branches, an effect covered in problems regarding dynamic brittle fracture

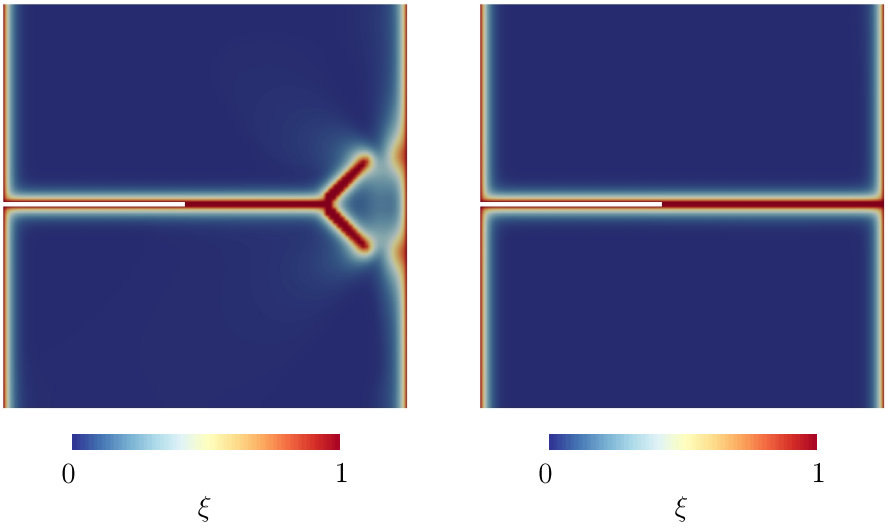

Figure 4.38: Shear loading. Parameter $\gamma = 100$ (left) and $\gamma = 10$ (right).

(cf. [16, 59, 69, 70]) where the branching stability depends on the crack growth speed. Since the time-scaling coefficient γ of the order parameter damage approach controls the overall damage propagation rate it confirms the mentioned analogy.

The damage zone patterns obtained with different values of the critical strain parameter ε_c are displayed in figure (4.39). Under shear loading, this param-

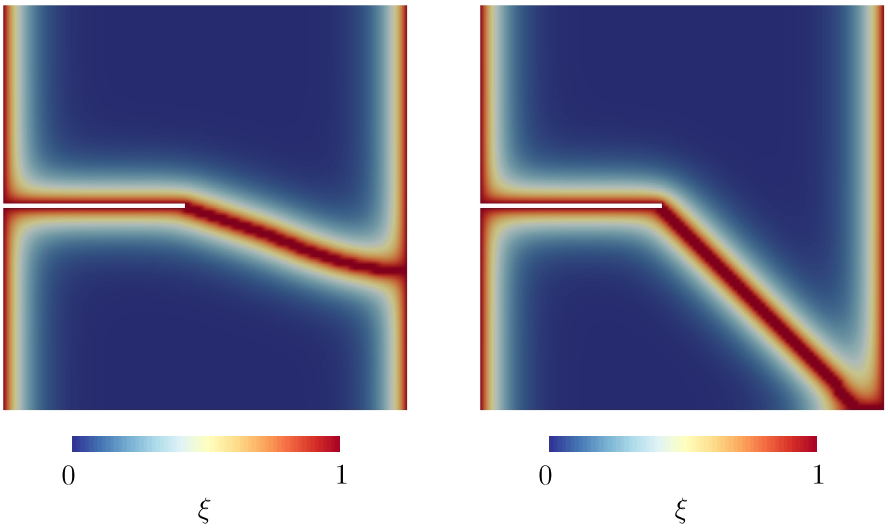

Figure 4.39: Shear loading. Parameter $\varepsilon_c = 0.1$ (left) and $\varepsilon_c = 0.2$ (right).

eter controls the trajectory of the damage zone. The increasing values of the critical strain induce a higher deviation of the damage zone trajectory from the horizontal propagation path (figure 4.39, right).

4.2.7 Additional Microstructural Data

The actual propagation path of the damage zone can be further adjusted using the additional information originating from the microstructure. This is achieved by including directional data such as the local strut orientation of the foam cell. We consider the orientation distribution function (ODF) as a generalization of the directional data representing the fraction of single elements with a particular direction (cf. [68]).

The orientation distribution function $\rho(\mathbf{n})$

$$\rho = \rho(\mathbf{n}) = F_{ij}\, n_i\, n_j\,, \tag{4.66}$$

corresponding to the microstructure of an open-cell foam is approximated using the fabric tensor of the second kind $\mathbf{F}$ and the fabric tensor of the first kind $\mathbf{N}$ (cf. [68, 125])

$$F_{ij} = \frac{15}{2}\left(N_{ij} - \frac{1}{5}\delta_{ij}\right)\,, \tag{4.67}$$

$$N_{ij} = \frac{1}{N}\sum_{k=1}^{N} n_i^{(k)} n_j^{(k)}\,, \tag{4.68}$$

with $\mathbf{n}$ as a unit vector indicating the strut orientation.

The distribution function obtained using the fabric tensor from the equation (4.67) is then incorporated into the evolution equation

$$\frac{\partial \xi}{\partial t} = -\mathrm{div}\left(\beta\, \mathrm{grad}\, \xi\right) + \alpha\, \xi - \tilde{\Psi}_u\, (1-\rho)\,. \tag{4.69}$$

Microstructural Model

As an example we consider a tensile test performed on a SEN-specimen constructed as an artificial foam structure displayed in figure (4.40). The struts of the specimen are discretized using standard Timoshenko beam elements (cf. [87, 100, 120]).

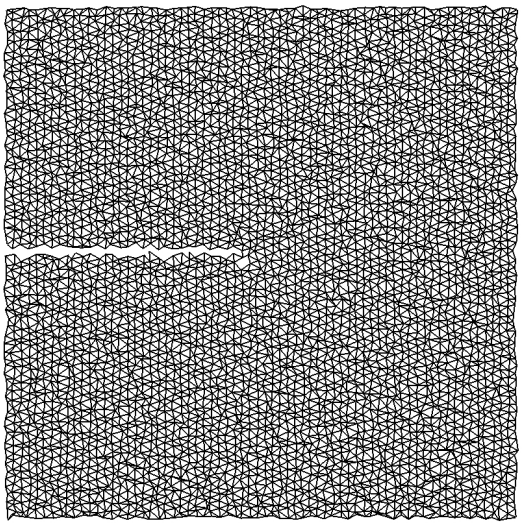

Figure 4.40: Microstructural SEN-specimen.

The computations of the reference model are performed using the finite element analysis solver RADIOSS [106].

For the tensile test computation an element deletion scheme was used where the beam elements with the highest values of the von Mises stress considered as a failed foam struts and being consequently deleted. Figure (4.41) shows the damage propagation in SEN-specimen made with the artificial microstructure.

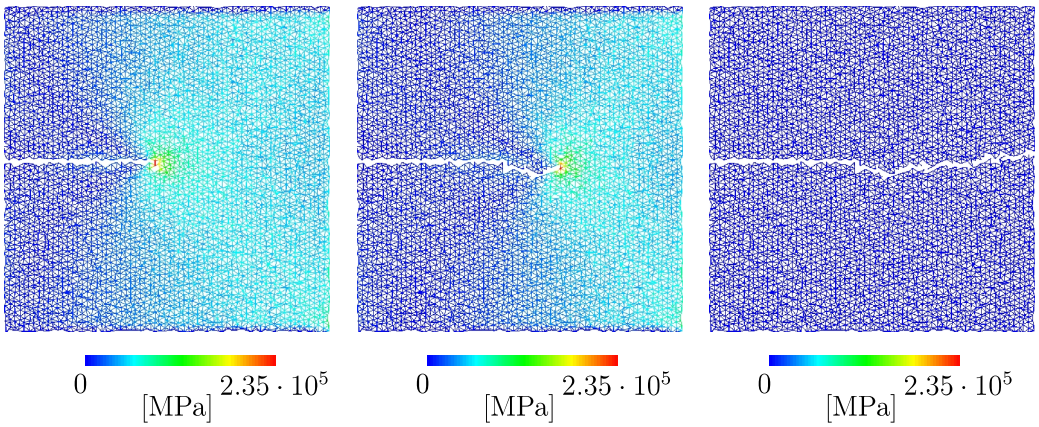

Figure 4.41: Artificial foam structure. Von Mises stress under tensile loading: $t = 0.01$ (left), $t = 0.5$ (middle), $t = 1$ (right).

Order Parameter Model with Directional Data

In the present example the directional data of the beams from the reference microstructural model displayed in figure (4.40) is transferred into the order parameter damage model using the orientation distribution function $\rho(\mathbf{n})$ from the equation (4.66).

Here, the tensile test is performed using the modified order parameter damage formulation presented in equation (4.69).

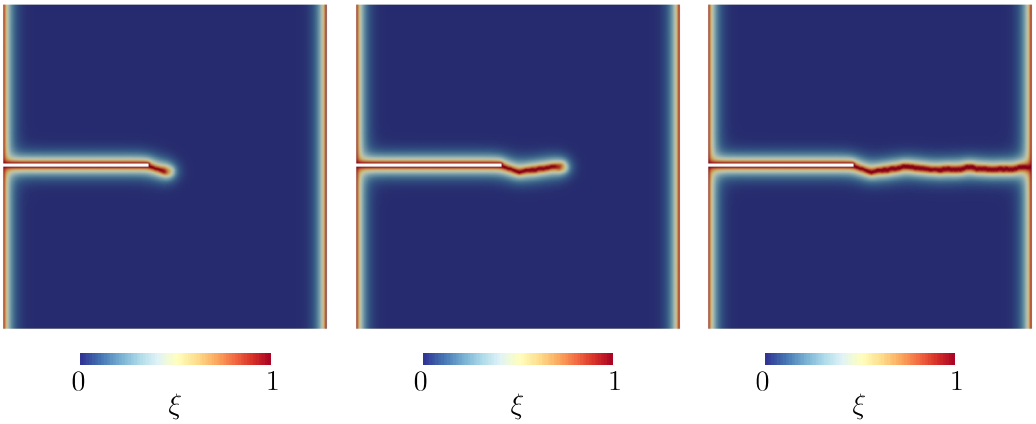

Figure 4.42: Order parameter damage model with directional data. Damage propagation under tensile loading: $\Delta u = 8.2$ mm (left), $\Delta u = 9.3$ mm (middle), $\Delta u = 10$ mm (right).

The obtained damage zone distribution is shown in figure (4.42). The comparison of the damage zone distribution computed using the directional data and the data from the reference model shows a qualitative similarity between the propagation paths.

The incorporation of the microstructural directional data into the order parameter approach in the context of damage mechanics provides higher level of detail to the order parameter damage model for an open-cell foam without full discretization of the microstructure.

4.2.8 Experimental Validation

The order parameter damage model is validated by means of the tensile experiment performed on an open-cell foam SEN-specimen. The specimen geometry is shown in figure (4.43, left). The foam material is an aluminum alloy AlSi7Mg0.3 with the pore size of 10 ppi (pores per inch). The specimen has the dimensions of 40 mm $\times$ 40 mm $\times$ 60 mm with the notch width of 8 mm and the notch tip radius of 4 mm. The upper and lower specimen boundaries were molded into a polyurethane polymer. The molding was necessary in order to mount the specimen in the testing machine. The effective specimen height amounts to 50 mm. The experiment was performed using the *Instron E10000 Linear-Torsion Floor Instrument* [62]. The tensile test was carried out with the strain rate $\dot{\varepsilon} = 0.0003\ \mathrm{s}^{-1}$.

The force-displacement curve obtained in the field experiment is depicted in figure (4.44). This curve serves as reference for the parameters adjustment of the order parameter damage model.

The order parameter damage analysis was performed using the specimen

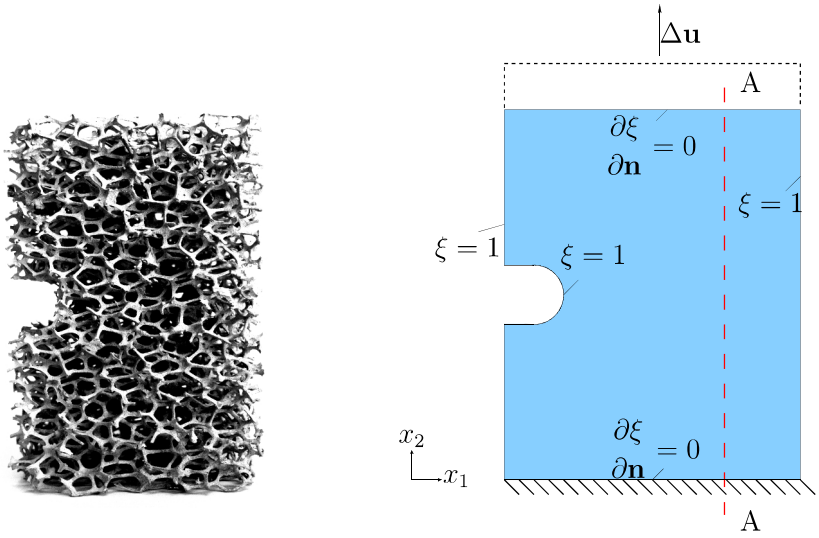

Figure 4.43: Experimental validation. Geometry of the open-cell specimen (left) and macroscopic specimen (right).

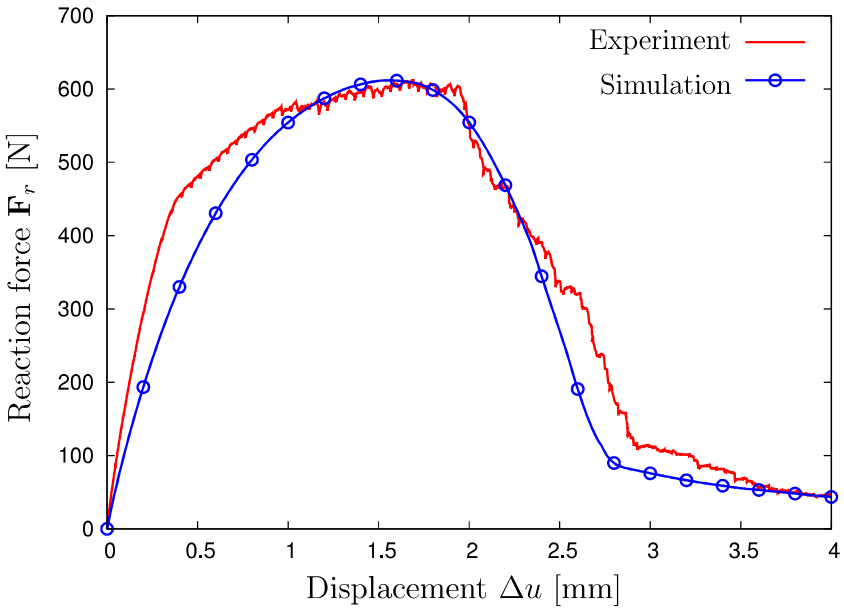

Figure 4.44: Field experiment and damage model. Force-displacement curves.

with dimensions matching a specimen from the field experiment (figure 4.43, right). Due to the extremely low Poisson's ratio values of open cell foams (cf. [53]) the computations were performed based on the assumption of the plane stress deformation state with $T_{33} = 0$.

The model parameters of the macroscopic order parameter damage approach were manually determined to match the general shape of the force-displacement curve and the peak value of the reaction force. The model parameters corresponding to mentioned criteria and basic numerical data are presented in table (4.3). The reaction force curve obtained in the numerical experiment is shown in figure (4.44).

The ascending part of the curve has only a minor significance, since this

E [MPa]	ν [-]	β [N]	α [MPa]	γ [-]	ε_c [-]
44.9	0.03	100	0.1	1	0.046

Table 4.3: Identified parameters of order parameter damage model.

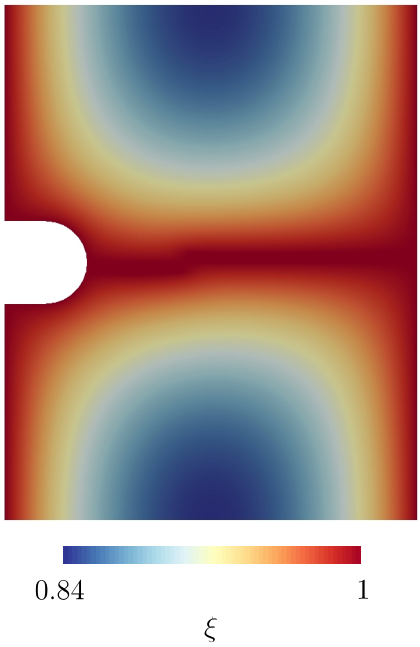

Figure 4.45: Damage distribution in the macroscopic specimen.

part describes the undamaged material. Hence, a higher level of mismatch in this part of the curve is tolerable. The primary importance belongs to the descending part of the force-displacement curve. This curve segment is associated with the damage process where the material loses its strength and the effective material properties get altered.

The damage computation result obtained using the determined parameter set is displayed in figure (4.45). The damage area propagates from the tip of the notch towards the opposite boundary on the right-hand side of the specimen. The profile of the damage region is shown in figure (4.46).

In general, the critical values of the damage variable corresponding to material rupture measured in experiments differ from the theoretical ones. For example, metals can begin to rupture already with the value of the damage variable of 0.2 (cf. [80]). In an open-cell foam material the failure takes place on the level of a single pore or cell strut. The average pore size of the tested open-cell foam specimen is about 4 mm (cf. [52]). Using this characteristic value of the foam we can identify the critical value of the damage specific to

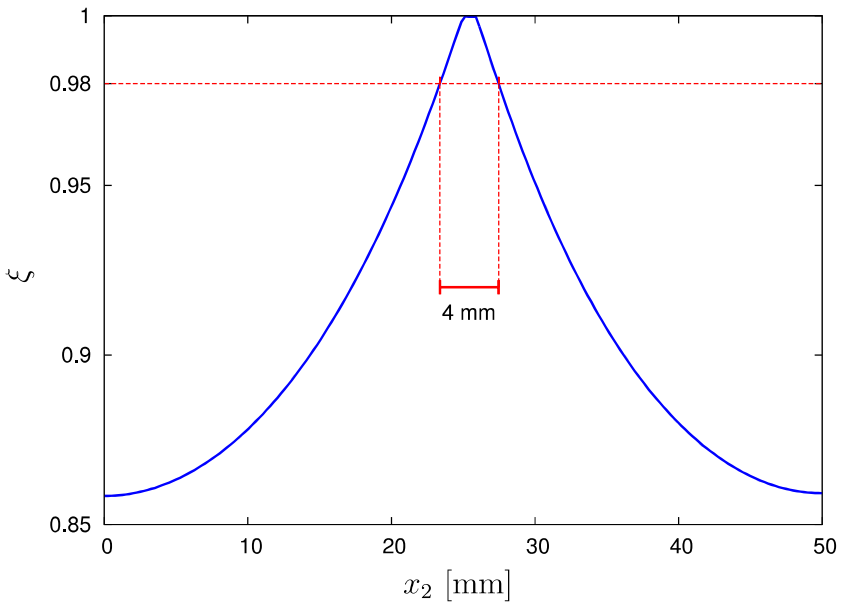

Figure 4.46: Damage zone profile along cutting line A-A.

the tested foam material. In the present case depicted in figure (4.46) the critical damage value can be identified to the value of $\xi \approx 0.98$.

The numerically obtained curve shows qualitative agreement with the results of the field experiment and demonstrates the capability of the order parameter damage model. To attain a higher level of agreement between the presented approach and a real experiment further constitutive models can be included into the order parameter model.

5

Conclusion

The order parameter approach and its applications were explored in the presented work. The order parameter is a characteristic value representing the microstructure. With this additional parameter the macroscopic model is extended to include effects attributed to the underlying microscopic level. This versatile and flexible approach overcomes the shortcomings of the classical continuum theory.

The order parameter formulation was utilized to describe the scale effect where the effective material properties show the dependency on the specimen size. The open-cell foam materials are a class of materials with notable presence of the mentioned scale effect. This effect was investigated using a computational micromechanical model of high resolution as a reference. The finite element representation of the foam material based on standard beam elements was created and a set of tensile and simple shear virtual tests was carried out in order to characterize the effective macroscopic mechanical properties and to extract the key material data.

The proposed approach was investigated as an alternative to the extended continuum theory such as the micropolar continuum which is known for the ability to cover scale effects under particular loading mechanisms. The micropolar model fails, however, to reproduce the scale effect under tensile loading. In this context, the advantage of the order parameter approach becomes obvious, since this approach actually describes the size-dependent behavior in tensile as well as in shear loading modes.

Although the modeling of the size-dependent material behavior can be performed by both micropolar and order parameter approaches, it is only possible with the set of appropriate model parameters. Yet, another problem emerges, namely, the problem of parameters identification. The respective model parameters were identified by formulating the inverse problem, which in turn was stated as an optimization problem. This problem was solved using the stochastic method such as genetic algorithm, since the gradient-based methods may reach the local minimum before finding the global one and suffer stability problems due to a high sensitivity of the solution of the micropolar problem with respect to the model parameters.

The flexibility of the order parameter approach was further demonstrated by formulating the continuum damage mechanics model based on the order parameter approach. For this purpose, a damage variable based on the microstructural property of an open-cell foam such as connectivity number was associated with the order parameter.

The developed damage formulation was enhanced with an additional structural property derived from the foam strut orientation. This way the qualitative precision of the spatial distribution of the damage zone was increased.

The examination of the proposed damage formulation with regard to mesh sensitivity has shown that the results are fairly independent from the chosen discretization. The influence of the model parameters was investigated, thus, providing a detailed insight into the model behavior.

The straightforward procedure of the parameters adjustment of the macroscopic damage model to the results obtained in a tensile test field experiment performed on an open-cell aluminum foam specimen served as a bridge between the numerical simulation and a real world experiment. The comparison with the field experiment results proves the capability and flexibility of the proposed damage approach and demonstrates again the versatility of the order parameter modeling. Further investigation and a detailed parameter identification with respect to the experiments will be provided in future work.

Although only linear elastic material behavior was considered, the proposed model can be further extended with regard to more complex constitutive models (e. g. hyperelastic behavior of elastomers) as well as finite strain theory. Apart from the coupling of the order parameter damage field with the deformation state additional damage mechanisms such as chemical (e. g. acid) or physical (e. g. humidity) can be incorporated into the model formulation.

Bibliography

[1] H.-D. Alber. Evolving microstructure and homogenization. *Continuum Mechanics and Thermodynamics*, 12(4):235–287, 2000.

[2] D. H. Allen. Homogenization principles and their application to continuum damage mechanics. *Composites Science and Technology*, 61(15):2223–2230, 2001.

[3] E. Andrews, W. Sanders, and L. J. Gibson. Compressive and tensile behaviour of aluminum foams. *Materials Science and Engineering: A*, 270(2):113–124, 1999.

[4] D. N. Arnold, F. Brezzi, and M. Fortin. A stable finite element for the stokes equations. *Calcolo*, 21(4):337–344, 1984.

[5] A. Artemev, Y. Jin, and A. G. Khachaturyan. Three-dimensional phase field model of proper martensitic transformation. *Acta Materialia*, 49(7):1165–1177, 2001.

[6] A.F. Bastawros, H. Bart-Smith, and A.G. Evans. Experimental analysis of deformation mechanisms in a closed-cell aluminum alloy foam. *Journal of the Mechanics and Physics of Solids*, 48(2):301–322, 2000.

[7] K.-J. Bathe and P. Zimmermann. *Finite-Elemente-Methoden - Matrizen und lineare Algebra, die Methode der finiten Elemente, Lösung von Gleichgewichtsbedingungen und Bewegungsgleichungen.* Springer, Berlin, Heidelberg, 1 edition, 1990.

[8] Z. P. Bazant. Recent advances in failure localization and nonlocal models. *Micromechanics of Failure*, 1990.

[9] Z. P. Bazant and G. Pijaudier-Cabot. Nonlocal continuum damage, localization instability and convergence. *Journal of Applied Mechanics*, 55(2):287–293, 1988.

[10] E. Becker and W. Bürger. *Kontinuumsmechanik*. Teubner, 1975.

[11] H.G. Beyer. *The theory of evolution strategies*. Springer, 2001.

[12] R. Billardon and I. Doghri. Localization bifurcation analysis for damage softening elastoplastic materials. *Cracking and Damage-Strain Localization and Size Effect, Elsevier, London, New York*, pages 295–303, 1989.

[13] S. B. Biner and S. Y. Hu. Simulation of damage evolution in composites: A phase-field model. *Acta Materialia*, 57(7):2088–2097, 2009.

[14] W.J. Boettinger, J.A. Warren, C. Beckermann, and A. Karma. Phase-field simulation of solidification. *Annual review of materials research*, 32(1):163–194, 2002.

[15] J. Bonet and R. D. Wood. *Nonlinear Continuum Mechanics for Finite Element Analysis*. Cambridge University Press, Cambridge, 2008.

[16] E. Bouchbinder, J. Mathiesen, and I. Procaccia. Branching instabilities in rapid fracture: Dynamics and geometry. *Physical Review E*, 71(5):056118, 2005.

[17] J. W. Cahn and J. E. Hilliard. Free energy of a nonuniform system. i. interfacial free energy. *The Journal of chemical physics*, 28(2):258–267, 1958.

[18] G. Capriz. Continua with latent microstructure. *Archive for Rational Mechanics and Analysis*, 90(1):43–56, 1985.

[19] G. Capriz. *Continua with microstructure*, volume 35. Springer-Verlag New York, 1989.

[20] J. L. Chaboche. Le concept de contrainte effective appliqué à l'élasticité et à la viscoplasticité en présence d'un endommagement anisotrope. In *Mechanical Behavior of Anisotropic Solids/Comportment Méchanique des Solides Anisotropes*, pages 737–760. Springer, 1982.

[21] A. Chatzouridou and S. Diebels. Identification of material parameters in extended contiuum mechanical models. *PAMM*, 5(1):495–496, 2005.

[22] L.-Q. Chen. Phase-field models for microstructure evolution. *Annual Review of Materials Science*, 32:113–140, 2002.

[23] B. D. Coleman and W. Noll. The thermodynamics of elastic materials with heat conduction and viscosity. *Archive for Rational Mechanics and Analysis*, 13(1):167–178, 1963.

[24] COMSOL Multiphysics. *Version 3.5a.* COMSOL AB, Stockholm, Sweden, 2009.

[25] E. Cosserat, F. Cosserat, M. Brocato, and K. Chatzis. *Théorie des corps déformables.* A. Hermann Paris, 1909.

[26] R. de Boer. *Vektor- und Tensorrechnung für Ingenieure.* Springer, Berlin, Heidelberg, 1982.

[27] R. de Borst. Simulation of strain localization: a reappraisal of the cosserat continuum. *Engineering computations*, 8(4):317–332, 1991.

[28] R. de Borst. A generalisation of j2-flow theory for polar continua. *Computer Methods in Applied Mechanics and Engineering*, 103(3):347–362, 1993.

[29] R. de Borst, M. A. Crisfield, J. J. C. Remmers, and C. V. Verhoosel. *Nonlinear Finite Element Analysis of Solids and Structures.* John Wiley & Sons, New York, 2012.

[30] R. de Borst, L. J. Sluys, H.-B. Muhlhaus, and J. Pamin. Fundamental issues in finite element analyses of localization of deformation. *Engineering computations*, 10(2):99–121, 1993.

[31] F. Dell'Isola, G. Sciarra, and S. Vidoli. Generalized hooke's law for isotropic second gradient materials. *Proceedings of the Royal Society A: Mathematical, Physical and Engineering Science*, pages rspa–2008, 2009.

[32] S. Diebels. *Mikropolare Zweiphasenmodelle - Formulierung auf der Basis der Theorie poröser Medien.* Inst. für Mechanik (Bauwesen), Stuttgart, 2000.

[33] S. Diebels and H. Steeb. The size effect in foams and its theoretical and numerical investigation. *Proceedings of the Royal Society of London. Series A: Mathematical, Physical and Engineering Sciences*, 458(2028):2869–2883, 2002.

[34] S. Diebels and H. Steeb. Stress and couple stress in foams. *Computational materials science*, 28(3):714–722, 2003.

[35] J. Dufailly and J. Lemaitre. Modeling very low cycle fatigue. *International Journal of damage mechanics*, 4(2):153–170, 1995.

[36] J. E. Dunn and J. Serrin. On the thermomechanics of interstitial working. In *The Breadth and Depth of Continuum Mechanics*, pages 705–743. Springer, 1986.

[37] R. Eberhart and J. Kennedy. A new optimizer using particle swarm theory. In *Proceedings of the sixth international symposium on micro machine and human science*, volume 1, pages 39–43. New York, NY, 1995.

[38] T. Ebinger, H. Steeb, and S. Diebels. Modeling macroscopic extended continua with the aid of numerical homogenization schemes. *Computational materials science*, 32(3):337–347, 2005.

[39] Britannica Editors. Cancellous bone. In *Encyclopedia Britannica.* http://www.britannica.com/EBchecked/topic/92222/cancellous-bone, 2014.

[40] V. A. Eremeyev, L. P. Lebedev, and H. Altenbach. *Foundations of micropolar mechanics*. Springer, 2013.

[41] A. C. Eringen. *Linear theory of micropolar elasticity*. DTIC Document, 1965.

[42] A. C. Eringen. *Mechanics of micromorphic continua*. Springer, 1968.

[43] A. C. Eringen. *Continuum Physics: Polar and non-local field theories*, volume 4. Elsevier, Amsterdam, 1976.

[44] A. C. Eringen. *Microcontinuum field theories, Vol. 1.* Springer, NY, 1998.

[45] F. Feyel. Multiscale FE^2 elastoviscoplastic analysis of composite structures. *Computational materials science*, 16(1):344–354, 1999.

[46] F. Feyel. A multilevel finite element method (FE^2) to describe the response of highly non-linear structures using generalized continua. *Computer Methods in applied Mechanics and engineering*, 192(28):3233–3244, 2003.

[47] J. Fish and Q. Yu. Multiscale damage modelling for composite materials: theory and computational framework. *International Journal for Numerical Methods in Engineering*, 52(1-2):161–191, 2001.

[48] S. Forest. Micromorphic approach for gradient elasticity, viscoplasticity, and damage. *Journal of Engineering Mechanics*, 135(3):117–131, 2009.

[49] S. Ghosh. Multiple scale analysis of damage and texture evolution in real heterogeneous materials. Technical report, DTIC Document, 1999.

[50] L. J. Gibson and M. F. Ashby. *Cellular solids: structure and properties*. Cambridge university press, 1999.

[51] L. J. Gibson, T. Pardoen, and P. R. Onck. Size effects in foams: Experiments and modeling. *Progress in Materials Science*, 56(2):109–138, 2011.

[52] D. Gierlich, C. Kühn, K. Hackeschmidt, and R. Riedl. Mechanical properties of open-pored aluminium foams (mechanische kenndaten offenporiger aluminiumschäume). *Konstruktion*, 9:69–74, 2004.

[53] G. Gioux, T. M. McCormack, and L. J. Gibson. Failure of aluminum foams under multiaxial loads. *International Journal of Mechanical Sciences*, 42(6):1097–1117, 2000.

[54] A. L. Gurson. Continuum theory of ductile rupture by void nucleation and growth: Part i—yield criteria and flow rules for porous ductile media. *Journal of engineering materials and technology*, 99(1):2–15, 1977.

[55] M. E. Gurtin. Generalized ginzburg-landau and cahn-hilliard equations based on a microforce balance. *Physica D: Nonlinear Phenomena*, 92(3):178–192, 1996.

[56] M. E. Gurtin, E. Fried, and L. Anand. *The Mechanics and Thermodynamics of Continua*. Cambridge University Press, Cambridge, 1 edition, 2010.

[57] Z. Hashin. Theory of mechanical behavior of heterogeneous media. *Appl. Mech. Rev.*, 17(1):1–9, 1964.

[58] P. Haupt and J. A. Kurth. *Continuum Mechanics and Theory of Materials*. Springer Science & Business Media, Berlin Heidelberg, 2nd ed. 2002 edition, 2002.

[59] H. Henry. Study of the branching instability using a phase field model of inplane crack propagation. *EPL (Europhysics Letters)*, 83(1):16004, 2008.

[60] R. Hill. A self-consistent mechanics of composite materials. *Journal of the Mechanics and Physics of Solids*, 13(4):213–222, 1965.

[61] G. A. Holzapfel. *Nonlinear Solid Mechanics - A Continuum Approach for Engineering*. Wiley, New York, 1 edition, 2000.

[62] INSTRON. *Instron E10000 Linear-Torsion Floor Instrument.* Worldwide Headquarters, Norwood, Massachusetts, USA, 2014.

[63] R. Jänicke and S. Diebels. Numerical homogenisation of micromorphic media. *Technische Mechanik*, 30(4):364–373, 2010.

[64] M. G. Johlitz. *Experimentelle Untersuchung und Modellierung von Maßstabseffekten in Klebungen.* Shaker, 2008.

[65] L. Kachanov. *Introduction to continuum damage mechanics*, volume 10. Springer, 1986.

[66] L. M. Kachanov. On creep rupture time. *Izv. Acad. Nauk SSSR, Otd. Techn. Nauk*, 8:26–31, 1958.

[67] C. B. Kafadar and A. C. Eringen. Micropolar media—i the classical theory. *International Journal of Engineering Science*, 9(3):271–305, 1971.

[68] K.-I. Kanatani. Distribution of directional data and fabric tensors. *International Journal of Engineering Science*, 22(2):149–164, 1984.

[69] A. Karma and A. E. Lobkovsky. Unsteady crack motion and branching in a phase-field model of brittle fracture. *Physical review letters*, 92(24):245510, 2004.

[70] E. Katzav, M. Adda-Bedia, and R. Arias. Theory of dynamic crack branching in brittle materials. *International Journal of Fracture*, 143(3):245–271, 2007.

[71] D. Krajcinovic. Constitutive equations for damaging materials. *Journal of applied Mechanics*, 50(2):355–360, 1983.

[72] D. Krajcinovic. *Damage mechanics*, volume 41. Elsevier, 1996.

[73] C. Kuhn and R. Müller. A continuum phase field model for fracture. *Engineering Fracture Mechanics*, 77(18):3625–3634, 2010.

[74] H. W. Kuhn and A. W. Tucker. pp. 481–492 in: Nonlinear programming. In *Proc. 2nd Berkeley Symp. Math. Stat. Prob.(J. Neyman, ed.), Univ. of Calif. Press, Berkeley, CA*, volume 14, 1951.

[75] P. Ladeveze. Multiscale computational damage modelling of laminate composites. In *Multiscale modelling of damage and fracture processes in composite materials*, pages 171–212. Springer, 2005.

[76] P. Ladeveze and G. Lubineau. On a damage mesomodel for laminates: micro–meso relationships, possibilities and limits. *Composites Science and Technology*, 61(15):2149–2158, 2001.

[77] P. Ladeveze and G. Lubineau. An enhanced mesomodel for laminates based on micromechanics. *Composites Science and Technology*, 62(4):533–541, 2002.

[78] F. A. Leckie and D. R. Hayhurst. Creep rupture of structures. *Proceedings of the Royal Society of London. A. Mathematical and Physical Sciences*, 340(1622):323–347, 1974.

[79] J. Lemaitre. Evaluation of dissipation and damage in metals submitted to dynamic loading. *Mechanical behavior of materials*, pages 540–549, 1972.

[80] J. Lemaitre. How to use damage mechanics. *Nuclear Engineering and Design*, 80(2):233–245, 1984.

[81] J. Lemaitre. Micro-mechanics of crack initiation. *International journal of fracture*, 42(1):87–99, 1990.

[82] J. Lemaitre and J. L. Chaboche. A non-linear model of creep-fatigue damage cumulation and interaction(for hot metallic structures). *Mechanics of visco-elastic media and bodies*, page 1975, 1975.

[83] J. Lemaitre and J.-L. Chaboche. Aspect phénoménologique de la rupture par endommagement. *J Méc Appl*, 2(3), 1978.

[84] J. Lemaitre and R. Desmorat. *Engineering Damage Mechanics - Ductile, Creep, Fatigue and Brittle Failures.* Springer, Berlin, Heidelberg, 2006.

[85] J. Lemaitre and H. Lippmann. *A course on damage mechanics*, volume 2. Springer Berlin, 1996.

[86] J. Lemaitre, J. P. Sermage, and R. Desmorat. A two scale damage concept applied to fatigue. *International Journal of Fracture*, 97(1-4):67–81, 1999.

[87] K. R. Mangipudi and P. R. Onck. Multiscale modelling of damage and failure in two-dimensional metallic foams. *Journal of the Mechanics and Physics of Solids*, 59(7):1437–1461, 2011.

[88] C. Miehe, M. Hofacker, and F. Welschinger. A phase field model for rate-independent crack propagation: Robust algorithmic implementation based on operator splits. *Computer Methods in Applied Mechanics and Engineering*, 199(45):2765–2778, 2010.

[89] C. Miehe and A. Koch. Computational micro-to-macro transitions of discretized microstructures undergoing small strains. *Archive of Applied Mechanics*, 72(4-5):300–317, 2002.

[90] C. Miehe, J. Schotte, and J. Schröder. Computational micro-macro transitions and overall moduli in the analysis of polycrystals at large strains. *Computational Materials Science*, 16(1-4):372–382, 1999.

[91] C. Miehe, F. Welschinger, and M. Hofacker. Thermodynamically consistent phase-field models of fracture: Variational principles and multi-field fe implementations. *International journal for numerical methods in engineering*, 83(10):1273–1311, 2010.

[92] R. D. Mindlin. Micro-structure in linear elasticity. *Archive for Rational Mechanics and Analysis*, 16(1):51–78, 1964.

[93] R. D. Mindlin. Second gradient of strain and surface-tension in linear elasticity. *International Journal of Solids and Structures*, 1(4):417–438, 1965.

[94] R. D. Mindlin and N. N. Eshel. On first strain-gradient theories in linear elasticity. *International Journal of Solids and Structures*, 4(1):109–124, 1968.

[95] M. Mitchell. *An Introduction to Genetic Algorithms*. MIT Press, Cambridge, mit press pbk. edition, 1998.

[96] N. Moelans, B. Blanpain, and P. Wollants. An introduction to phase-field modeling of microstructure evolution. *Calphad: Computer Coupling of Phase Diagrams and Thermochemistry*, 32(2):268–294, 2008.

[97] S. Murakami. Mechanical modeling of material damage. *Journal of Applied Mechanics*, 55(2):280–286, 1988.

[98] S. Murakami. *Continuum Damage Mechanics - A Continuum Mechanics Approach to the Analysis of Damage and Fracture*. Springer, Berlin, Heidelberg, 2012.

[99] S. Murakami and N. Ohno. A continuum theory of creep and creep damage. In *Creep in structures*, pages 422–444. Springer, 1981.

[100] P. R. Onck, E. W. Andrews, and L. J. Gibson. Size effects in ductile cellular solids. part i: modeling. *International Journal of Mechanical Sciences*, 43(3):681–699, 2001.

[101] N. S. Ottosen and M. Ristinmaa. *The Mechanics of Constitutive Modeling*. Elsevier, Amsterdam, 1 edition, 2005.

[102] R.H.J. Peerlings, R. de Borst, W.A.M. Brekelmans, and J.H.P. de Vree. Gradient enhanced damage for quasi-brittle materials. *International Journal for Numerical Methods in Engineering*, 39(19):3391–3403, 1996.

[103] R. Poli, J. Kennedy, and T. Blackwell. Particle swarm optimization. *Swarm intelligence*, 1(1):33–57, 2007.

[104] R. S. Qin and H. K. Bhadeshia. Phase field method. *Materials science and technology*, 26(7):803–811, 2010.

[105] Y. U. Rabotnov. N., 1968. creep rupture. In *Proceedings of the XII International Congress on Applied Mechanics, Stanford-Springer*, pages 342–349, 1968.

[106] RADIOSS. *Version 11.0.* Altair Engineering Inc., Troy, Michigan, 2012.

[107] R. Schmitt, R. Müller, R. Skorupski, M. Smaga, and D. Eifler. A phase field approach for martensitic transformations in elastoplastic materials. *PAMM*, 13(1):213–214, 2013.

[108] M. W. Schraad and N. Triantafyllidis. Scale effects in media with periodic and nearly periodic microstructures, part i: Macroscopic properties. *Journal of applied mechanics*, 64(4):751–762, 1997.

[109] H. R. Schwarz. *Methode der finiten Elemente - Eine Einführung unter besonderer Berücksichtigung der Rechenpraxis.* Vieweg+Teubner Verlag, Wiesbaden, 3 edition, 1991.

[110] H. P. P. Schwefel. *Evolution and Optimum Seeking: The Sixth Generation.* John Wiley & Sons, Inc., 1993.

[111] Y. Shi and R. Eberhart. A modified particle swarm optimizer. In *Evolutionary Computation Proceedings, 1998. IEEE World Congress on Computational Intelligence., The 1998 IEEE International Conference on*, pages 69–73. IEEE, 1998.

[112] R. Siquieri, H. Emmerich, and M. Jurgk. Computation of solidification problems with hydrodynamic convection resolving energetic anisotropies at the microscale quantitatively. *European Physical Journal: Special Topics*, 149(1):27–41, 2007.

[113] H. Steeb and S. Diebels. Modeling thin films applying an extended continuum theory based on a scalar-valued order parameter.: Part i: isothermal case. *International journal of solids and structures*, 41(18):5071–5085, 2004.

[114] I. Steinbach. Phase-field models in materials science. *Modelling and Simulation in Materials Science and Engineering*, 17(7):073001, 2009.

[115] P. Steinmann. Theory and numerics of ductile micropolar elastoplastic damage. *International journal for numerical methods in engineering*, 38(4):583–606, 1995.

[116] B. Svendsen. On the thermodynamics of thermoelastic materials with additional scalar degrees of freedom. *Continuum Mechanics and Thermodynamics*, 11(4):247–262, 1999.

[117] R. Talreja. A continuum mechanics characterization of damage in composite materials. *Proceedings of the Royal Society of London. A. Mathematical and Physical Sciences*, 399(1817):195–216, 1985.

[118] C. Taylor and P. Hood. A numerical solution of the navier-stokes equations using the finite element technique. *Computers & Fluids*, 1(1):73–100, 1973.

[119] C. Tekoğlu and P. R. Onck. Size effects in the mechanical behavior of cellular materials. *Journal of Materials Science*, 40(22):5911–5917, 2005.

[120] C. Tekoğlu and P. R. Onck. Size effects in two-dimensional voronoi foams: a comparison between generalized continua and discrete models. *Journal of the Mechanics and Physics of Solids*, 56(12):3541–3564, 2008.

[121] W. Thomson. On the division of space with minimum partitional area. *Acta Mathematica*, 11(1-4):121–134, 1887.

[122] E. van der Giessen and T. Y. Wu. *Advances in Applied Mechanics*, volume 38. Academic Press, Amsterdam, Boston, 2002.

[123] W. Volk. *Untersuchung des Lokalisierungsverhaltens mikropolarer poröser Medien mit Hilfe der Cosserat-Theorie*. Inst. für Mechanik (Bauwesen), Stuttgart, 1999.

[124] G. Z. Voyiadjis and P. I. Kattan. *Damage Mechanics*. CRC Press, 1 edition, 2005.

[125] G. Z. Voyiadjis and P. I. Kattan. Damage mechanics with fabric tensors. *Mechanics of Advanced Materials and Structures*, 13(4):285–301, 2006.

[126] G. Z. Voyiadjis and N. Mozaffari. Nonlocal damage model using the phase field method: Theory and applications. *International Journal of Solids and Structures*, 50(20):3136–3151, 2013.

[127] D. Weaire and R. Phelan. A counter-example to Kelvin's conjecture on minimal surfaces. *Philosophical Magazine Letters*, 69(2):107–110, 1994.

[128] O. C. Zienkiewicz. *The Finite Element Method*. Elsevier Science & Technology Books, Oxford, 5th edition, 2000.